1949

Radiation- and Thermally Stimulated Changes in Amorphous Chalcogenide Layers and Nanocomposites

Doctoral (PhD) dissertation

Sándor Molnár

Supervisor:
Dr. Sándor Kökényesi

UNIVERSITY OF DEBRECEN
Doctoral Committee of Natural Sciences and Information Technology
Debrecen, 2020

Ezen értekezést a Debreceni Egyetem Természettudományi és Informatikai Doktori Tanács Fizikai Tudományok Doktori Iskolájának Szilárdtestfizika és anyagtudomány programja keretében készítettem a Debreceni Egyetem természettudományi doktori (PhD) fokozatának elnyerése céljából. Nyilatkozom arról, hogy a tézisekben leírt eredmények nem képezik más PhD disszertáció részét.

Debrecen, 2020. június 12.

Molnár Sándor
doktorjelölt

Tanúsítom, hogy *Molnár Sándor* doktorjelölt 2013 – 2020 között a fent megnevezett doktori iskola Szilárdtestfizika és anyagtudomány programjának keretében irányításommal végezte munkáját. Az értekezésben foglalt eredményekhez a jelölt önálló alkotó tevékenységével meghatározóan hozzájárult. Nyilatkozom továbbá arról, hogy a tézisekben leírt eredmények nem képezik más PhD disszertáció részét. Az értekezés elfogadását javasolom.

Debrecen, 2020. június 12.

Dr. Kökényesi Sándor
témavezető

Radiation- and Thermally Stimulated Changes in Amorphous Chalcogenide Layers and Nanocomposites

Értekezés a doktori (Ph.D.) fokozat megszerzése érdekében
a fizika tudományágban

Írta: Molnár Sándor
okleveles fizikus

Készült a Debreceni Egyetem Fizikai Tudományok Doktori Iskolája
Szilárdtestfizika- és anyagtudomány programja keretében

Témavezető: Dr. Kökényesi Sándor

A doktori szigorlati bizottság:

elnök:	Dr. Beke Dezső	.....
tagok:	Dr. Harsányi Gábor	.....
	Dr. Szabó István	.....

A doktori szigorlat időpontja: 2020.

Az értekezés bírálói:

	Dr.	.....
	Dr.	.....

A bírálóbizottság:

elnök:	Dr.	.....
tagok:	Dr.	.....
	Dr.	.....
	Dr.	.....
	Dr.	.....

Az értekezés védésének időpontja: 202 …… … .

Table of contents

Abbreviations and symbols

σ – electrical conductivity
η_{SE} – viscosity coefficient from Stokes-Einstein equation
C_1^- – negatively charged undercoordinated atom
C_3^+ – positively charged overcoordinated atom
C_3^0 – neutrally charged three-fold coordinated atom
AFM – atomic force microscopy
AmAc – 2-(dimethylamino) ethyl acrylate
ATR – attenuated total reflectance
c – specific heat
ChG – chalcogenide glass
D – effective coefficient of diffusion
D^- – negatively charged defect
D^+ – positively charged defect
D^0 – neutral defect
D_B – laser beam diameter
DE – diffraction efficiency
DEA – diethylamine
d_g – grating diameter
DPSS – diode pumped solid state
EDX – energy dispersive X-ray spectroscopy
E_g – optical band gap
E_η – activation energy of viscous flow during grating erasing
f_{ChG} – chalcogenide volume content in the nanocomposite
$f_{polymer}$ – polymer volume content in the nanocomposite
FIB – focused ion beam
FTIR-ATR – Fourier-transform infrared attenuated total reflection spectroscopy
FWHM – Full Width at Half Maximum
GA* – grating amplitude divided by light intensity
H – chalcogenide film thickness
h(t) –profile amplitude at a given time
h_0 – initial profile amplitude
H_g – glass substrate thickness
$h\nu$ – photon energy
H_η – activation enthalpy
I – incident light intensity
I(r) – Gaussian light intensity distribution
I_0 – light intensity in the beam center

I_{abs} – absorbed light intensity
I_B – beam current
IDA – isodecyl acrylate
ITO – indium tin oxide
IVAP – intimately bonded valance alternation pairs
J – heat flux
$J_1(x)$ – first order Bessel function
k – Boltzmann coefficient
k(T) –temperature dependent thermal conductivity
LCP – left circular polarization
LRO – long range order
m – chalcogenide mass
MEA – monoethanolamine
MRO – medium range order
n – layer refractive index
NC – nanocomposite
n_{ChG} – chalcogenide glass refractive index
n_{eff} – nanocomposite refractive index
NP – nanoparticle
$n_{polymer}$ – polymer matrix refractive index
P – laser beam power
P_{abs} – absorbed laser light power
PEA – 2-phenoxyethyl acrylate
PrA – propylamine
Q_D –effective activation energy of photo-induced diffusion
r – radius
R – surface profile radius
R_B – ion beam penetration depth
RCP – right circular polarization
RERR – relative efficiency for relief recording
r_m – moving species radius in viscous medium
r_s – radius of quasi spherical heat field distribution
s – substrate refractive index
SEM – scanning electron microscopy
SRG – surface relief grating
SRIM – stopping and range of ions in matter
SRO – short range order
S_η – activation entropy
T – temperature
t – time
TEA – triethanolamine

TEM – transmission electron microscopy
T_g – glass transition temperature
T_M – maximum transmission for the interference fringe
T_m – minimum transmission for the interference fringe
T_s – substrate transmission
T_r – room temperature
TVE – thermal vacuum evaporation
UDMA – diurethane dimethacrylate, mixture of isomers
VAP – valance alternation pairs
w – radius at which the field intensity drops to $1/e^2$
XRD – x-ray powder diffraction
α – absorption coefficient
α_{abs} – absorbed light share
ΔT – temperature rise
η_{eff} – photo-induced diffusional viscosity
θ_B – Bragg angle
κ – flattening coefficient
Λ – grating period
λ – light wavelength
ω – light wave frequency
Ω – average atomic volume
γ – surface tension of the layer
η – dynamic viscosity
κ_g – glass substrate heat conductivity
ξ – diffraction efficiency
Δn – refractive index modulation

Introduction

Research and fine-tuning diverse functional, mostly semiconductor materials is one of the current goals of modern materials science. Application of these materials require the guided and planned feasibility of changing the properties of these materials and the stability of their given properties. If an external influence can change a given material's electrical, magnetic, optical and other parameters, then there are important discoverable applications, first of all in information technologies. Of course, better understanding the structural and electron processes ongoing in the semiconductor material determinates its wider applications.

Amorphous (inorganic and organic) materials are widely used in electrical and optical memory elements, optoelectronic sensors. Further basic and applied research tasks are connected to the nanostructured materials, nanocomposites, where in addition to the size limit, quantum effects appear.

Amorphous chalcogenide materials are still in the scientific spotlight today, since they are very important for information technologies and have been in the last few decades. Achievements include applications of them in printers, detectors, optical memory storage (CD, DVD, Blu-ray) and lately in solid state storage. Research and development of these materials could replace and improve other existing, interconnected technologies and applications, like security elements and integrated optical sensors.

The semiconductor materials discussed in this work are compositions of S, Se, Te and their compounds or alloys. They maintain short and medium range order, and their physical properties can be purposefully manipulated depending on the chemical composition. The physical properties of these materials are also easily manipulated by external effects, such as light, ion or electron irradiation or the effect of temperature. All these properties inspire new insights to the physics of disordered materials and to the development of new functional materials. Potential application in biocompatible environments is also possible using some types of glasses and chalcogenides containing polymers.

This thesis is based on the research of stimulated changes in amorphous chalcogenide layers and nanocomposites to better understand the undergoing physical processes and to improve their possible applications in optics and optoelectronics. To achieve this, I have set the following goals:

1. Separate the possible role of pure light and thermally stimulated effects in optical and geometrical relief formation processes in selected amorphous chalcogenides.

2. Develop an experimental method for direct measurements of viscosity in thin solid chalcogenide layers. Separate contributions of viscous flow and photo-induced diffusion flow during surface relief grating erasing processes.

3. Develop a new experimental method for light stimulated mass transport investigations.

4. Create surface relief structures by high-energy ion beams on amorphous chalcogenides, understand underlying processes.

5. Polymer-chalcogenide nanocomposite creation for *in situ* recording holographic elements and estimation of their parameters.

My thesis consists of four main chapters: in the first chapter, I present a brief overview of irradiation sensitive materials, mostly chalcogenide glasses, in photonics. The second chapter is about sample preparation, measurement techniques and developed methods, new approaches for amorphous chalcogenide and nanocomposite investigations. The next two chapters show my individual research results contributing to this thesis. The third chapter talks about light and thermally induced effects during mass transport, and the last chapter is about the creation of chalcogenide-polymer nanocomposites and recording optical elements in such media. Following this, there is an English and a Hungarian language summary of the work.

1. Irradiation sensitive materials in photonics (literature review)

Today's science and industry have a continuous need for more advanced, more economical photosensitive materials for applications in the information technology, telecommunications, sensorics, etc. In this group we can include inorganic chalcogenide glasses, which are wide band gap semiconductors, and organic polymers, mostly used for photoresists.

Of course, the spectra of light-sensitive materials used in photonics and optoelectronics is much wider, and it includes photoconductive, luminescent, photochromic, non-linear crystalline and amorphous materials, organic and inorganic, which serve as the basis of photodiodes, photo-materials, special sensors, non-linear optical elements, luminescent materials, etc. In this work, let us restrict the definition and focus the selection of the materials to those that change structure, defectness, electron spectra and related parameters (thermodynamical, optical, electrical, geometrical) under external irradiation, serving us possibilities to memorize the signal and its spatial distribution in the form of surface or volume reliefs, measurable parameters like optical absorption, refractive index, resistivity, solubility, etc. Such well-known materials, widely applied in electronics and electronic technology are photoresists and similar X-ray-, electron- and ion beam resists. They serve as the basis of the lithography process, which mostly consists of two steps: recording hidden spatial reliefs and selective etching. The result is a spatial geometrical relief on the given surface in the layer (diffractive grating, metasurface, integrated optical element, etc.). One popular research direction in the field is the direct, one step formation of such reliefs, without the etching process, directly on the functional optical or electronic material, which may also be used for prototyping, imprint technologies at micro- and nanoscale dimensions.

From the abovementioned points of view, chalcogenide glasses are versatile, multifunctional, smart materials, at least for the discussed applications.

Various chalcogenide glasses have a wide range of optical transparency from the visible to the infrared spectrum (0,55–15 μm [1]), which makes them good candidates for applicability as optical windows or as waveguides for IR optics and sensors. These materials also have a high refractive index [1] and non-linear optical parameters [2], [3].

Furthermore, their physical properties and parameters are easily changeable by fine-tuning the composition and by external influences. One such external influence is light illumination, which can change the band gap of the semiconductor chalcogenide glass, while also influencing the refractive index, thus the material can be used as a waveguide [4], a tunable optical element in the applicable range of the light spectra [5][6].

These glasses can be used as materials for diffraction gratings [7], photonic crystals, created either directly by optical recording, holography in one-step processes or by chemical etching [8] in two-step lithography. Creating surface reliefs is also possible with ion [9] or electron beam irradiation [10]. Special compositions (phase change materials) like $Ge_2Sb_2Te_5$ are used in optical and electrical rewritable memory devices. These applications highly depend on composition and structure variations of the selected materials.

1.1 Structure and main parameters of amorphous chalcogenides

Solid matter can be divided into two groups: crystalline and non-crystalline. Crystalline materials having an ordered and non-crystalline having a disordered structure.

In an ideal crystal, the whole crystal could be reproduced by translation along the coordinate axes, if the position of an elementary unit cell is known. This is called long-range order (LRO).

In a wide range of silicon-, oxide-, halogenide- and chalcogenide-based amorphous inorganic materials, which display semiconductor properties connected with excitation and presence of n- and p-type charge carriers, specific defects, the S and Se based materials are the most interesting. This is due to their multifunctionality, especially in relations to information technologies and comparatively easy materials technology.

Chalcogenide amorphous solids and glasses are known for their disordered structure, with a given short-range order (SRO), not having long range order, but some of them have peculiar “layered” or “chain-like” elements that make them closer to polymers (Fig. 1.1. and Fig. 1.2.). Within the first coordination sphere (number of neighboring atoms) around each atom, there is a resemblance between LRO and SRO. The number of neighboring atoms and their position in space are preserved, since the binding forces are the same. Step-by-step, the forces are weaker and when reaching the third-forth coordination sphere, the constraints of the directional covalent bonding are lost.

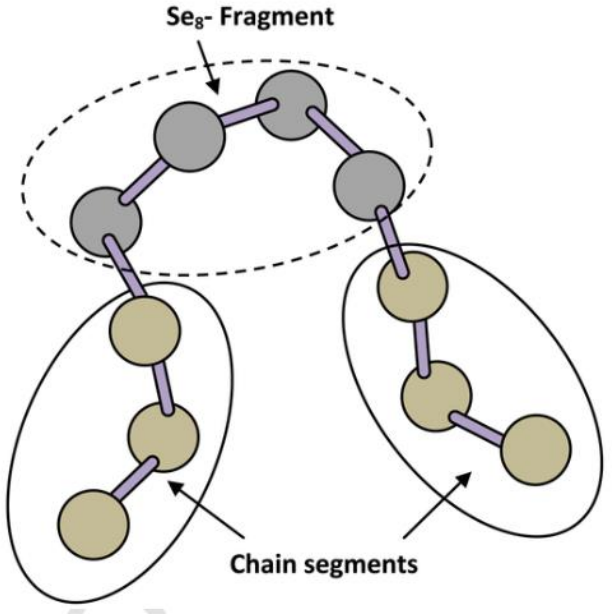

***Fig. 1.1**. Local molecular order in a selenium chain in which there are "chain-like" and "ring-like" segments (after [11]).*

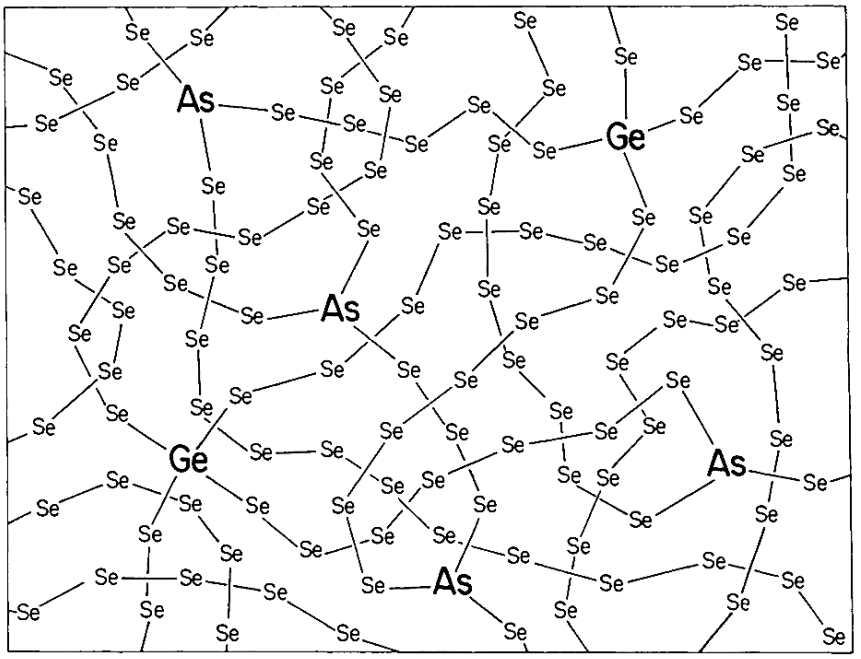

***Fig. 1.2.** Schematic bonding topology of $Se_{1-x-y}As_xGe_y$ glass ([12]).*

The ordered, crystalline state is thermodynamically the most favorable for atoms. When the covalent bonds are all satisfied, the free energy of the resulting crystal essentially decreases. Deviations of the atoms from this ordered state means, that there is additional free energy in the system, meaning glassy or amorphous solids have higher free energy compared to crystals. Medium-range order (MRO) was later introduced by materials physicists, because of the diversity of this state and unique elements in the diffraction pattern of chalcogenide glasses, polymeric materials, etc [1].

The most important parameters which determine the properties and applicability of chalcogenide glasses and amorphous layers are the softening temperature T_g, and the related viscosity, optical band gap E_g, electrical conductivity, σ. These parameters strongly depend on composition, even in one system, like the most known and investigated in my work, the As-Se system. Sometimes they are affected by material preparation conditions like evaporation and substrate temperature, material purity, like in the case of amorphous thin films.

	Se	$As_{10}Se_{90}$	$As_{20}Se_{80}$	As_2Se_3	As_2S_3	$Ge_{16}Se_{84}$	$Ge_{20}As_{20}Se_{60}$
T_g, ºC	40 [13]	82 [13]	104 [13]	193 [13]	206 [14]	143 [13]	280 [14]
E_g, eV	2.1 [15]	1.5 [14]	1.7 [14]	1.76 [15]	2.4 [15]	2 [15]	1.8 [14]
$-\log\sigma_{20ºC}$	13.8 [15]	14.9 [14]	13.5 [14]	12.2 [14]	18.1 [14]	15.8 [15]	16.1 [14]

Table 1.1. *Some parameters of typical chalcogenide glasses.*

These parameters strongly influence the sensitivity of the glass or layer to the given irradiation, heating, deformation. The photo- or more generally the irradiation-sensitivity is strongly related to the defectness of the structure, presence of certain spectra of electron-hole trapping centers in the forbidden band gap of these semiconductor materials.

1.2 Specificity of defects in non-crystalline chalcogenides

Deviations from the ideal long-range lattice order are known as defects in crystalline solids. The deviation of the structure from its low equilibrium state could be described as increasing or decreasing the density

of defects. Defects are related to specific electron energy states, which heavily influence the materials' optical and electrical properties.

Structural relaxation of the defects causes energy release to the system and mechanical deformation results an increase in the number of defects and energy absorption [16] [17].

Defects properties of amorphous and glassy solids are qualitatively the same as in crystalline solids [18]. The most important ones are discussed below.

The *vacancy-like defect* could be described as a local group of atoms, with a lower local density compared to the average density of the material.

The dangling bond is an unsatisfied valance electron on an immobilized atom. Such bonds help reducing stresses accumulated during network development.

Wrong bonds are the most common chemical defects in amorphous semiconductors. In a binary covalently bonded alloy, energetically the most favored, is that heteropolar bonds are created instead of homopolar bonds (e.g. As-S bonds instead of As-As bonds in the case of As_2S_3). Wrong bonds occur when the same type of atoms are bonded instead of a heteroatomic bond. Occurrence of these bonds are noticeable during thin film deposition by evaporation.

Chemical impurities are foreign atoms in the amorphous network. Considering the large number of states in the band gap, amorphous semiconductors are usually not easy to dope [1]. Contrary to this, amorphous selenium is very sensitive to doping [19]. Its dark conductivity can be increased significantly with a few hundred ppm dopants of oxygen, potassium or chlorine [20]. It was reported that, the addition of Cl into a-Se could change its conductivity to n-type.

It was assumed [21], that amorphous solids have tails of localized states in both valance and conduction bands, and the localized states from the extended states are separated by a mobility edge. The band tail extends into the band gap, and as the result of their superposition, the Fermi level is pinned. According to Davis and Mott [22] the mechanism of Fermi level pinning in chalcogenides is unlikely, and they are the result of deep levels caused by defects. Anderson [23] suggested, that in chalcogenides the electron spins are paired as a result of strong electron-lattice interaction. Furthermore, the repulsion inside the electron pair is compensated by energy obtained by the result of chemical bond distortion. These are the so-called negative-U centers and the electron repulsion is characterized by them.

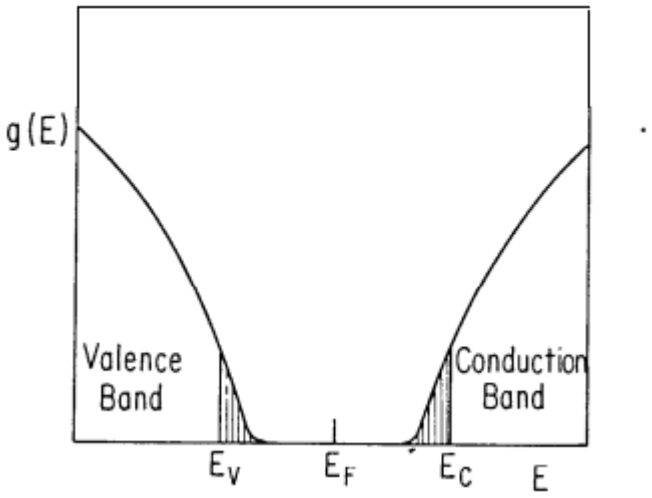

***Fig. 1.3**. Sketch of density of states g(E) for an ideal amorphous semiconductor. E_V and E_C are the mobility edges separating the tails of localized states from the extended band states (after [24]).*

For the dangling bond centers Mott [25] used the following notations: D^0 (neutral center), D^+ (positively charged center), D^- (negatively charged center). According to Mott, the $2D^0 \rightarrow D^+ + D^-$ reaction is exothermic, with all electron spins becoming paired, which can explain the lack of an electron spin resonance signal.

Kastner et al. [26] suggested that thermodynamically it is advantageous for the system, if the defects are created in pairs: a positively charged over- and a negatively charged under-coordinated atom, which are called *valance alternation pairs* (VAPs). The following notations were introduced:

C_1^-, C_3^+, C_3^0, where the subscript is the number of neighboring atoms, and the superscript is the charge state of the defect atom. The $D^+ D^-$, or $C_3^+ C_1^-$ defect pair is regarded as essential in amorphous chalcogenides.

In a-Se, VAPs can be created by bond breakage between atoms when an electron is moved between one of the triply bonded selenium atoms to an atom where the crosslink was broken. The electron transfer reduces the total energy of the solid, and almost all trigonally bonded selenium atoms become VAPs. The energy for such VAP creation is small, since the number of bonds remains constant during the defect creation.

Intimately bonded valance alternation pairs (IVAP) are created as the result of two near VAPs bonding with each other [27].

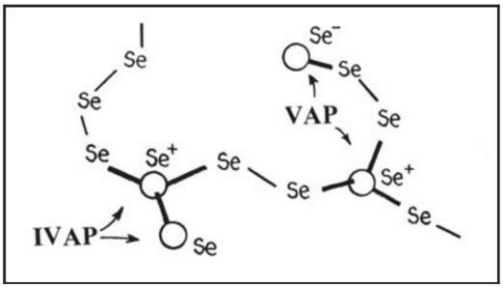

***Fig. 1.4**. Representation of the IVAP and VAP defects (after [1]).*

Defects in chalcogenides can also be induced, or their number can be changed by photo illumination, and can be further enhanced by oblique deposition or other variations of technology [28], [29],[30]. Finally, after years of multiple studies it is commonly accepted that there are well defined states in the forbidden gap in chalcogenides [24], [25], [26], [27] and their involvement in the formation of optical parameters (Urbach tails, optical band gap, luminescence) in chalcogenide glasses is necessary to explain photo-induced, optical recording effects as well.

1.3 Induced changes in amorphous chalcogenides

External influences in chalcogenide glasses and amorphous layers can change the materials' optical, electrical, structural, compositional, physico-chemical properties. These influences include light illumination, high energy illumination (X-ray, gamma ray), electron and ion beam irradiation and thermal effects.

1.3.1 Photo-induced changes in amorphous chalcogenides

Influence of radiation (from ultraviolet to near infrared light, neutrons, gamma- or X-ray) on the material most of the time occurs with absorption of energy, electron and/or hole excitation, atomic movements, phonon generation or amplification. Irradiation can induce changes in the structure of the material, electrical conductivity and temperature. Melting or evaporation of the material may occur as well [1]. Radiation can also create defects, bond redistribution, crystallization or amorphization. As well as chemical reactivity change, changes of surface profile, optical transmissivity, reflectivity, change of refraction index, hardness, thickness, fluidity may happen [31]. Usually one photon is absorbed during light illumination, but two or more photon absorption is possible with high intensity laser pulses.

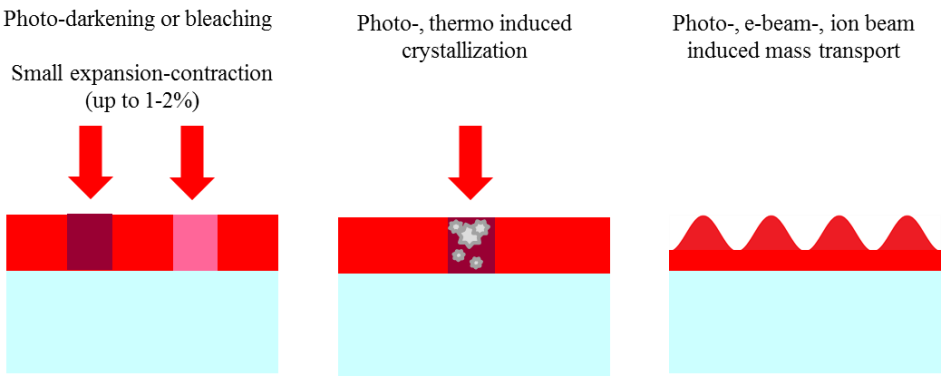

Fig. 1.5. *General effects on chalcogenides under irradiation.*

In amorphous chalcogenides, the disorder of the atoms is high and the density is lower compared to the same material's crystalline form (if available), hence larger free volume is available in them, which is preferred for compositional and coordination defect development. This disorder is even larger in amorphous layers compared to glasses [32].

The larger photo-induced changes compared to other materials could be explained by the following:

1) In chalcogenide glasses, the chalcogens mostly have two-fold coordination and 90–109° angle between these covalent bonds. Structures like these are flexible and the bond angle can easily be distorted. Vibrations of such connected chalcogen atoms can be described as free oscillators, since these atoms are localized and independent [33].

2) Homoatomic bonds can be formed between chalcogen (Se, S), pnictogen (As, Sb, Bi) and group IV (Si, Ge) elements (i.e. As-As, Se-Se, Ge-Ge). These bond energies are not far from the bond energies between chalcogenide–metal or chalcogenide–metalloid bonds (Table 1.2., after [1]), which permits coordination changes of individual atoms [34][35].

Bond	E, eV	Bond	E, eV	Bond	E, eV
S–S	2.9	P–Se	2.49	Sb–Te	2.02
Se–Se	2.33	As–As	2.07	Si–Si	2.33
Se–Te	2.02	As–S	2.7	Si–Te	2.28
S–Se	2.64	As–Se	2.38	Ge–Ge	1.92
Se–Te	2.28	As–Te	2.12	Ge–S	2.74
P–P	2.33	Sb–Sb	1.81	Ge–Se	2.38
P–S	2.8	Sb–S	2.38	Ge–Te	2.07

Table 1.2. *Bond energies for atom pairs (after [1]).*

3) Exposure could induce charged over- and under-coordinated atomic defects in amorphous chalcogenides, which increase (or decrease) the densities of the localized states in the band-tails and cause absorption edge shift [1] (darkening or bleaching).

4) Non-bonding electrons (lone pairs) are common in chalcogens and pnictides, which are the top part of the valance band in these materials [15], [31]. The lone pairs can be transferred to the bonding orbitals or the other way around. Lone pairs can form new bonds, which can alter the geometry of local structural units [1].

5) The high free volume makes the chalcogenide glasses flexible [35]. This enabled that the highest photo-induced changes were found for large free volume systems [32], and the composition with the maximum free volume is near the average coordination number of 2.7 [36].

6) Chalcogenide glasses are metastable, exposure can induce structural transformations in them (e.g. crystallization). Surprisingly, amorphous films can be created as unique compositions that are outside of the regular glass-forming region of the bulk glass.

These photo-induced changes can be put into two groups: reversible and irreversible changes.

1.3.2 Reversibility of photo-induced changes

Reversible changes are mostly seen in bulk chalcogenide glasses and annealed (heat treated) amorphous layers. These processes include crystallization-amorphization, changes in optical transmittance and reflectance, refraction index, volume, reactivity, etc.

Thermal annealing near the softening temperature of the glass can revert the structure to its original state, as well as certain light exposure [1]. One of the simplest systems, where reversible photo-induced changes can be observed is amorphous selenium. In selenium, the Se_8 rings can transform into polymer-like Se_n-chains under illumination, which could be behind reversible photodarkening. Another possibility is that bond switching happens via lone-pair electron photoexcitation, forming dynamic interchain bonds [1].

Macroscopically, the result of excitation can be photo-contraction, photo-expansion, change in viscosity and hardness. It has been shown in several amorphous chalcogenides, that light with wavelength corresponding to the Urbach tail of absorption edge of that material can cause photo-induced volume expansion [31].

Hisakuni and Tanaka [37] observed a phenomenon called giant photo-expansion, which really is a mass-transport connected phenomenon, where As_2S_3 have been illuminated with laser light, and the material's thickness increased 10 times more compared to regular photo-expansion [38]. Such surface structures could be erased by local heating of the amorphous material above its T_g or with appropriate light illumination.

Optically induced viscosity change was reported in a-Se and described as photomelting, and purely optical in nature [39]. In As_2S_3 [40] it is supposed that light breaks van der Waals bonds and excites the valance band tail electrons into antibonding orbitals and lower the chemical bond order [1]. After breaking these bonds, the glass can flow more freely. Even light, with energy lower than the band gap of the chalcogenide semiconductor can cause significant viscosity decrease in As_2S_3 [40]. The effect can be explained by excitation of van der Waals or weaker bonds in the chalcogenide glass. The initial state of viscosity is returned, when the illumination is eliminated [1].

1.3.3 Irreversible structural changes

Irreversible photo-induced changes are more prominent in as-deposited chalcogenide films. At evaporation with high vapor temperature the chalcogenides can dissociate into lower molecular mass fragments, and the film can become inhomogeneous (the composition could differ per

volume). Irreversible changes could be introduced to this metastable structure by light illumination, such as photodarkening (absorption edge shifting to longer wavelength) and photobleaching (absorption edge shifting to shorter wavelength). Irreversible photodarkening could occur, due to the creation of defects and localized electronic states in the conduction and valence bands tails, which in turn decrease the band gap [31]. In as-deposited films there is also higher refraction index change upon illumination [15]. Amorphous chalcogenide layer refractive index change can be expressed by the Wemple-DiDomenico formula, using a single oscillator approach [41], [42]:

$$(n^2 - 1)^{-1} = \frac{E_0^2 - (h\nu)^2}{E_0 E_d}, \quad (1.1)$$

where, E_0 is the single oscillator energy, E_d is the dispersion energy, which is connected to the material's type and structure.

Changes of chemical reactivity can also occur. The dissolving rate of exposed chalcogenides can be influenced by specific chemical reactants. For example, freshly evaporated As_2S_3 contains large amounts of As_4S_4 [43], which is relatively resistant to alkalines. Exposed regions of freshly evaporated As_2S_3 contain less As_4S_4 than the unexposed region, hence the dissolution of the exposed region is faster in alkalines. Depending on the previous chemical treatment of the surface, both positive and negative etching can be achieved on As-S compositions [44].

There is also non-reversible crystallization, where photons with near band gap energies are energy sources for crystalline nuclei. It was detected in various chalcogenides, where materials form unstable glasses, such as a-Se [1]. However, reversible crystallization is also possible by exposure. Exposure-induced amorphization was first discovered in crystalline $As_{50}S_{50}$ films under the glass transition temperature [45]. RW DVD, based on some chalcogenide compositions, uses the effects of reversible crystallization-amorphization process by selecting appropriate heating-cooling parameters.

1.4 High energy ion irradiation and electron beam induced changes

When irradiating absorbable energy onto chalcogenide glasses by high-energy quanta or particles, similar changes can be achieved as with

light from visible spectral region, such as darkening, relief formation via bond breaking and defect generation. The difference is that high-energy irradiation excites much more atoms, compared to band gap light, and can create multiple orders of magnitude, more electron hole pairs and defects. These include irradiation by γ-, X-ray, electron- and ion beam.

The best-known changes were achieved by γ-irradiation on As_2S_3, As_2Se_3 and other chalcogenides, which showed the band gap moving to the longer wavelength of the spectrum (photodarkening). Additionally, the samples experienced change in their mechanical, optical and electrical properties [46], [47].

Nishihara et. al. showed [48], that direct writing of optical gratings on As_2S_3 layers by electron beam is possible, where in the irradiated regions the refractive index increases proportionally to the irradiation dose and voltage. Later it was found [49] that electron beam irradiation caused film thickness shrinkage and the refractive index change is composition dependent. Surface relief structures created by line scanned electron beam are also possible, where local height increase under irradiation was reported. Here, the underlying process is thought to be surface deformation as the result of electrostatic force action and electro-induced fluidity [50].

What is most known about ion irradiation induced changes, is that the absorption edge of $Ge_{20}Se_{80}$, GeSe, As_2S_3, AsSe, As_3Se_2 glasses is moving towards higher wavelength when irradiated with 1 MeV-es Kr^{2+}, 60 MeV C^{5+} and few hundred keV energy Ar^+, N^+ and O^+ ions [51], [52], [53].

Lately the effects of up to 180 keV H^+ and D^+ ions on chalcogenides were investigated at the Institute of Physics, University of Debrecen [54]. The chalcogenide samples experienced darkening and refractive index increase after irradiation [54]. A Se/As_2S_3 type multilayer structure experienced 6% layer thickness change [55]. Large, 40% volume contraction occurred in obliquely deposited $Ge_{25}Se_{75}$ samples, when irradiated with 50 keV He^+ ions [56]. However, there are very few or no research data on high-energy ion irradiation with low mass ions on chalcogenides and their possible applicability.

1.5 Photo-induced mass transport effects

Photo-induced volume expansion has been observed in various amorphous chalcogenides, when the stimulating light energy corresponds to the Urbach tail of the absorption edge of the material [31].

Surface relief creation is also possible with at least two coherent laser beams, to create surface relief gratings (SRGs). The first recorded SRG was

created on an As_2Se_3 layer by Chomat in the 1970s [57]. These holograms could be erased by heating or illumination. Such investigations on the topics of surface reliefs appeared many years later on optical polymer films [58]. Azopolymers have very similar recording characteristics to amorphous chalcogenides and new experiments on chalcogenides followed after them. Chalcogenides obtained more attention due to the higher stability and compatibility with microelectronic technology.

It was reported that beam polarization properties highly influence the generated surface relief structures. Polarization of the recording beam has an essential role in anisotropic photo-induced mass transport. The gradient of the intensity field and the material's polarizational properties were supposed to determine the direction of anisotropic photo-stimulated diffusion [59].

In As_2S_3 thin films, higher efficiency of relief recording by *p:p* polarized beams was achieved compared to *s:s* polarized beams, when two coherent laser beams were used. Additional *s*-polarized non coherent beam to the *p:p* setup (*p:p-S*) resulted the highest recording efficiency for surface relief grating in the "simple" polarized laser setup. Furthermore, overall highest efficiency was achieved by right circular polarization - left circular polarization (*RCP:LCP*) and orthogonal linear (-45 degree +45 degree) setup [60]. Similar recording efficiencies depending on polarization setup were reported for other chalcogenide compositions as well.

Mass transport efficiency also depends on the holographic grating's period [61] and material composition. In the As-Se system the highest efficiency was reported for $As_{20}Se_{80}$ [62].

Irradiation intensity dependence of mass transport direction was also reported, where on an As_2S_3 layer low intensity focused laser beam with band gap comparable energies created a surface bump, independent of beam polarization. However, higher intensity beams created a valley with pileup of the material around where the valley was formed. The pileup direction depended on the light polarization [63].

Real-time Atomic Force Microscopy (AFM) showed that in the As-Se system mass transport direction is dependent on the laser polarization and the material's properties. The mass transport occurs from the illuminated regions to the dark regions in the case of a-Se, and from dark regions to illuminated regions in the case for $As_{20}Se_{80}$, when *p:p* polarization setup was used. In both cases, photo-induced mass transport starts with small volume expansion in the illuminated region, but for a-Se it changes direction after a short time [64], [65]. The directional dependence of photo-induced mass transport may be connected to the

different electron-hole mobility and lifetime parameters in these materials, which is not fully understood yet.

Surface relief grating formation is also possible at liquid nitrogen and helium temperatures [66], [67]. The central mechanism of the mass transport is thought to be diffusion flow. One possible driving force of photo-induced mass transport is the lateral steady state electric field induced by light interference. The surface relief grating formation is dependent on the temperature due to the diffusion coefficients' temperature dependence [66]. Creation of such structures is illumination-dependent: increasing illumination intensity increases mass transport efficiency, upon reaching T_g of the material.

Light intensity and polarization also effects erasing of the surface relief structures. Surface relief grating erasure rate was much faster with *p*-polarized light, compared to *s*-polarized light. Higher grating period also resulted in prolonged erasure time, where erasure was the fastest on the 1.5 μm grating and slowest on 7.5μm grating [68].

Lateral mass transport during surface relief patterning is related to inhomogeneous light intensity pattern that causes inhomogeneous distribution of chemical potentials, as suggested in [68]. Near band gap light creates non-equilibrium carriers in the chalcogenide glass, where non-radiative relaxation can create broken bonds and giant photoexpansion while decreasing the viscosity. In the chalcogenide glass, absorbed light creates electron-hole pairs. The recombination can occur via transient valance alternation pairs. After recombination, bond deformation can occur and atoms can move over atomic distances, where the recombination energy can be released [69].

Data is still unclear on the process of mass transport, whether electric properties, heat effects, light polarization (or the lack of) influences its direction and effectivity, and hence it needs further examination.

2. Amorphous Chalcogenide and Nanocomposite Samples: Preparation, Measurement Techniques and Methods

2.1 Sample deposition and preparation

2.1.1 Chalcogenide samples

I used bulk 5N purity glasses from the As (Ge)-S (Se)-Te system for preparation of amorphous chalcogenide layers by thermal vacuum evaporation (TVE), because of their comparatively low softening temperature. Furthermore, this is one of the most economical, simple and practical deposition techniques for such materials from metal evaporators of different configurations. The bulk glasses were made at Uzhhorod National University in the framework of a cooperation agreement and common researches.

I made the thin layers of chalcogenide glasses by thermal vacuum evaporation from a molybdenum or tantalum boat at 10^{-5} Torr pressure and 10-20 nm/s deposition rate with the TVE system at the Experimental Physics Department, University of Debrecen. Layer thicknesses were between 0.5-35 μm depending on the required application. At the evaporation procedure, the evaporation boat was heated up by constant current. I regulated the layer thickness empirically by choosing the weight of the material, evaporation time and by changing the distance between the evaporation boat and the sample.

Three or more component materials with high softening temperatures can also be evaporated by this method, but to achieve the same composition in the evaporated layer as in the bulk, sputter free (i.e. quasi closed) evaporation boats may be required. I usually used special microscope silicate glasses as substrates, though indium tin oxide (ITO) coated glass substrates or polished silicon wafers were used as well, if higher thermal or electrical conductivity was required. Layer thicknesses of the deposited films were homogenous up to 3-4 μm. These were used mainly for photodarkening-bleaching and surface relief grating recording-erasing measurements.

For ion beam measurements, I deposited 25-35 μm thick layers with the TVE method. Such a large thickness introduces difficulties in optical parameter measurements and calculations, because of larger layer thickness inhomogeneities. I achieved the larger layer thickness by decreasing the evaporation boat–sample distance and/or increasing the deposition time. In addition to the layers, few types of the chosen samples were bulk glassy

selenium with smooth cleaved surface and bulk As_6Se_{94}, As_2S_3, $As_{30}Ge_{20}S_{50}$ glass samples. I formed these bulk samples into thick plates with 1-3 mm in thickness, by raising the temperature of the glass above its T_g and pressed them between polished molds. For studying temperature and crystallization effects I fabricated and used bulk a-Se polished plates (S1), 2–3 mm in thickness, and used twenty-year-old (kept at room temperature in dark) a-Se plates with unpolished highly reflective smooth surfaces (S2). The twenty-year-old selenium sample was taken from an ampule with quenched chalcogenide glass to study the possible ageing or crystallization effects. The latter sample was heat treated and rapidly cooled down, to create parallel plane samples for the measurements. These bulk a-Se samples were chosen for surface profile creation by focused He-Ne laser beam (633 nm). The beam had a 10 μm diameter and the laser power intensity ranged between 2–27 mW, and was controlled by neutral filters.

I measured the layer thicknesses and surface reliefs with Ambios XP-1 profile meter. EDX by Hitachi S-4300 CFE type SEM was used for checking the chemical composition of the evaporated chalcogenide layers. Chemical bonds were studied by micro-Raman measurements with Renishaw 1000 micro-Raman spectrometer, where 785 nm excitation wavelength was used.

2.1.2 Polymer-chalcogenide nanocomposite sample preparation

The polymer-chalcogenide nanocomposites (NCs) were made by adding As_2S_3 and $As_{20}Se_{80}$ chalcogenide nanoparticles into a polymer matrix. Two methods were used to create the chalcogenide nanoparticles.

The first tested method to create chalcogenide nanoparticles involved a femtosecond Nd:YAG laser (532 nm wavelength, 8 mJ power in a pulse, power density of 4 J/cm^2, 10 Hz repetition rate). In this experimental setup, I submerged the chalcogenide layer into a liquid monomer matrix. Here, my goal was to ablate nanoparticles from an As_2S_3 chalcogenide layer directly into the monomer matrix by the femtosecond laser. This method only yielded a low 1 wt% nanoparticle concentration in a thin layer at the target surface. The low yield may be the result of the relatively high viscosity of the monomer matrix, which caused agglomeration of the ablated chalcogenide nanoparticles. To obtain higher yield, a chemical method was proposed based on the dissolution of ChGs (Chalcogenide glass) in amines.

The amines used were diethylamine (DEA), propylamine (PrA), monoethanolamine (MEA) and triethanolamine (TEA). The best outcome

was achieved with DEA. The dissolved chalcogenides in DEA were added to a combination of monomers as the next step.

For the monomer matrix, these materials were used: diurethane dimethacrylate, mixture of isomers (UDMA, ≥ 97%), isodecyl acrylate (IDA), 2-phenoxyethyl acrylate (PEA), 2-(dimethylamino) ethyl acrylate (AmAc). As the initiator for polymerization, Irq784 was used, since it is sensitive up to 550 nm light, and green laser light could be utilized for photo-polymerization. These monomers were chosen because of the presence of certain functional groups, which may stabilize the ChG nanoparticles.

The creation of the chalcogenide nanocomposite happened in the following order. The first step of creating the nanocomposites was to dissolve the chalcogenide glass (7.5 wt% of monomer mixture) in DEA, to reduce the ChG particle size to the nanometer range. In the next step, to this solution, a monomer mixture (see Table 2.1**.**) was added and stirred for 24 hours with Irg784 initiator in chloromethylene (4 wt% of monomer mixture). The nanocomposite in this state was kept in nitrogen atmosphere in darkness, until the DEA solvent is evaporated. This was controlled by measuring the weight of the nanocomposite and DEA before and after the evaporation.

This process resulted in stable, transparent, slightly yellowish nanocomposites, with the compositions presented in Table 2.1.

№	Monomer ratios [wt %]			Initiator Irq784 [wt %]	ChG [wt %]
11h	UDMA 80	IDA 10	PEA 10	4%	7.5 % As_2S_3
14h	UDMA 70	AmAc 20	PEA 10		7.5 % As_2S_3
20h	UDMA 70	AmAc 20	PEA 10		7.5 % $As_{20}Se_{80}$

Table 2.1. *The developed nanocomposites [70].*

I made the solid chalcogenide nanocomposite films for optical measurements by placing some amount of this solution between glass substrates or between a glass substrate and a polyester cover, with a 30 μm spacer between them (layer thickness 30 μm), and polymerized it by UV light (10 mW/cm^2) for half an hour.

A Bruker Tensor-37 ATR-Miracle-Pike equipment was used for ATR measurements, Hitachi S-4300 SEM, JEM-2000FXII TEM and XRD equipment were used for structural investigations of the NC.

More detailed information about the used chalcogenide and polymer samples are available at the end of the work in the Appendix.

2.2 Experimental setups and developed methods for surface relief investigations

Developing methods for surface relief investigations was one of the main objectives of this thesis: to find mass transport direction and efficiency on selected chalcogenide compositions, get data on thin film viscosity, and separate light and heat effects during recording-erasing processes.

For this reason, I used two main experimental approaches in surface relief formation experiments: holography, i.e. recording the optical interference picture, and optical recording through a mesh metal mask, which relates to the recording diffraction patterns.

2.2.1 Setup for holographic grating recording on simple and adjacent layers

For simple holographic recording the following setup was used, presented in Fig. 2.1. I set up the holographic system by adjusting the laser polarizations, powers and incident angles with the goal to get high quality interference pattern. In this setup Laser *1* was used as the recording laser, where the beam splitter divided the beam into two, and the mirrors guided the beams to create an interference pattern on the sample surface. Laser *2* was used to accelerate the recording process.

Usually, I used 2–3 μm thick chalcogenide layers for holographic grating recordings. The grating periods were between 3.5 and 15 μm. In the experiments, I used standard *s:s* or *p:p* polarized laser beam configurations and sometimes additional *p*- or *s*-polarized beams to accelerate the recording process [60]. For As-Se based compositions 633 nm wavelength He-Ne or 650 nm diode lasers, for As-S or Ge-Se based compositions 532 nm wavelength DPSS lasers were used for creating the interference pattern on the layers' surface and to accelerate the recording.

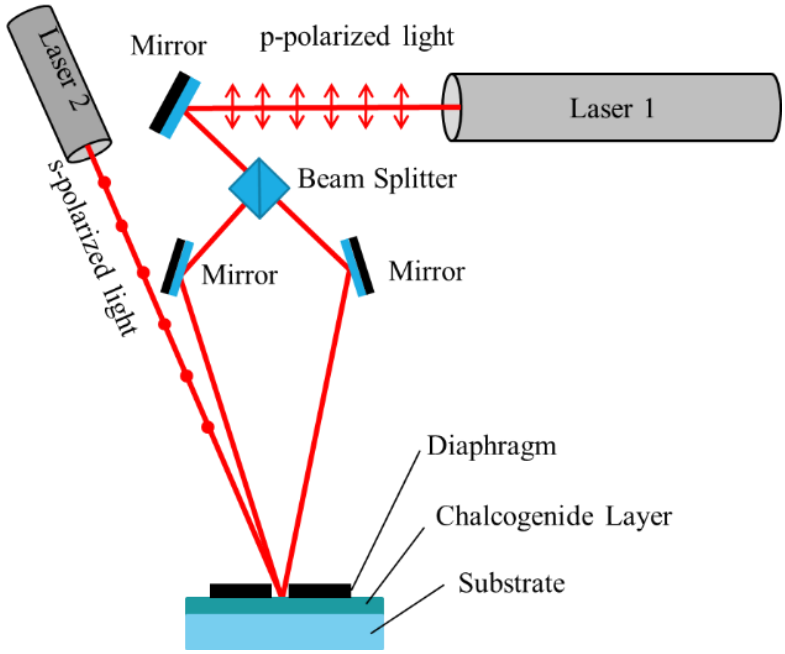

Fig. 2.1. *Experimental setup for holographic relief recording [71].*

The adjacent layers method (Fig. 2.2.) was used to determine the direction and efficiency of the photo-induced mass transport in selected chalcogenide glass compositions. In this method, I used a glass substrate, where chalcogenide layers (1–6 μm thickness) were deposited next to each other on the substrate with a very small, usually under 20 μm gap between the edges of the adjacent layers. Producing such combined layers with a minimal gap between proved to be challenging, but it was required for successful AFM measurements. One of the chosen thin films for such investigations was usually a-Se, while the other was chosen from the As_xSe_{100-x} system (x=1, 3, 6, 20, 40). For mass transport comparisons, the adjacent layers need to be sensitive in the same spectral range. Therefore, for the As-Se system a 633 nm laser and for the As-S system a 532 nm laser was used.

The layer deposition (TVE method) was made by covering half of the glass substrate with a metal mask, and on the uncovered side I deposited an As_xSe_{100-x} layer. Amorphous selenium was deposited as the next step, with the As_xSe_{100-x} layer masked and selenium deposited on the free surface. The subsequent evaporation resulted in tightly deposited layers with minimal gap between them. Overlapping layers would have caused mixture of the As-Se and Se layers, and a too wide gap would have caused inability

to get a good result with AFM. I achieved the small gap by carefully positioning the metal mask.

The recorded hologram was formed by two interfering *p*-polarized laser beams of a He-Ne laser (633 nm wavelength) with 1.8 mm diameter and Gaussian intensity distribution on the adjacent layer junction of the surface. (Fig. 2.2.). For accelerating the grating formation process, I used an additional non-coherent *s*-polarized He-Ne beam.

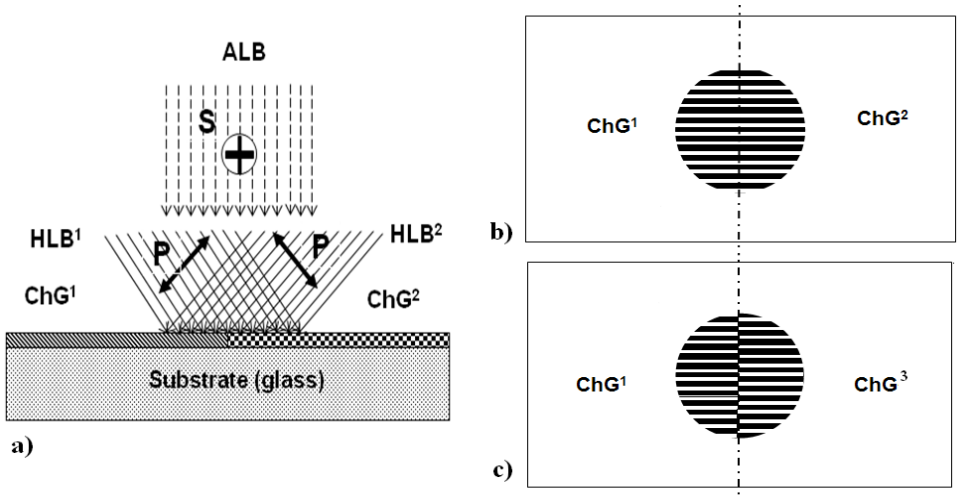

Fig. 2.2. *Adjacent chalcogenide layers method for surface relief investigations: a) $ChG^1(^2)$ – chalcogenide layer 1 (2), $HLB^1(^2)$ – holographic laser beam 1 (2), ALB- assisting (amplifier) laser beam, p:p and s – laser polarizations; b) $ChG^1(^2)$ – chalcogenide glasses with the "same phase" recording nature; c) $ChG^1(^3)$ – chalcogenide glasses with different "opposite phase" recording nature [72].*

The recording laser beam's Gaussian radial light intensity *I(r)* distribution during surface relief hologram recording can be expressed as:

$$I(r) = I_0 \, exp\left(-\frac{2r^2}{w^2}\right) = \frac{2P}{\pi w^2} exp\left(-\frac{2r^2}{w^2}\right), \qquad (2.1)$$

where: r – distance from the laser beam center, I_0 – light intensity in the beam center, P– laser beam power, w – radius at which the field intensity drops to $1/e^2$, respectively. $I_{0He\text{-}Ne} \approx 5000$ W/m^2, $w_{He\text{-}Ne} \approx 0.9$ mm for the given *p*-polarized He-Ne laser beam and $I_{0\ He\text{-}Ne\_amplifier} \approx 7300$ W/m^2, $w_{He\text{-}Ne\_amplifier} \approx 0.75$ mm for the *s*-polarized He-Ne laser respectively. Full laser beam power in the recording spot was equal to 19.5 mW [72].

2.2.2 Mesh mask method setup for surface relief investigations

The second method I used for creating surface reliefs was illumination through a mesh mask with 60 μm period (Fig. 2.3.), similar to the slit method used by Teteris [60]. However, this method gave the possibility to separate mass-transport processes in two dimensions *in situ*.

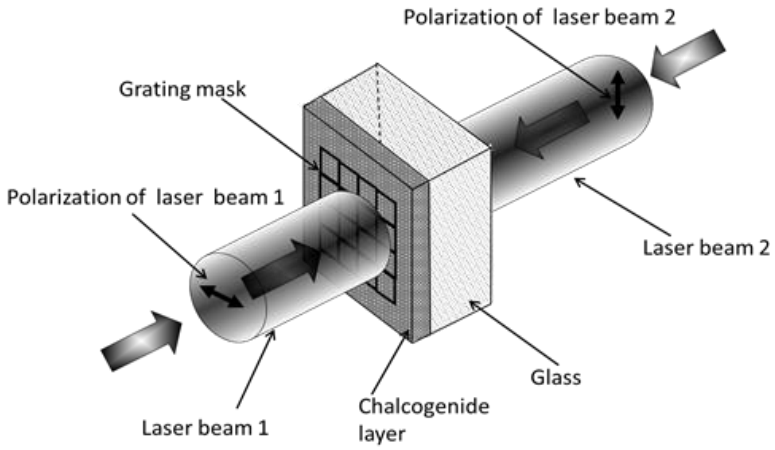

Fig. 2.3. *Square grating (mesh mask) optical recording setup (front side recording laser with horizontal polarization, back side assisting laser with vertical polarization) [72].*

With this method (see Fig. 2.3.), we can find the direction of the photo-induced mass transport at given illumination conditions. Laser beam *1* with a certain light polarization illuminates the mesh mask, and the diffracted light on the mask edges creates a periodical light intensity pattern. The backside laser (Laser beam *2*) with a perpendicular polarization to Laser beam *1* may be used for accelerating the relief formation process.

Experimental parameters of the lasers used for the Se and $As_{20}Se_{80}$ layer recordings are described below.

He-Ne laser, with maximum light intensity (at the beam center): 19 mW, illumination density $I_{0He\text{-}Ne\_recording} \approx 16000$ W/m^2, $w_{He\text{-}Ne\_recording} \approx 0.9$ mm beam waist (front side recording laser) and 6.5 mW, $I_{0He\text{-}Ne\_assisting} \approx 7300$ W/m^2, $w_{He\text{-}Ne\_assisting} \approx 0.8$ mm (back side assisting laser), respectively.

For As_2S_3 and other sulphur-based layers, I used DPSS lasers with 532 nm wavelength, because of their wider band gaps. The front side DPSS laser had 40 mW power and 40000 W/m^2 maximum light intensity density.

The back side laser had 14 mW power, 14000 W/m^2 maximum light intensity density. The *w* was 0.8 mm for both 532 nm laser beams.

The investigated layers' thicknesses ranged between 2–3.6 μm. Grating recording time ranged from 2 to 3 hours.

For vibration-free recordings, I recorded all reliefs for mass transport and efficiency comparisons on a Newport Optical breadboard table.

2.3 Optical and temperature dependent measurements. Method for determining thin film viscosity

For measurement of light intensities during kinetics' investigations of reflection, transmission, diffraction efficiency, I used a ThorLabs PM100 power meter connected to a PC.

In amorphous chalcogenide layers, absorption at a given wavelength increases with increasing temperature, due to optical absorption edge shift, so transmission and reflection measurements were made in a wide temperature range with a He-Ne laser probe beam (P= 0.01 mW, λ= 633 nm) in the spectral range of intermediate optical absorption of the film. This enabled the correction of the absorption coefficient for surface relief formation-erasing kinetics calculations.

For the chalcogenide thin film viscosity measurements I built an experimental setup, shown in Fig. 2.4. With this setup, I obtained data to calculate viscosity and diffusion parameters.

I investigated the mechanism of surface profile flattening (erasing) by measuring the diffraction efficiency ξ, as the intensity of the first order diffraction maximum reflected beam of a 2 mW 408 nm laser diode (spectral range of fundamental absorption) at constant temperatures. Using a 408 nm laser in pulse regime eliminated light penetration into the chalcogenide glass volume, thus it did not affect the measurement.

I investigated the erasing (flattening) kinetics of surface relief gratings at a 298–408 K temperature range at the selected constant temperatures. The measurements were completed both in dark and under illumination with a 635 nm multimode laser diode with up to 90 mW power. The illuminating light was guided to the chalcogenide surface via an optical system presented in Fig. 2.4. This system consists of a multimode fiber (2 m length, 400 μm diameter), focusing and collimating lens and a polarizer. The multimode fiber provided uniform *depolarized* light on the surface relief grating, since the diameter of the grating, d_g was much smaller compared to the illuminating beam diameter, D_B.

The flattening rates of polarized and depolarized beams were compared at the same light intensity, using a polarizer. To the grating

vector, the illuminating laser light had a 2° deviation from the normal plane. The parallel direction to the grating vector corresponds to *p*-polarization, while the normal to the grating vector corresponds to *s*-polarization.

A temperature rise and absorption change due to high light intensities (up to 2.5 W/cm^2) was included in the necessary calculations.

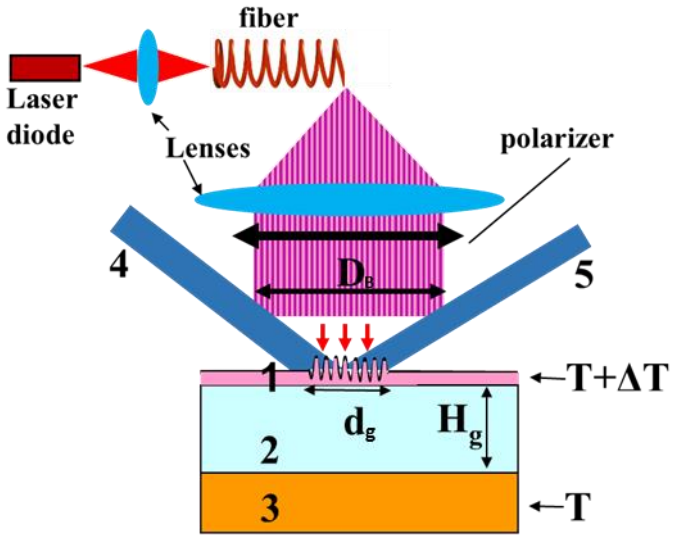

Fig. 2.4. *Grating erasing experimental setup: 1 – chalcogenide film with surface grating (d_g –grating diameter); 2 – glass substrate; 3 – heater, 4 – violet laser beam (λ=408 nm); 5 – first maximum of the diffracted beam, D_B – laser beam diameter [73].*

I carried out transmission measurements for thin chalcogenide and polymer-nanocomposite layers using a UV-VIS Shimadzu UV3600 spectrophotometer in a 300–2000 nm spectral range (example spectra shown in Fig. 2.5.). From these transmission measurements we can calculate the refractive index, thickness, other parameters of a thin film using the Swanepoel method [74]. Although a limitation for this method exists, that it is only usable for non-highly absorptive layers. For thick layers, it is necessary to use slit width correction.

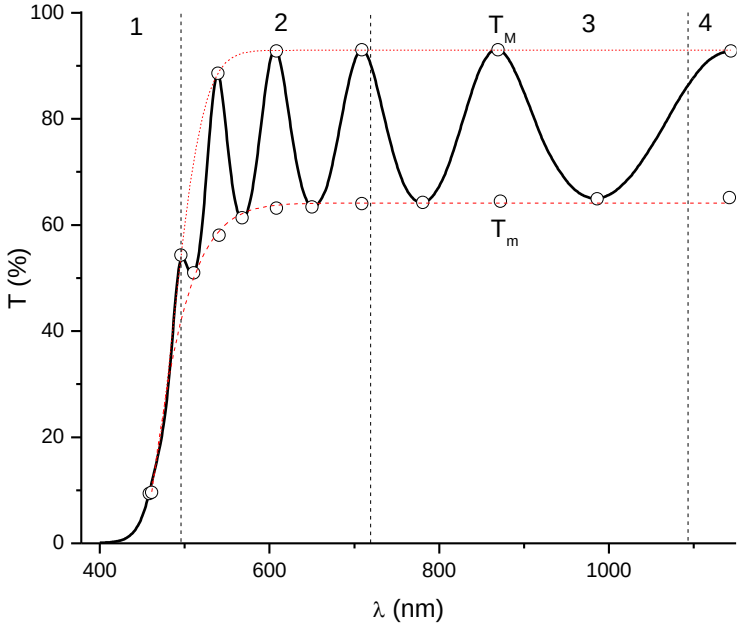

Fig. 2.5. *Transmission spectra of an As_2S_3 layer (regions: 4–transparent, 3–weak absorption, 2–medium absorption, 1–strong absorption).*

Regions of the not absorbing spectra with interference fringes can be used to calculate the optical parameters of the layer (Fig. 2.5.).

From the transmission spectra of a thin film, more precisely from the interference fringes, we get the formula for the layer refractive index *n* expressed as:

$$n = (N + (N^2 - s^2)^{1/2})^{1/2}, \tag{2.2}$$

where,

$$N = 2s\frac{T_M - T_m}{T_M T_m} + \frac{s^2+1}{2}, \tag{2.3}$$

where *s* is the substrate refractive index, T_s – substrate transmission,

$$s = \frac{1}{T_s} + \sqrt{\frac{1}{T_s^2} - 1}, \tag{2.4}$$

T_M and T_m are the maximum and minimum transmission for the interference fringe, respectively.

From the well-known equation for interference fringes

$$2nd=m\lambda. \quad (2.5)$$

Hence, the layer thickness d* can be calculated as:

$$d^* = \frac{\lambda_1\lambda_2}{2(\lambda_1 n_2 - \lambda_2 n_1)}, \quad (2.6)$$

where, n_1 ,n_2 are the corresponding refractive indices for λ_1, λ_2, (maxima or minima) adjacent fringes.

The absorption coefficient α can be calculated from the region of strong absorption of the transmission spectra:

$$\alpha(\lambda) = -\frac{1}{d}\, ln\frac{(n+1)^3+(n+s^2)}{16n^2s}\, T(\lambda). \quad (2.7)$$

Optical absorption above α >10^4 cm^{-1} can be calculated by the Tauc-method: [75]

$$\alpha = \frac{B(h\nu - E_g)^n}{(h\nu)^m}, \quad (2.8)$$

where $h\nu$ is the photon energy, E_g – band gap of the material, n, m and B – fitting coefficients. From this, we can find the band gap of the semiconductor. For indirect band gap semiconductor, using the Tauc-method [75]:

$$\sqrt{\alpha h\nu} = B(h\nu - E_g). \quad (2.9)$$

For permitted transitions in the indirect band gap n =1 and m= 1/2 and for direct band gap n=1 and m=2 [75].

2.4 Ion irradiations

Ion irradiation of chalcogenide glass samples was performed by focused 2 MeV energy He^+ and H^+ beams at ATOMKI Institute for Nuclear Research at the nuclear microprobe beamline of the Van de Graaff accelerator. The characteristics of the ion irradiation are the following: beam spot size 2–3 μm at FWHM (Full Width at Half Maximum), repetition rate of one pixel 200 μs for line scan and continuous irradiation for spot recording, beam current 80–1300 pA, ion fluence 100–300 000 nC/mm^2. To create surface structures on the chalcogenide samples, 1 pixel

dot matrix patterns and patterns of lines of various widths and spacings were recorded at 10^{-7} Torr pressure at room temperature.

I prepared polished glass plates, thick films on various transparent substrates, bulk cleaved blocks as media for ion beam induced surface recordings. The chalcogenide glasses (Se, As_6Se_{94}, $As_{20}Se_{80}$, As_2S_3, $As_{30}Ge_{20}S_{50}$) were chosen based on their efficiency for amplitude and/or phase optical- and e-beam recording found by previous investigations [76], [77],[78], [72].

The selected materials used for ion beam patterning were in different forms. The Se sample was a bulk mirror-like cleaved surface. Samples of As_6Se_{94}, As_2S_3, $As_{30}Ge_{20}S_{50}$ compositions were made into 1-3 mm thick plate form. Lastly, I used 25-35 μm thick films on silica glass and indium tin oxide (ITO) covered glass substrates, which I obtained by TVE method. Prior to chalcogenide layer depositions, I used SRIM (Stopping and Range of Ions in Matter) [79], [80] software by modelling ion propagation and penetration depth, to choose the necessary layer thickness to eliminate ion penetration into the substrate.

2.5 Surface investigations

To study surface reliefs, I used a Veeco diCaliber AFM in tapping mode. Average surface roughness was 3nm for layers under 3 μm thickness, 30 nm for thicker layers used for ion beam recording. For high resolution optical imaging I used a Zeiss AXIO Scope A1 microscope and for determining layer thickness and relief height for light or ion beam effect created structures, I used an Ambios XP-1 profilemeter.

3. Investigations of Amplitude and Phase Modulated Structures in Amorphous Chalcogenide Layers and Bulk Glasses

As it was mentioned in Chapter 1, the characteristics of photo-induced mass transport are still not fully understood: the effect of light and temperature during recording or erasing a surface relief, the role of material composition, polarization dependence of the mass transport direction, the common and different mechanisms of irradiation induced phase and amplitude modulated structure formation. In this chapter, I discuss the role of temperature and light during surface relief structure creation and erasing in As (Ge)-Se (S) based chalcogenide layers and glasses, the methods for determining photo-induced mass transport direction depending on chalcogenide glass composition, and compare efficiencies of high-energy ion beam surface relief recording with data on light induced recording.

3.1 Thermally and optically induced effects in chalcogenide layers and bulk samples

3.1.1 Thermal effects in amorphous selenium

To separate the light and thermally induced effects of mass transport, first I discuss the thermal effects of amorphous selenium, which is the simplest, low softening temperature (~410 K) chalcogenide glass possessing all the effects of induced transformations.

Thermal effects are typically ignored in chalcogenide bulk glasses and thin films during optical recording. Nevertheless, thermal effects can cause structural changes, melting or even phase change, as it is known in rewritable CDs or DVDs. Furthermore, the effect of temperature can change the direction of photo-induced processes like darkening-bleaching, recording-erasing surface reliefs, mass transport efficiency and viscosity. Crystallization can also be influenced by heat effects based on hetero- or homogeneous nucleation and following crystal growth [81].

For creating optoelectronic elements, the presence of crystalline phase could be a major negative factor, however, it could be used as a marker and developer of the hidden transformation mechanisms [82].

33 Thermally and optically induced effects in chalcogenide layers and bulk samples

To better understand the mass transport processes in optical relief recording, I investigated surface profiles created by focused laser beam on bulk amorphous selenium samples.

Raising the temperature above a critical level could initiate crystallization in amorphous selenium. In this case, photo-crystallization may not have the dominant role. Under gradient fields of light illumination, atomic movements and mass transport are accelerated, which at the same time can promote crystal growth from crystalline seeds [81]. The subsequent temperature increase and the growing number of defects can further help this crystallization process.

Different light intensities and irradiation times can be used to separate these effects, so at the same expositions (total energy), there could be different temperatures, which may reveal if crystallization only occurs in hot spots or whether it depends on photon-excited effects as well.

Various light intensities and illumination times were chosen for spot recording on bulk a-Se samples (S1 and S2, see the Appendix), so the temperature profiles could be estimated. a-Se was chosen as the investigated chalcogenide material, since in the As-Se system it has the lowest softening temperature [83], as well as it has a known tendency for fast crystallization. This method can be applied to As-Se compositions as well, regardless of the fact that with increasing As content, T_g rise and lack of crystallization effects can be observed [83]. Heating can still influence the relief recording in those material compositions.

The recorded spot, presented in Fig. 3.1a was created by a He-Ne laser beam, focused into a spot with 10 μm in diameter, with laser power 17.5 mW and illumination time 60 s onto the *S1* polished a-Se sample. With such intensity and illumination duration, crater formation was observed in the illuminated spot, with concentric waves of different surface levels, including a region with visible crystallites (Fig. 3.1a yellow rectangle). The created surface profile had a radius around 200-250 μm. Structural differences in the waves were revealed by micro-Raman spectroscopy (in detail will be discussed below), which were compared to the *S2* smooth surface sample as well (Fig. 3.1b). Additionally, recorded focused spots with different intensities (17.5 mW, 10mW, 6.5mW) with the same 60 s recording duration show (Fig. 3.1c) the profile evolution from light stimulated volume expansion to crater formation in the center of the illuminated region, and in Fig. 3.1d, I show the temperature model depending on the distance from the center of illumination.

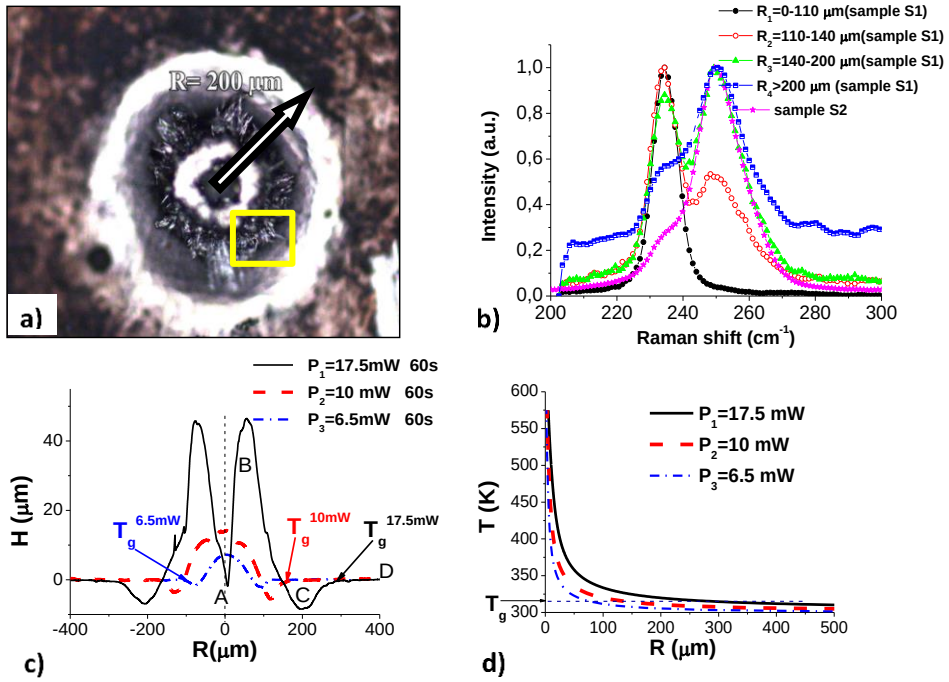

Fig. 3.1. *Focused laser beam created relief on bulk a-Se: a) optical picture of the created relief on S1 sample by He-Ne focused beam, 17.5 mW, 60s. Yellow rectangle shows crystalline region. b) micro-Raman spectra of the recorded spot on S1 sample (17.5 mW, 60s) at multiple distances from the crater center, comparison with unilluminated S2 sample. c) Created profiles by different expositions on S1 sample, measured by profile meter. d) Radial temperature profile of the illuminated spots on S1 sample (origin point is the beam center) [82].*

I performed profile meter measurements of the surface profiles recorded on the *S1* sample at different illumination intensities. These results are shown in Fig 3.1c. In Fig. 3.1c curve *1*, the solid (black) curve represents high heating (17.5 mW, 60s) with a crater region (Fig. 3.1c, region A), ring hillock (Fig. 3.1c, region B), ring well (Fig. 3.1c, region C) and free unilluminated surface (Fig. 3.1c, region D). The dotted (red curve, 10 mW, 60s) and dashed (blue curve, 6.5 mW, 60 s) curves represent low heating created profiles.

According to micro-Raman measurements, the crystallization occurred in the hillock region (Fig. 3.1c dotted and dashed curves, Fig. 3.1a yellow rectangle). Under the illumination process (see Fig. 3.1c), the

temperature gradient is oriented outward from the central region (region A) and when the crystalline region forms in the hillock (region B), it prevents the mass transport from the softer region of the ring well (region C), since crystalline selenium has lower diffusion coefficient than amorphous selenium [84]. Mass transport direction change from the ring well to the hillock is also possible, which may be connected to the softer structure and lower surface tension in the hillock.

The crater shown on Fig 3.1c (black curve) is the product of high temperature, where the material melts or even boils under high light intensities (see Fig. 3.1d). Mass transport is not analyzed in the crater region (up to 10–20 μm from the origin point, Fig. 3.1d), since the temperature is even higher than the glass melting point, 493K [81] or boiling point 958 K [85]. From the crater region towards the hillock region (crystalline region B) the effect of temperature increases diffusion and mass transport towards region B.

In the ring hillock (Fig. 3.1c region B), diffusion occurs from both sides towards the hillock center. Temperature in the ring well (Fig.3.1c – region C) is near the softening temperature of selenium (see Fig.3.1d). In this region, the conditions are possibly beneficial for revitrification. The ring well's inner side is softer compared to the exterior one. The diffusion direction is oriented from region C towards region B. The crystalline phase has lower diffusion coefficient than the glass phase, hence inverse diffusion is limited. Outside of the 10 μm spot there is no illumination absorbed, so the photoplasticity effect is excluded from the interpretation. From Fig. 3.1c,d we can see, that the temperature of the hillock ring is around 350 K. According to DTA (differential thermal analysis) or DSC (differential scanning calorimetry) this temperature is near the crystallization temperature of a-Se [86], [87], [88].

Micro-Raman spectroscopy showed that even in the unirradiated regions of *S1* and in the twenty-year-old smooth *S2* sample, which was used for comparison, there are low amounts of trigonal crystals (Fig. 3.1b, curve for *S2*). Such crystals can be seeds for crystallization, if excited by the necessary means. The *S2* smooth surface sample, with low amounts of surface defects and saturated bonds, is thermodynamically more stable compared to the *S1* sample's polished surface with induced defects (Fig. 3.1b, curve R_4>200 μm) [82]. Nevertheless, no crystalline phase was found investigating the deeper regions of the selenium samples by the micro-Raman measurements.

Further analyzing the micro-Raman spectra taken on the *S1* sample (Fig. 3.1a-b) we can see, that moving from the outer regions to the origin of the focused spot, the share of the crystalline phase increases. Outside of

the recorded spot, Se is completely amorphous with a Raman band at 252 cm^{-1}, but moving closer to the center spot, we can discover partially crystallized trigonal phase (232 cm^{-1}) and fully crystallized material in the center of the illumination [89].

Finally, to know the surface temperature under illumination without direct measurements, I modelled the temperature field around the illuminated spot. I used the following estimations:

1. All light in the illuminated spot is absorbed in a-Se sample at 3–5 μm depth (absorption is above 10^4 cm^{-1} for He-Ne laser emission in a-Se [90]).

2. The laser is focused into a 10 μm spot, which is an order of magnitude smaller than the radius of the created profile (R= 200–250 μm). The diameter of the focused beam is equivalent to the diameter of the softening/melting region in Fig. 3.1c.

3. The heat flux direction is only towards the chalcogenide.

Using semi-infinite bulk approximation, the calculations for heat conduction are valid for a semi-spherical temperature field outward a 5 μm region. For the temperature dependence on radius r> 5 μm, in a spherical coordinate system, I used following approximation:

$$P_{abs} = -2\pi \cdot k(T) \cdot r^2 \frac{dT}{dr}. \quad (3.1)$$

Here $k(T)$– Se thermal conductivity, which is temperature (T) dependent, P_{abs}– absorbed laser light power.

The boundary conditions for the temperature field are:

$$T \rightarrow T_r + \Delta T \text{ at } R \rightarrow \infty, \quad (3.2)$$

where T_r – room temperature, ΔT – light induced temperature increase in the chalcogenide glass. Moreover, the temperature rise is:

$$\Delta T = P_{abs} \cdot t/(m \cdot c), \quad (3.3)$$

where t – irradiation duration, m – chalcogenide mass, c – the specific heat of selenium. These calculations gave 3 to 10 °C temperature increase in the sample, depending on illumination intensity.

Thermal conductivity dependence for bulk a-Se (data from [91], [92]) can be fitted by the expression:

$$k(T) = \alpha + \beta \cdot T + \gamma \cdot T^2 + \delta \cdot T^3, \quad (3.4)$$

where $\alpha \approx -27 W \cdot m^{-1} \cdot K^{-1}$, $\beta \approx 0.21\ W \cdot m^{-1} \cdot K^{-2}$, $\gamma \approx -5.2 \cdot 10^{-4}\ W \cdot m^{-1} \cdot K^{-3}$, $\delta \approx 4.4 \cdot 10^{-7}\ W \cdot m^{-1} \cdot K^{-4}$.

The radial distribution of the temperature profile on bulk *S1* selenium sample has been calculated by solving Eq. (3.1) with boundary conditions Eq. (3.2) (shown on Fig. 3.1d). The known thermodynamical parameters, low T_g value, low crystallization thresholds for a-Se enables us to check the reality of modeling, i.e. to make conclusions about the sample temperature and role of possible heating during the optical recording process.

In Table 3.1. the comparison of the volume of the hillocks (ring hillock) and ring wells at different illuminating powers is shown. Around two times difference is noticeable while comparing the hillocks (hillock ring) to the ring wells, which suggest the crystalline phase in the hillock is porous. This is supported by the micro-cross section made on the hillock (Fig. 3.2a,c), where in the hillock region a large amount of microcrystals is shown.

Power (mW)	6.5	10	17.5
Volume of hillock (h) and hillock ring (hr) (μm^3)	45000 h	227000 h	1380000 hr
Volume of ring well (μm^3)	28000	127000	712000

Table 3.1. *Comparison of volumes of hillock (ring hillock) based on the data of Fig. 3.1c [82].*

For further technological applications, the use of smooth surface quenched glasses are more advisable, since polished a-Se samples may contain seeds of crystalline phase, in which the crystal growth is induced by mechanical and heat treatment [88] (Fig. 3.1b).

Increasing light intensity of the focusing beam leads to crater formation in the center of the a-Se glass, with material evaporation (Fig. 3.1c, solid curve). Evaporation is supported as well, by the calculated temperature profiles, shown in Fig. 3.1d. When irradiating with low light intensities, a bump profile is formed (Fig. 3.1c, dotted and dashed curves) with surrounding wells. These can be explained by lateral mass transport in gradients of temperature fields.

In the center of the illuminated spot on the bulk *S1* sample, the crystalline region appears much earlier than crater formation. At low

intensities, this results in an inflated hillock, which has porous crystalline structure as shown on Fig. 3.2. Only small, under 1 μm high bumps were seen to be amorphous, which is a known phenomenon, connected to photo-induced volume expansion [93].

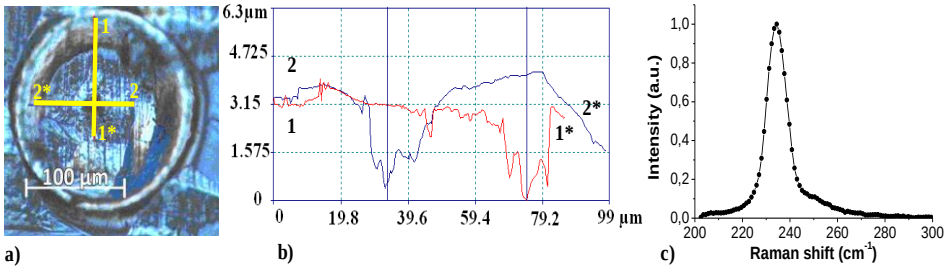

Fig. 3.2. *S1 Selenium sample. Optical picture (a) and the AFM profile of cross sections (1–1*, 2–2*) (b) of the cut hillock on bulk S1 sample, illuminated with focused He-Ne laser, 7.8 mW during 96 s. (c) Raman-spectrum [82].*

Such temperature effects should be considered during the formation of surface relief elements, like diffraction gratings or microlenses, since high intensity light illumination could erase the recorded relief or crystallization can occur, especially in low softening point materials, like the investigated a-Se.

Conclusion

I showed the surface relief creating effect of focused He-Ne laser beam on a-Se bulk selenium samples at different light intensities. This permitted the separation of the thermal effects from light stimulated ones, during the surface profile formation.

I fabricated the bulk samples by using polishing and molding methods and investigated the recorded surface profiles on them by using a profile meter.

I showed and modelled, that high intensity illumination can create a temperature field, in which mass transport and even crystallization can occur.

Material properties such as heat conductivity and softening temperature should be considered in recording experiments, to eliminate possible negative processes like crystallization and self-erasing.

Results of Chapter 3.1.1 are covered by thesis point 1.

These were published in:

[A1.] R. Bohdan, S. Molnar, I. Csarnovics, M. Veres, A. Csik, S. Kokenyesi, *Optical recording of surface relief on amorphous selenium*, J. Non. Cryst. Solids **408**, 57–61 (2015).

3.1.2 Separation of light and thermal effects during surface relief variations

Surface relief erasing measurements

In this subsection, I had the following goals: to show the possibility of measuring the viscosity of solid amorphous chalcogenide layers, to try to separate viscous flow from diffusion flow and define what mechanism occurs during surface relief grating erasing. Furthermore, to preferably separate light and thermally induced effects during the surface relief recording process.

Since there were no direct methods reported for measurement of viscosity of thin chalcogenide films, I present a viscosity determination method for thin amorphous layers and display it on thin $As_{20}Se_{80}$ films.

This method is based on measuring the flattening kinetics of a surface profile grating recorded on the surface of a thin film. The profile height (amplitude) of the recorded relief (grating) needs to be small regarding to the layer thickness. This theory for surface profile erasing was developed by Mullins [94] for bulk crystalline samples, in which he described four main flattening mechanisms: bulk diffusion, viscous flow, surface diffusion and evaporation-condensation. This theory was modified for thin film profile flattening [68].

For our experiments we usually recorded small period gratings with Λ= 1–5 μm, and large period gratings with Λ = 10–20 μm, since such were applicable earlier for modelling surface relief transformations [68]. For the following viscosity experiments I used two periods: 3.5 μm and 15 μm.

When the essential mechanism of the flattening process is viscous flow, the profile flattening can be expressed as:

$$h(t) = h_0 \exp(-\kappa \cdot t). \tag{3.5}$$

Here $h(t)$ is the profile amplitude at a given time, h_0 is the initial amplitude, κ is the flattening coefficient. κ depends on the mechanism of flattening and for viscous flow

$$\kappa = \mathrm{C} \cdot \pi \cdot \gamma/(\Lambda \cdot \eta), \tag{3.6}$$

where, Λ is the grating period, γ is the surface tension of the layer, η is the dynamic viscosity, and coefficient *C* depends on the *H*/*Λ* ratio [68], where *H* is the layer thickness. Coefficient *C* can be expressed as:

$$C = -\mathrm{e}^{4\pi \mathrm{H}/\Lambda} \cdot \frac{1+4\pi \mathrm{H}/\Lambda - \mathrm{e}^{4\pi \mathrm{H}/\Lambda}}{1+\mathrm{e}^{8\pi \mathrm{H}/\Lambda}}. \tag{3.7}$$

When *H* layer thickness was 2.3 μm, *C* = 1 for *Λ* = 3.5 μm period grating and *C* = 0.55 for *Λ* = 15 μm period grating, and when *H* was 2.6 μm, *C* = 1 for *Λ* = 3.5 μm period grating and *C* = 0.62 for *Λ* = 15 μm period grating.

From Fig. 3.3., we can see, that coefficient C becomes much less than 1, if the period of the profile, *Λ,* is much greater than the layer thickness *H*.

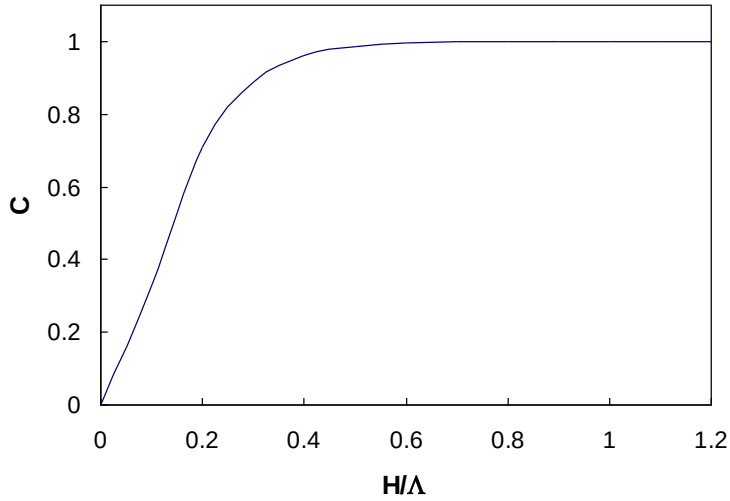

Fig. 3.3. *Coefficient C as a function of H /Λ [95].*

I studied the flattening rate of sinusoidal holographic gratings with 3.5 μm and 15 μm periods recorded by standard holographic setup on $As_{20}Se_{80}$ films. The experimental setups of holographic grating recording and the setup I built for the viscosity investigations is described in Chapter 2 (see Fig. 2.1. and Fig. 2.4.).

As stated by the diffraction theory [96], diffraction efficiency ξ depends on the *h*/*λ ratio*:

$$\xi = J_1^2(2\pi h/\lambda), \tag{3.8}$$

where $J_1(x)$ is the Bessel function of the first kind, h is the grating amplitude and λ is the light wavelength. If the grating amplitude is small, ξ is proportional to h^2. In the investigated layers the initial amplitude was about 300 nm. Thus, I investigated the flattening of the holographic gratings over time by measuring the diffraction efficiency at various temperatures. Plotting ln ξ (diffraction efficiency) over time shows linear dependence for both investigated periods, according to Eq. (3.5), shown in Fig. 3.4.

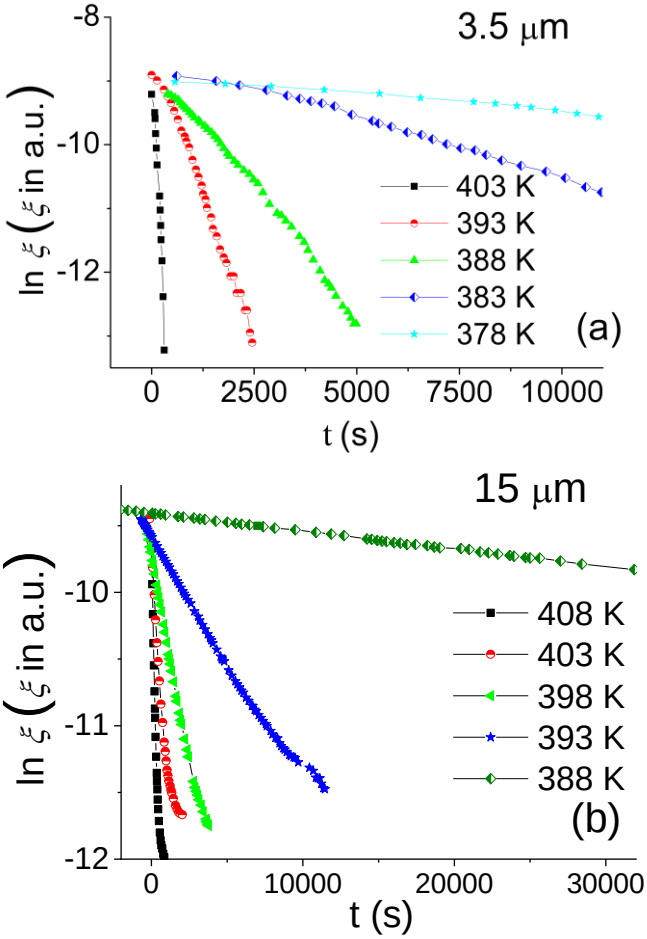

Fig. 3.4. *Dependence of ln ξ (diffraction efficiency) from time for various temperatures for two grating periods: (a) Λ = 3.5 μm, (b) Λ = 15 μm [95].*

According to the capillary flattening theory [68], [94], the flattening coefficient κ, depends on the grating period, Λ. For viscous flow κ is proportional to Λ^{-1} (see Eq. 3.6), while for bulk diffusion it is Λ^{-3} and Λ^{-4} for surface diffusion. For both grating periods of 3.5 and 15 μm I used in the surface pattern erasing experiment in darkness, $\kappa(\Lambda)$ is described by Eq. (3.6) so the erasing process is viscous flow, $\kappa \sim \Lambda^{-1}$.

Calculating viscosity coefficients η for both investigated periods using Eq. (3.6) and data from Fig. 3.4., surface tension, $\gamma = 0.13$ J/m^2 [97], layer thickness 2.6 μm, $C = 1$ for $\Lambda = 3.5$ μm grating, $C = 0.62$ for $\Lambda = 15$ μm grating (from Fig. 3.3.), the results coincide with one another. The data is presented in Arrhenius coordinates in Fig. 3.5. In the measured temperature range of 378–408 K, viscosity, η was obtained in the range of $3\times10^7 - 10^{10}$ Pa·s, with $E_\eta = 2.9$ eV activation energy [95]. The effect of light on the grating erasing will be discussed in the next section.

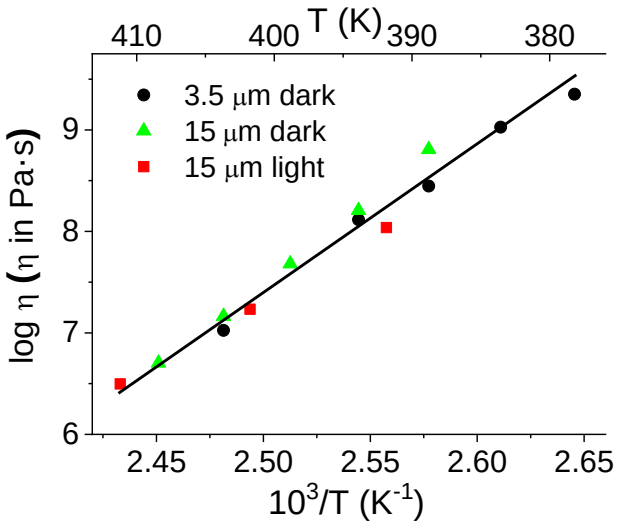

Fig. 3.5. *Viscosity coefficients of $As_{20}Se_{80}$ layer for grating periods of Λ =15 μm and 3.5 μm. Λ =15 μm under p-polarized light illumination, I = 1.2 W/cm^2 [73].*

Literature data shows [98], [99], [100], [101], that viscosity for the bulk $As_{20}Se_{80}$ glasses is 2–5 times larger [95], compared to the investigated thin films, which may be caused by differences in the microstructure of bulk and thin films. This difference in viscosity supports the developed method to be used for direct viscosity measurements for different thin

chalcogenide films, since thin film properties may vary on the creation circumstances.

It should be mentioned, that viscosity activation energy decreases with temperature as:

$$E_\eta = H_\eta - TS_{\eta,} \tag{3.9}$$

where H_η is the activation enthalpy and S_η is the activation entropy of viscous flow. The activation enthalpy, H_η does not depend on temperature, although TS_η does and shows the quirks of viscous flow's cooperative nature.

Surface relief erasing measurements under light illumination

The main question after these experiments was how does band gap light effects the viscosity of chalcogenide layers at high temperatures, and whether it changes the mechanism of thermal flattening. Therefore, I complemented the experimental setup presented on Fig. 2.4. with a red diode laser.

However, the effect of light induced temperature rise had to be considered in the calculations. The temperature increase ΔT is proportional to I_{abs}, intensity of the absorbed light. This absorbed power is dissipated by heat flow from the chalcogenide layer to the silica substrate. Linear temperature rise was assumed from the film surface to the heater (see Fig. 2.4.), considering the laser beam light diameter, D_B on the surface was much larger than the substrate thickness H_g. The heat flux to the heater from the chalcogenide layer can be expressed as:

$$J = \kappa_g \cdot \Delta T / H_g, \tag{3.10}$$

where κ_g is the glass substrate heat conductivity. Equating heat flux, J to absorbed light intensity, I_{abs}, ΔT temperature rise is:

$$\Delta T = I_{abs} \cdot H_g / \kappa_g. \tag{3.11}$$

Transmission and reflection measurements were made in 298 – 408 K temperature range to calculate the absorbed light power in the chalcogenide layer at various temperatures. Transmission varied from 13 to 3%, since absorption is higher at higher temperatures and reflection varied from 21 to 22 % using 100% as the incident light intensity. Considering these "losses", the absorbed light in the ChG layer was 70% of the initial light intensity.

Hence, $I_{abs} = \alpha_{abs} \cdot I$, where I is the incident light beam intensity, $\alpha_{abs} \approx 0.7$ is the absorbed light in the layer, H_g = 1.1 mm and $\kappa_g \approx 1$ W/m·K, we get 0–20 K temperature rise depending on 0–2.5 W/cm^2 incident light intensity, respectively.

From Fig. 3.5. we can see that the viscosity coefficients match each other for both periods. Even for the 15 μm period under light illumination (1.2 W/cm^2) in a high temperature range, near the softening temperature of $As_{20}Se_{80}$ chalcogenide glass. This suggests that the erasing kinetics has a viscous flow character. The calculated activation energy was 2.9 eV.

Flattening kinetics of gratings also depends on temperature, light polarization and intensity. Comparing slopes in Fig. 3.6., the band gap light did not influence strongly the erasing process for the 15 μm grating. The slightly faster flattening here is caused by the light induced temperature rise. However, for the 3.5 μm period, the flattening rate is much faster under illumination (Fig. 3.6a).

Analyzing Fig. 3.6. we can see, that $\ln\xi$ is still linearly dependent on time, but the flattening constant, κ, increases with illumination for 3.5 μm gratings. In this case $\kappa(\Lambda)$ is close to $\kappa \sim \Lambda^{-3}$, as it would be for bulk diffusion mechanism, not $\kappa \sim \Lambda^{-1}$ as for viscous flow. However, comparing directly the flattening rates for 3.5 μm and 15 μm gratings was not possible under 380 K, since at lower temperatures the erasing process for the larger grating period did not show any significant changes in diffraction efficiency, even after a 50 hour period.

Since band gap light has no effect on the flattening constant κ for 15 μm gratings, it is possible that "pure" coefficients of viscosity are illumination-independent, they do not change under band gap light. At the same time, illumination can induce diffusion in the mass transport process, and can change the effective (diffusional) viscosity.

Considering both mechanisms of viscous flow and bulk diffusion, the flattening constant can be rewritten as [96], [97]:

$$\kappa = C\frac{\pi\gamma}{\Lambda\eta} + B\frac{8\pi^3 D\gamma\Omega}{\Lambda^3 kT} = C\frac{\pi\gamma}{\Lambda\eta_{eff}} \qquad (3.12)$$

Here $B = 1 - \mathrm{e}^{-2\pi \mathrm{H}/\Lambda}$, D is the effective coefficient of diffusion, which defines mass transfer kinetics, Ω is the average atomic volume, k is the Boltzmann constant, and T is the absolute temperature. Here, η_{eff} can be regarded as "diffusional viscosity".

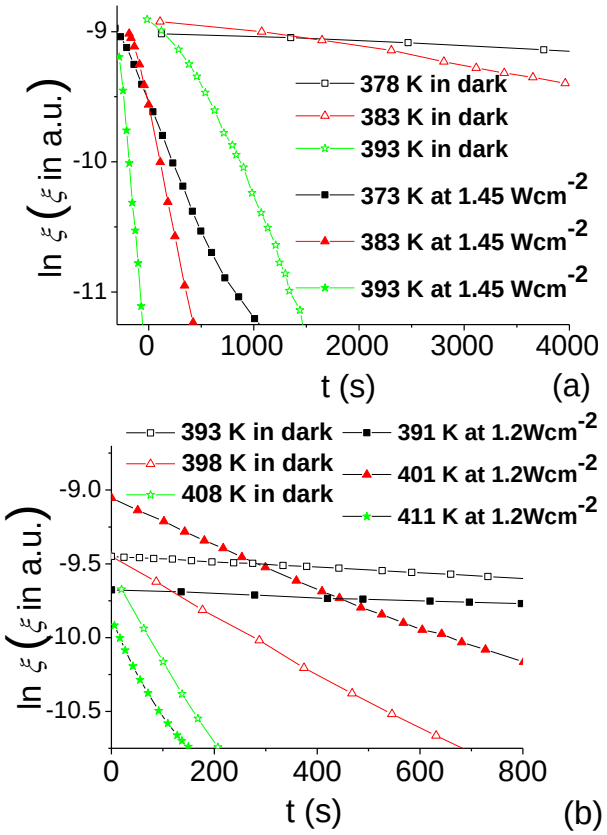

Fig. 3.6. *Flattening rates (diffraction efficiency coefficient vs time) in dark and under p-polarized illumination at different temperatures for gratings with periods of 3.5 μm (a) and 15 μm (b) [73].*

From Fig. 3.6. we see that the flattening rate is much higher under illumination than in the dark for the 3.5 μm grating, so it is logical, that the second term in Eq. (3.12) is much larger than the first term. This way, the effective coefficient of viscosity *D* can be separated and expressed as:

$$D = \frac{C}{B}\frac{\Lambda^3 kT}{8\pi^2 \Omega}\left(\frac{1}{\eta_{eff}} - \frac{1}{\eta}\right). \tag{3.13}$$

When $\eta_{eff} << \eta$, the photo-induced diffusional viscosity coefficient can be calculated as

$$\eta_{eff} = \frac{C}{B}\frac{\Lambda^2 kT}{8\pi^2 \Omega D} \tag{3.14}$$

With Λ = 3.5 μm, $\Omega = 2\times10^{-29}$ m^3, $C/B \approx 1$, 370 < T <390 K, and $10^{-13} < D < 10^{-12}$ m^2/s, we get $4\times10^7 < \eta_{eff} < 4\times10^8$ Pa s for the effective viscosity coefficient, which is smaller from the real value of viscosity by one order of magnitude at same temperatures.

From the Stokes-Einstein equation, η_{SE} viscosity coefficients can be expressed as:

$$\eta_{SE} = \frac{kT}{6\pi r_m D} \tag{3.15}$$

Here, the equivalent effective viscosity for the same coefficient D (r_m, moving species radius in viscous medium) is seven orders of magnitude smaller compared to the effective viscosity, $\eta_{eff.}$ This means Eq. (3.15) is not valid for amorphous solids.

Next, I investigated the effect of light polarization on the flattening

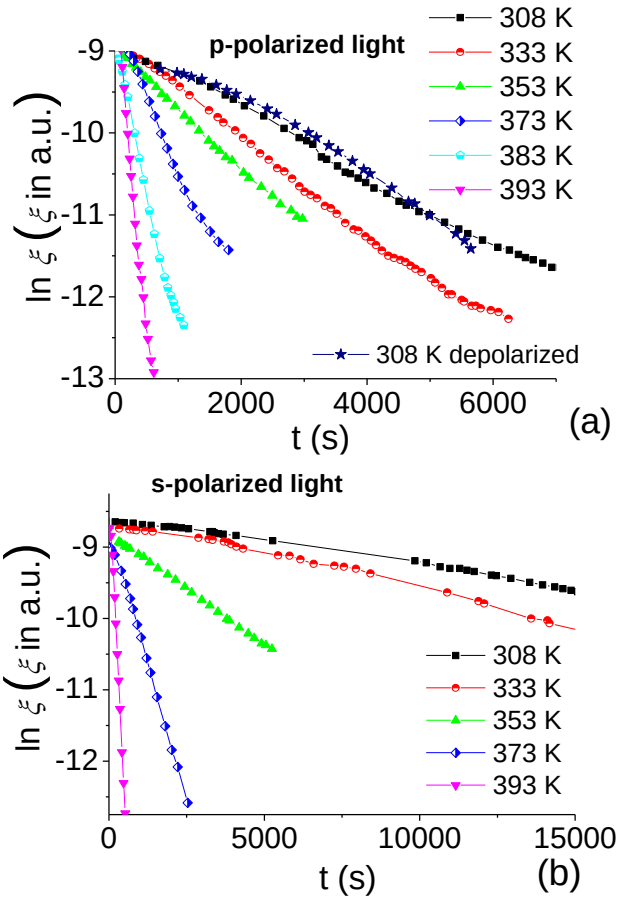

Fig. 3.7. *Flattening kinetics of the 3.5 μm grating under p-polarized light (a) and s-polarized light (b) illumination. Light intensity is 1.45 W/cm^2 [73].*

rate of a 3.5 μm period grating under *s*-, *p*- and depolarized light with intensities up to 2.5 W/cm^2 at various temperatures between 300 – 403 K (Fig. 3.7).

Considering the flattening rates under illumination are much higher compared to the flattening rates of unilluminated surface relief gratings and using Eq. (3.12) and (3.13), I calculated the photo-induced diffusion coefficient, *D*, as shown in Fig. 3.8.

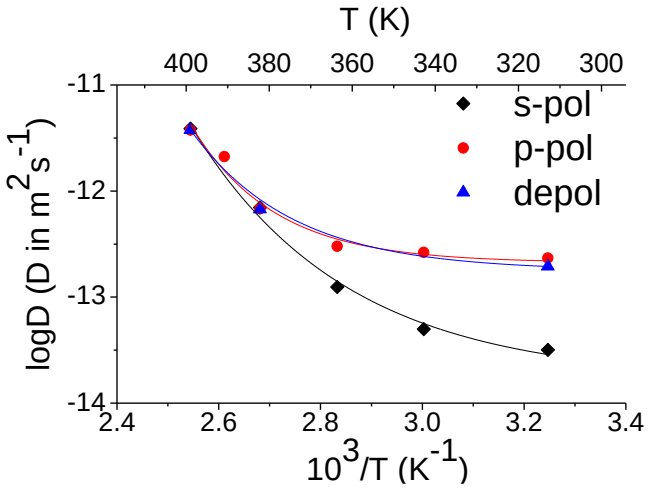

Fig. 3.8. *Temperature dependence of effective diffusion coefficients under s-, p-polarized and depolarized light illumination. Λ = 3.5 μm, I = 1.45 W/cm^2 [73].*

As shown in the figure, the temperature dependence of the photo-induced diffusion coefficients are demonstrated in Arrhenius coordinates. In a temperature range of 300 – 330 K, Q_D, the effective activation energy of photo-induced diffusion is 0.1 – 0.2 eV. In the temperature range of 373 K– 393 K it increases up to 1.1eV. It is important to mention, it is first time observed, that Q_D increases significantly in the mass transport with increasing temperature.

Q_D values of 0.09 eV were obtained by our earlier investigations on surface relief grating recordings at low temperatures (77–300 K) [66]. This low value was explained as electric interaction of charges near radiation defects, surrounded by diffusing atoms. Coulomb interaction lowers the potential barriers compared to ordinary diffusion barriers. These potential barriers can be overcome at higher temperatures, where point radiation defect decay is joined with atomic jumps. With temperature, the likelihood of these jumps is increasing, as is the effective diffusion activation energy.

From Fig. 3.8. it is also visible, that with increasing temperature, the difference in the coefficient of effective diffusion under *p*- and *s*-polarized light becomes less and less, and reaching the glass softening temperature it disappears, since the glass undergoes a structural transformation.

In Fig. 3.9., the temperature dependence of the effective viscosity coefficients are presented in Arrhenius coordinates for the 3.5 μm period grating in the dark and under band gap depolarized light illumination. I calculated the effective (diffusional) viscosity using Eq. (3.12) for depolarized light (very similar to *p*-polarized light). As we can see from Fig. 3.9., with increasing light intensity the effective viscosity decreases [73].

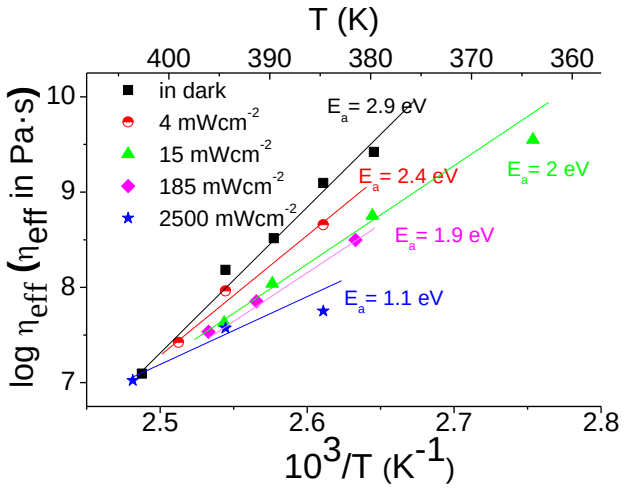

Fig. 3.9. *Effective viscosity coefficient dependence on light intensity (depolarized light) at different temperatures. Effective activation energies of* η_{eff} *are shown [73].*

Decrease in the activation energy with increasing light intensity is caused by the increasing contribution of the photo-induced diffusion process into the flattening mechanism. In the dark, the mechanism of the flattening process is viscous flow with 2.9 eV activation energy. With light illumination increment, the diffusion contribution increases in the flattening process, and becomes close to the effective activation energy of the photo-induced diffusion at the related temperatures.

Based on these results, stability of holographic or other surface relief structures can be estimated.

Conclusions

I developed a method for determining the effective viscosity of thin amorphous chalcogenide layers through the relief erasing process in dark and under illumination.

I deposited the chalcogenide layers, using TVE method, recorded surface holograms and investigated them with AFM. Furthermore, I designed and built the experimental setup for the erasing measurements, performed the diffraction efficiency measurements and calculated the viscosity and diffusion parameters.

I showed that the rate of erasing of a surface profile exponentially depends on the time, and the grating period Λ. Based on this, the flattening mechanism was found.

Erasing rate of a surface profile in the dark depends on Λ as Λ^{-1} and under light illumination as Λ^{-3}. Without light illumination, the erasing mechanism is viscous flow, while under light illumination, the diffusion flow mechanism appears.

The activation energy of viscous flow is illumination independent for the 15 μm grating, and equals 2.9 eV. For the 3.5 μm period grating it does depend on light intensity and polarization, and depending on light intensity it decreases to 1.1 eV.

I found and separated the viscous and diffusion flow components of grating erasing in thin $As_{20}Se_{80}$ layers. The presented method is applicable for determining viscosity for light sensitive amorphous films.

Results of Chapter 3.1.2. are covered by thesis point 2.

These were published in:

[A2.] S. Molnar, R. Bohdan, V. Takats, Y. Kaganovskii, S. Kokenyesi, *Viscosity of As20Se80 amorphous chalcogenide films*, Mater. Lett. **228**, 384–386 (2018).

[A3.] S. Molnar, R. Bohdan, V. Takats, Y. Kaganovskii, S. Kokenyesi, *Stimulated Surface Relief Erasing in Amorphous As-Se Layers: Thermal- and Light Induced Effects*, Phys. Status Solidi Appl. Mater. Sci. **215**, 24, 1–7 (2018).

3.2 Determination of the direction of mass transport

As it was mentioned in Chapter 1, discrepancies exist in the description of irradiation-induced mass transport processes. Their nature, driving forces and even the direction, i.e. from illuminated regions toward dark regions or vice versa, are described as different. Therefore, in this section I present two simple methods that I developed to investigate *in situ* the direction of photo-induced mass transport during surface relief grating recording in different compositions from the As_xSe_{100-x} system (x=1, 3, 6, 20, 40).

In the *first method,* I investigate the kinetics of holographic grating formation, recorded (see Fig. 2.1. and 2.2.) on the middle borderline of the sample, where the adjacent chalcogenide layers with different compositions are meeting, one with known and another with unknown direction of mass transport.

Surface relief formation usually starts with volume expansion in chalcogenides, and it is followed by mass transport. Accordingly, after 10–30 s of recording a surface relief hologram on the adjacent Se and As_xSe_{100-x} layer junction, the recorded reliefs are in the same phase (Fig. 3.10a), as at this stage only volume expansion happened, which was expected for all these glasses. The AFM picture of the connected layers is presented in Fig. 3.10.

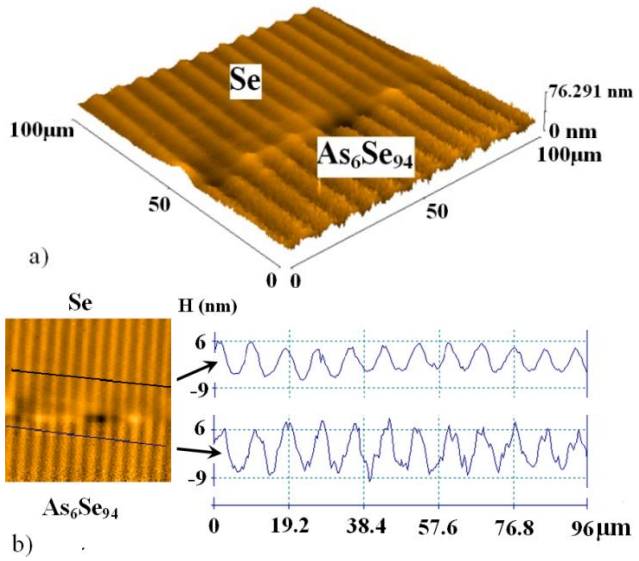

Fig. 3.10. *Holographic grating in the junction region between an As_6Se_{94} and Se layer (recording time: first 15 s): a) 3D AFM image b) 2D AFM image and cross section of the junction region from As_6Se_{94} layer to Se layer [72].*

However, the AFM picture of Fig. 3.11. shows, that after longer recording of the holographic gratings, the created structures of Se and As_xSe_{100-x} (for x>1) layers are in opposite phases.
In Fig. 3.11., larger grating amplitude for As_6Se_{94} layer than Se layer is caused by different layer thicknesses: 5 µm and 2 µm respectively, as well as slightly higher light absorption for As_6Se_{94}. Nonetheless, sensitivities for these materials are rather similar [76].

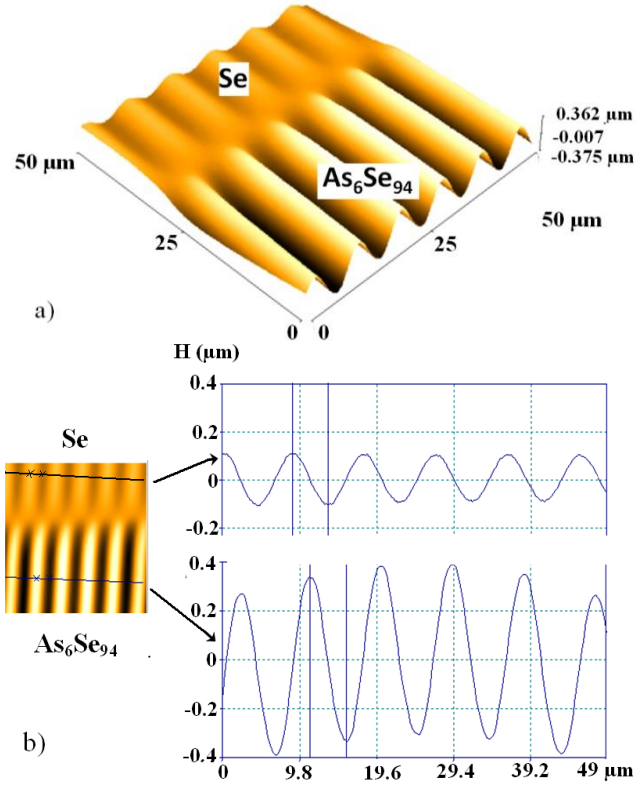

Fig. 3.11. *Holographic grating in the junction region between an As_6Se_{94} and Se layer (recording time – 6 hours): a) 3D AFM image b) 2D AFM image and the cross section of the junction region from As_6Se_{94} layer to Se layer [72].*

To compare the grating recording efficiency between the investigated chalcogenide glasses, I used the grating amplitude for comparisons at the same conditions. I measured the grating amplitudes with an AFM in tapping mode. Thus, I calculated the relative efficiency for relief recording (RERR) in As_xSe_{100-x} layers (Fig. 3.12.) as:

$$RERR = \frac{GA^*(As_xSe_{100-x})}{GA^*(Se)} \quad (3.16)$$

Here, *GA** means the grating amplitude for the appropriate layer divided by the absorbed light intensity in that layer. This eliminated the problem of different layer thicknesses of the investigated chalcogenide layers.

From Fig. 3.12. we can see, that according to the investigations, highest efficiency of recording was achieved for the As-Se layer with 20% of As content, as it was reported by other investigations, i.e. in Ref. [102]. Interestingly, there was no measureable mass transport around 1 at% of As content in the As_xSe_{100-x} layer [72].

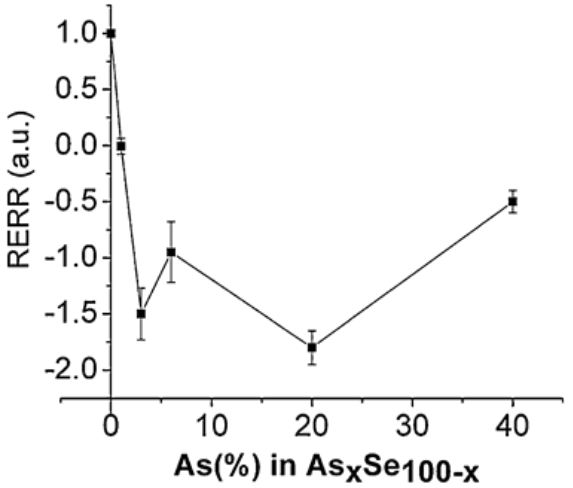

Fig. 3.12. *Relative efficiency of relief recording caused by mass transport in various As_xSe_{100-x} based layers (compared to Se). Negative sign shows opposite mass transport direction to Se [72].*

After this, with the *mesh mask method*, I used the diffraction pattern created by laser irradiation from the perpendicular edges of the metal mask as a tool for relief recording efficiency measurements. With this simple method, I determined the direction of mass transport of selected chalcogenide materials (Se, $As_{20}Se_{80}$, As_2S_3) and its dependence on light polarization conditions. The experimental setup is shown in Fig. 2.3., and the results are shown in Fig. 3.13.

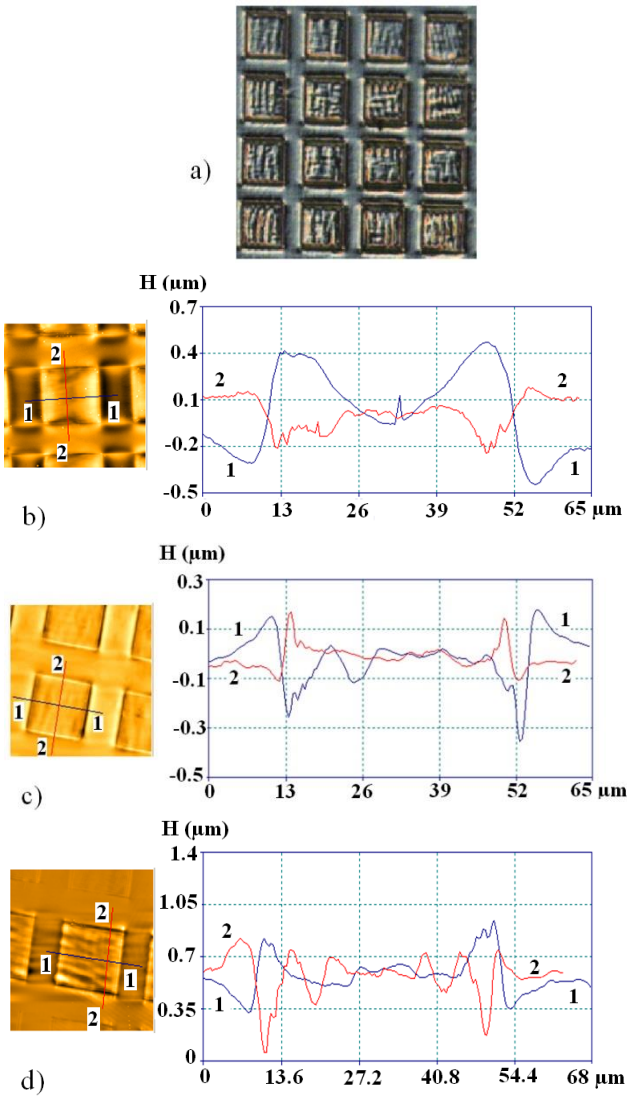

Fig. 3.13. *AFM picture and surface reliefs created by the mesh mask method: a) optical image of $As_{20}Se_{80}$ layer with mesh mask pattern b) AFM and surface profile of $As_{20}Se_{80}$ layer; c) AFM and surface profile of a-Se layer; d) AFM and surface profile of As_2S_3 layer. Laser beam polarization (front side- horizontal, back side-vertical). Note, that the vertical and horizontal cross sections of the surface profile on $As_{20}Se_{80}$ and As_2S_3 layer have similar mass transport directions [72].*

We can see, that for the $As_{20}Se_{80}$ layer, the first AFM profile (Fig. 3.13b, profile *1*) shows opposite material direction to the first AFM profile

measured on Se (Fig. 3.13c, profile *1*). The direction is opposite as well, for AFM profile *2* for the mentioned two layers. At the same time, we can see, that AFM profile *1* for the $As_{20}Se_{80}$ layer corresponds to profile *2* for the Se layer. This means, that the photo-induced mass transport direction is opposite in these two compositions at the same recording conditions. This is in agreement with the results of the "adjacent layers" method. Additionally, the mass transport direction is equivalent in As_2S_3 and $As_{20}Se_{80}$ layers (Fig. 3.13b, d).

The two developed methods can display the differences in light-stimulated mass transport caused surface relief formations for the As-Se system and for As_2S_3 layers as well.

The elimination of light stimulated mass transport effect in As-Se compositions around 1 at% As addition may be connected to the different electron-hole lifetime and mobility properties in the investigated compositions. Chalcogenides are usually known as p-type semiconductors, but in selenium, electrons and holes have comparable role in electrical transport and generation-recombination processes, i.e. the drift mobility for electrons is around $5 \cdot 10^{-3}$ $cm^2/V \cdot s$ and for holes it is around 0.2 $cm^2/V \cdot s$ [75]. However this can change under light illumination, where values of electron and hole mobilities for selenium were reported as 0.32 and 0.15 $cm^2/V \cdot s$, respectively [103]. Thus, under illumination Se behaved like an n-type semiconductor.

As investigated in [8], atomic movements are influenced by built-in electric and stress fields, light illumination, which creates electron-hole pairs, defects and mass transport. In the presented case, the difference in built-in polarizations and electric fields may be decisive.

The developed experimental methods can be used for a wide variety of chalcogenides or polymers, other light sensitive thin film or bulk materials. They could help uncover the peculiarities of the mass transport process, and provide quick and unique modes for investigating unknown samples.

Conclusions

I developed two experimental methods for investigating light stimulated mass transfer in As-Se (S) chalcogenide thin films. These methods show in situ, that light induced mass transport direction is based on the material composition and recording light polarization.

For these investigations, I developed the deposition setup and deposited the thin chalcogenide films by TVE method. I recorded the

surface reliefs on the thin layers and investigated the created profiles by AFM.

I showed, that depending on the composition in the As-Se system, optically induced mass transport can be eliminated at 1 at% of As, which may be connected to the electric characteristics of the charge carriers.

The mesh mask method can be used for simplifying more complicated experimental setups.

Both methods are improved, simpler in comparison with the previous existing ones for in situ investigations of mass transport, and can help finding efficient compositions for optical elements.

Results of Chapter 3.2. are covered by thesis point 3.

These were published in:

[A4.] R. Bohdan, S. Molnar, S. Kokenyesi, *Methods comparing peculiarities of surface-relief recording in amorphous chalcogenides*, Phys. status solidi **212**, 10, 2186–2190 (2015).

3.3 Ion beam induced changes and relief recording

My goal was to show the similarities and differences between surface relief structure creation by light irradiation and ion irradiation, since geometrical structures can be created this way and optical properties of the chalcogenide layers can be changed as well. 2 MeV energy proton and He^+ ions were used on selected chalcogenide samples (described in Chapter 2 and in the Appendix), since there are no experimental data for our materials at these energies. At the same time, such ion beams were used for lithography and waveguide creation in organic resists [104].

As mentioned in Chapter 2, the chalcogenide layer thicknesses were chosen after SRIM simulations, to prevent ion implantation to the substrate. Hence, for As_6Se_{94}, the penetration depth for 2MeV energy He^+ ions is 7.32 μm (Fig. 3.14.), and the layer thickness was chosen accordingly for this and other investigated samples as well.

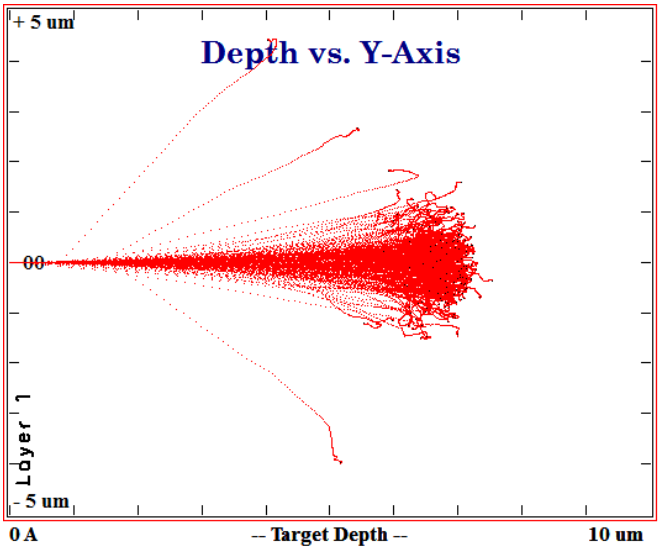

Fig. 3.14. *SRIM simulation of 2 MeV energy He^+ Ion beams into As_6Se_{94} layer [80].*

When low weight ions with MeV energy penetrate the chalcogenide glass, they lose energy by the electronic stopping power. Meaning, the energy is spent to ionize and excite the electrons in the layer. Nuclear energy transfer is negligible in this case [105]. This gives us the opportunity to compare the effect with light or electron induced recording effects, where electron-hole pair creation-recombination plays an important role [4], [106],[68], [77].

2 MeV H^+ or He^+ ion irradiations were used in the initial experiments. To create geometric reliefs, *spot* (or multiple spots) or *line* (or multiple lines) type patterns were recorded on As-Se samples with various ion fluences (in nC/mm^2 units), which I chose depending on what type of material, pattern and ion beam was used (see Fig. 3.15a–c).

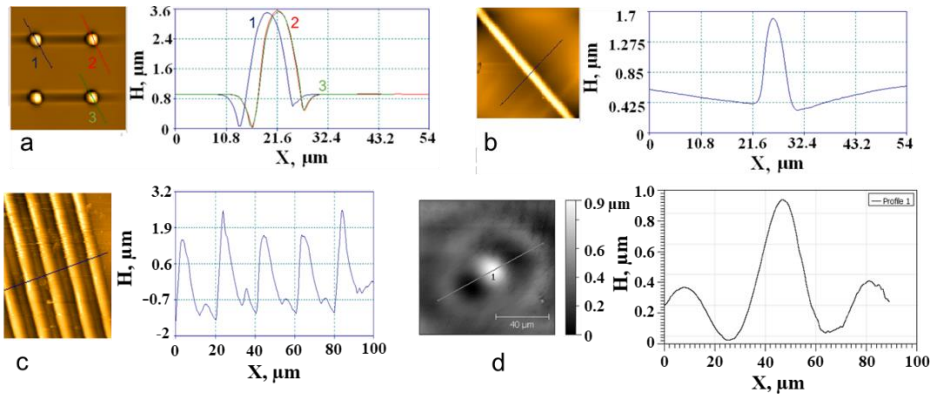

Fig. 3.15. *AFM picture of created patterns on ChG surface. a) Spots on a-Se (ITO substrate), He^+ ions (2 MeV, I_B=80pA), 0.18 nC irradiation dose (0.36 mJ) b) Line on As_6Se_{94} layer (glass substrate), H^+ ions, 40000 nC/mm^2 irradiation fluence; c) Grating (multiple lines) on a-Se, He^+ ions. d) Surface profile recorded by He-Ne focused beam on $As_{20}Se_{80}$ layer (absorbed power around 0.3mW, exposure 0.54 J) [80].*

Analyzing Fig. 3.15a, we can see that the created relief is similar to that of Fig. 3.15d, in which the effect of a focused light beam is shown on an $As_{20}Se_{80}$ layer. The latter was created for this comparison. Both are the result of mass transport. In the ion beam's case, there is groove formation around the relief hump, which means that the material moved from non-irradiated regions to irradiated ones. Additionally to the light and ion induced relief formation experiments, data was also analyzed on electron beam created reliefs [77], [107].

For the following relief recording experiment, I chose various distances (periods) between the recorded lines to eliminate possible interactions between the created structures. For He^+ ion irradiation 20 and 100 μm period line patterns, for H^+ ions 200 μm period line patterns were used. Comparing line heights by 2MeV He^+ irradiation created patterns on Se, As_6Se_{94} and As_2S_3 bulk glasses, the relief height proved to be almost twice as high for the 100 μm period, than for the 20 μm period pattern. The lower relief height in the more close-packed patterns may be linked to charging effects in the chalcogenide sample [108].

Most of the experiments on relief creation efficiency were done at similar irradiation conditions on selected thick As-Se (S) and As-Ge-S glass plates, as shown in Fig. 3.16.

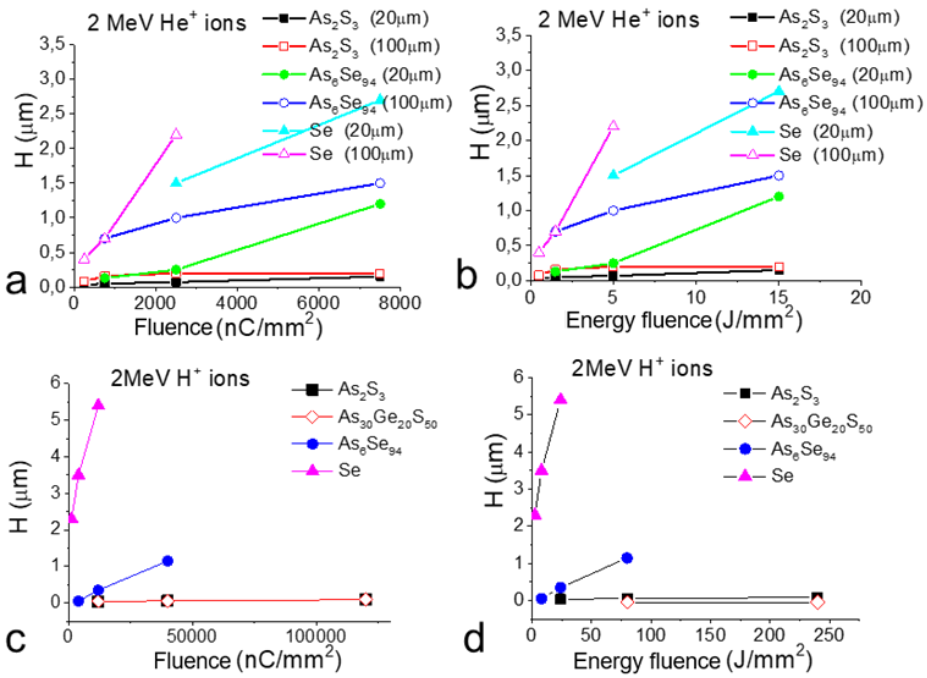

Fig. 3.16. *Line height on ChG surface, depending on the composition, irradiating ions (H^+ and He^+), line distance (20 μm and 100 μm) and irradiation fluence (in nC/mm² and J/mm²). a, b – He^+ ions, c, d – H^+ ions [80].*

Highest efficiency of proton and He^+ beam relief creation was achieved on a-Se (Fig. 3.16.), which has a good correlation with the patterning efficiency with light, as seen during preceding experiments [76],[72]. However, because of selenium's tendency to crystallize, more stable materials are needed for optical elements. Thankfully, more stable glasses can be created based on a-Se, by addition of arsenic to the network. Both As_6Se_{94} and $As_{20}Se_{80}$ are stable materials, with higher T_g, compared to pure selenium, and quite similar optical relief recording efficiency can be achieved on them. On the other hand, in As_2S_3 and $As_{30}Ge_{20}S_{50}$ glass plates, recording efficiency was the lowest between the investigated materials (Fig. 3.16.). Still, the use of these sulphides could be important, if wider optical transparency in the visible spectra, higher softening temperatures and thermal stability would be required.

Material properties like rigidity, T_g, heat and electrical conductivity could be the reason behind the various patterning efficiencies between the investigated glasses.

Selenium and As-Se compositions have floppy structures, with an average coordination number of 2–2.2. The structure of As_2S_3 and Ge containing glasses is more rigid, with germanium containing glasses having an increased average coordination number above 2.4. Even bonding energies are lower in the As-Se system compared to the bonds predominant in As_2S_3 and $As_{30}Ge_{20}S_{50}$ glasses [109].

Regarding ion beam efficiency, first the heating effect of the ion beam has to be analyzed. This temperature rise could cause viscosity drops, which accelerates mass transport and increases pattern height, as investigated in [67], [73]. The temperature rise could be negligible for high T_g glasses like As_2S_3 or $As_{30}Ge_{20}Se_{80}$, if the recording is made at room temperature or below it. However for selenium, which has low softening temperature of around 40 °C, it could cause a significant addition to the patterning efficiency. In the case of selenium, reaching temperatures above T_g is also problematic, since this could erase the recorded relief [73]. Local temperature measurement could not be done during recording (ion or light), so I calculated the possible temperature rise in the chalcogenide glass.

For He^+ ion beam irradiation with 80 pA beam current and 2 MeV energy, the total absorbed power is 0.16 mW in a Se layer (Fig. 3.15a), beam diameter 2.5 μm, penetration depth 8 μm. Regarding relevant light absorption in a very similar $As_{20}Se_{80}$ layer (Fig. 3.15d), by a He-Ne light beam focused into a 2–3 μm in diameter spot, was 0.3 mW. Using Eq. (3.1) and a minimal radius of 10 μm, above where a thermal sphere model is applicable (see Fig. 3.17.), the glass substrate thickness is much larger than the layer thickness, and the temperature increase can be calculated.

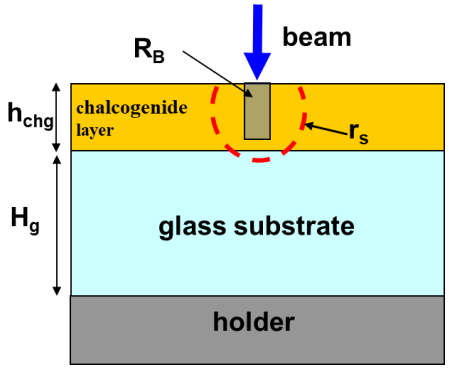

Fig. 3.17. *Setup for spot irradiation (ion or light) of a ChG layer. h_{chg} – thickness of chalcogenide layer (10 μm), H_g– thickness of the glass substrate (1 mm), R_B – penetration depth of the beam (ion or light), r_s – radius of quasi spherical heat field distribution, Holder– metal plate [80].*

This temperature rise outside of the 10 μm region for ion beam irradiation was 2.5 K and 5K for the light illumination. Therefore, this temperature rise is negligible even for low T_g glasses like Se.

It should be noted, that temperature rise in the irradiated region should be higher at a distance under 10 μm from the irradiation center, which is influenced by the beam parameters. In a focused spot, it could even reach T_g, which is highly likely to occur in Se, as shown in [82]. Temperature rise above T_g is disadvantageous [73], while under it is beneficial for the mass transport [67]. Hence, it can be said, that ion beam patterning has higher efficiency in selenium, than in $As_{20}Se_{80}$ or As_2S_3, if both ion beam and light induced mass transport have similar characteristics, as a result of the temperature increase (Fig. 3.16.).

Analyzing Fig. 3.16. we can see that patterning efficiency was higher with He^+ ions than with H^+ ions for the same chalcogenide compositions. It is necessary to say, that even when the energy was the same for both type of irradiations, differences could be found in beam penetration depth, linear energy transfer (deposited energy/ unit depth), current, focusing and beam spot form. Twofold increase in Se and approximately 30 times higher efficiency in As_2S_3 was achieved with He^+ ions compared to proton patterning.

Taking a closer look at Se and using SRIM simulations, the He^+ ion penetration depth was 7–8 μm and around five times deeper for protons. Linear energy transfer was up to 5–10 times larger for He^+ ions compared to protons in Se. Data for other compositions is also similar. Since He^+ ions "give out" their energy faster per unit depth, this may cause more significant changes in the materials. This is even more visible in lower viscosity As-Se compositions compared to As-(Ge)-S [110].

More challenging issues relating to the recording mechanism in the investigated glasses may be linked to the formation of pores and bubbles, especially at high temperatures. However, pore and bubble existence was eliminated by direct FIB and SEM measurements of the created surface pattern (see Fig. 3.18.). EDX cross section measurements in irradiated and unirradiated regions on $As_{20}Se_{80}$ did not show composition changes.

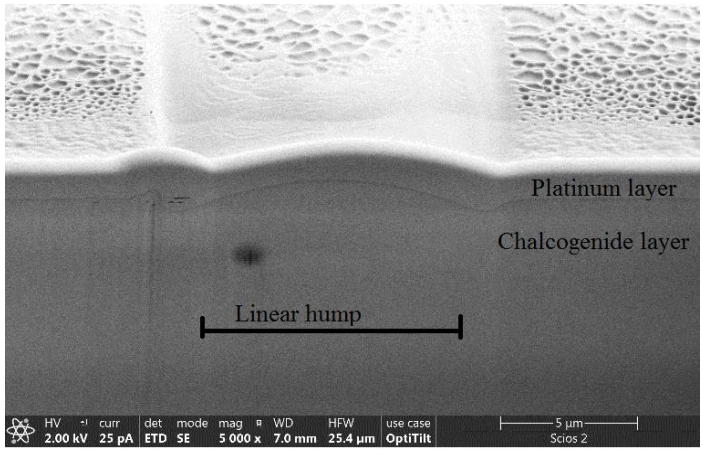

Fig. 3.18. *Cross-section of $As_{20}Se_{80}$ surface irradiated by 2 MeV He^+ ions (FIB/SEM image) [80].*

As a result of structural changes to a more organized state, small, up to 1% local expansion or contraction is still possible after ion beam irradiation, as is the case with light in other compositions [4], [111],[112]. In our case, this could have given only a few hundred nanometer surface relief, which is much less than what was detected.

During ion beam irradiation, charge accumulation in the bombarded spot can also effect its diffusion, and in the samples with dielectric substrates, patterning efficiency was higher compared to the ITO covered glass substrates.

To further investigate the substrate conductivity influence, I investigated Se and As_6Se_{94} layers under He^+ ion irradiation (Fig. 3.19.), deposited on glass and ITO covered substrates. Both height and volume were larger on the non-conductive substrate, compared to the ITO layer. The reason behind this process might be Coulomb force attraction-repulsion.

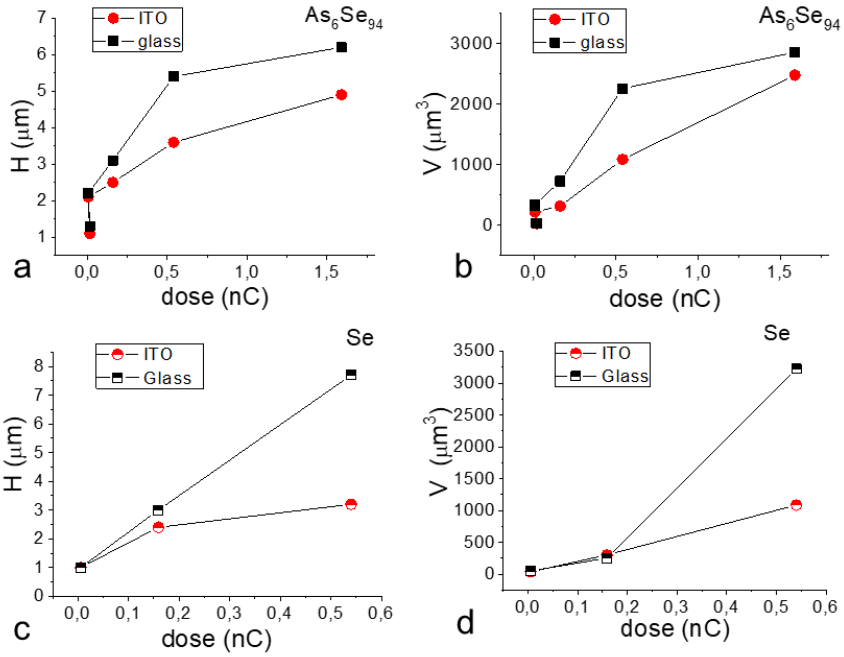

Fig. 3.19. *He^+ (2MeV) ion beam patterning efficiency (height and volume of spots on substrate conductivity (conductive or not conductive): a, b – As_6Se_{94} (25 μm thick); c, d – Se (26 μm thick) [80].*

Ions entering the ChG layer are accumulated around their stopping region. The created electric field has to be limited by the avalanche multiplication threshold, which is $7 \cdot 10^7$ V/m [113], [114] for Se.

Avalanche multiplication may be stimulated during ion irradiation in the chalcogenide glass. Since Se has a high resistivity ($\rho_{\text{selenium}} \approx 10^{14}$ Ω·m [115]), charge decrease is only possible through an avalanche effect which increases the relief formation process. Surface deformation is also possible, because of the built-in field stresses the glass structure. This is likely the case, since on ITO covered substrates patterning efficiency is lower (Fig. 3.19.), meaning the charges are grounded and there is less stress in the ChG layer.

Patterning efficiency comparison with optical illumination can be made, but light polarization and optical fields introduce additional difficulties. Comparing spot recording by 2 MeV He^+ ion beam (Fig. 3.16a) with e-beam recording from literature data [116] shows lower energy use to create a surface relief by ion beam by four times. Charge multiplication and larger penetration depth may be the reason behind that. However, it

should be noted that direct comparison cannot be made, because of the different nature of the irradiating beams (beam focusing, energy, current, penetration depth, scanning frequency, etc.).

Comparing different types of irradiations, namely light, electron and ion beam irradiation, we can see common characteristics, as a result of stimulated structural transformations and mass transport effects. In the first stage, there is electron-hole excitation, creation of charged defects. This is followed by charged particle or structural element diffusion in gradient fields of chemical potentials, electric fields and capillary effects [68]. However, there are differences: absence of light polarization compared to light, and the number of excited electron-hole pairs created are multiple orders higher when ion irradiation is used. Lastly, for thick layer applications, the use of ion beams may be beneficial, because of the larger penetration depth compared to light. The process can be used for direct recording and prototyping photonic elements on chalcogenide glasses.

Conclusions

On the selected chalcogenide glass compositions (Se, As_6Se_{94}, $As_{20}Se_{80}$, As_2S_3 and $As_{30}Ge_{20}S_{50}$) surface relief structures were recorded with 2 MeV energy H^+ and He^+ ion beams.

I fabricated the investigated bulk glasses by mold method and deposited the chalcogenide layers after simulating the required layer thicknesses using SRIM software. For the surface relief investigations I used an AFM and a profile meter.

I showed that the highest relief patterning efficiency was achieved on a-Se. Furthermore, patterns of spots and lines were recorded in the selected compositions with high efficiency, which shows the applicability of such a process and the equipment for in situ recording of optical elements and diffraction gratings.

I showed that substrate conductivity influences the pattern formation. Additionally, surface relief structure creation efficiency was higher with He^+ ion irradiation compared to protons.

Patterning processes have common elements: formation of charge and temperature gradients, mass transport stimulated by these gradient fields and glass network transformations. Comparing the illuminating sources, ion beam patterning seems to be the energetically most efficient.

Results of Chapter 3.3. are covered by thesis point 4.

These were published in:

[A5.] S. Molnar, R. Bohdan, G. Nagy, I. Rajta, L. Illes, A. Csik, S. Kokenyesi, *Direct surface patterning of amorphous chalcogenide layers with high- energy H+ and He+ ion beams*, J. Mater. Sci. Mater. Electron. **30**, 16, 15331–15338 (2019).

4. Optical Recording on Chalcogenide Polymer Nanocomposites

Considering the known and previously analyzed characteristics of amorphous chalcogenides as optical recording media (high refractive index, photodarkening-bleaching, temperature dependences), my goal was to overcome the challenging problem of combining these glasses with transparent photopolymers, and create a nanocomposite recording media with new functional parameters for possible use in flexible photonic structures and biocompatible environments.

First, I measured the optical transmission spectra of the polymerized *14m* pure monomer (without NPs) and the *14h* chalcogenide-polymer nanocomposite (prepared as described in Chapter 2) and compared to the vacuum-evaporated As_3S_3 chalcogenide thin film, as shown in Fig. 4.1. Before the measurement, excluding As_2S_3, the layers were polymerized by UV light.

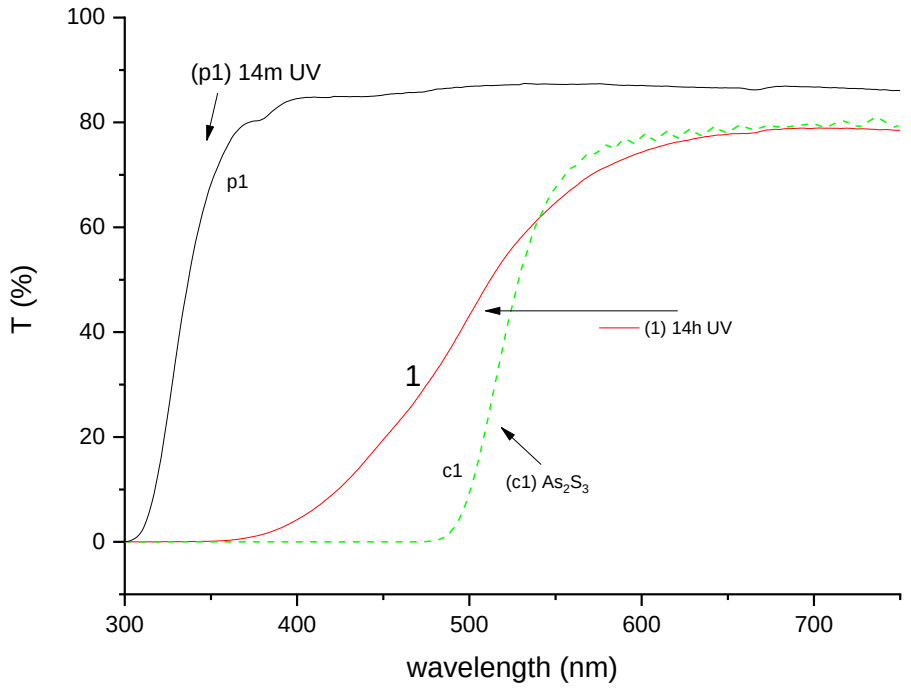

Fig. 4.1. *Transmission spectra of the 14h nanocomposite (curve 1), 14m UV (curve p1) monomer layer (30 μm thick), and As_2S_3 film (curve c1, 2.5 μm thick) [70].*

As shown in Fig. 4.1., originally, the pure polymer is optically transparent in the visible spectra, and As_2S_3 (or similarly other As-Se (S) chalcogenides) has a proper absorption edge in the visible spectral region. Adding a small amount of chalcogenide nanoparticles to the organic matrix (2.6 vol% or 7.5 wt% of monomer volume and weight, respectively) causes some shift of the resulting absorption edge towards shorter wavelengths in the nanocomposite in comparison with thick ChG glasses or layers. It may be partially caused by quantum confinement effects in nanoparticles and related small blue shift in their absorption spectra, but mostly due to the decreased absorption in the short wavelength range of absorption edge. Low light scattering and low total absorption caused by the low concentration and dimensions of the nanoparticles may also contribute to this effect.

Chalcogenide nanoparticle sizes in a polymer matrix were investigated by TEM measurements shown on Fig. 4.2. It should be noted, that sample preparation for TEM measurements may cause some degree of cluster formation.

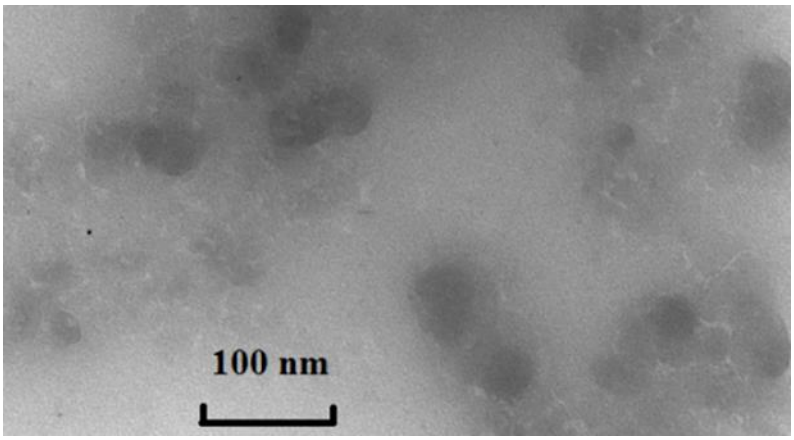

Fig. 4.2. *Nanocomposite TEM image [70].*

Initial components of the nanocomposite were both in amorphous state, and the resulting new nanocomposite stayed amorphous as well, according to XRD measurements. FTIR-ATR measurements show a possible capping effect of the nanoparticles by the monomers. Using the data, we can see the change in infrared absorption and possible bond changes. The results of these measurements are presented in Fig. 4.3. for the *14h* sample (with As_2S_3 nanoparticles). Nanocomposites from Table 2.1. show similar results as well.

Data from literature [117], [118]. [119], [120], [121], [122] are in agreement with the FTIR-ATR measurements obtained for composite *14* for phenyl fragment and urethane polymers.

As_2S_3 nanoparticle addition to the pure *14* monomer mixture (14h nanocomposite in Table 2.1.) causes the following FTIR-ATR spectral changes, which support nanoparticle stabilization by monomers (see Fig. 4.3.): 753 cm^{-1} and 690 cm^{-1} band energy decrease shows the presence of associated bonds of benzene ring and -N-H group; 950 cm^{-1}, 1038 cm^{-1} and 1160 cm^{-1} band energy decrease shows $\nu_{sym}C_{ph}$-C-O and νC-N, ν_{asym}C–O–C(=O) stretching vibration decrease; 850 cm^{-1} (νC–C–O–C(=O)–C(H_3)) band energy decrease shows nanoparticle stabilization by oxygen; 1237/1140 cm^{-1} band intensity ratio changes are connected to the ν_{asym}C–O–C(=O) vibrations.

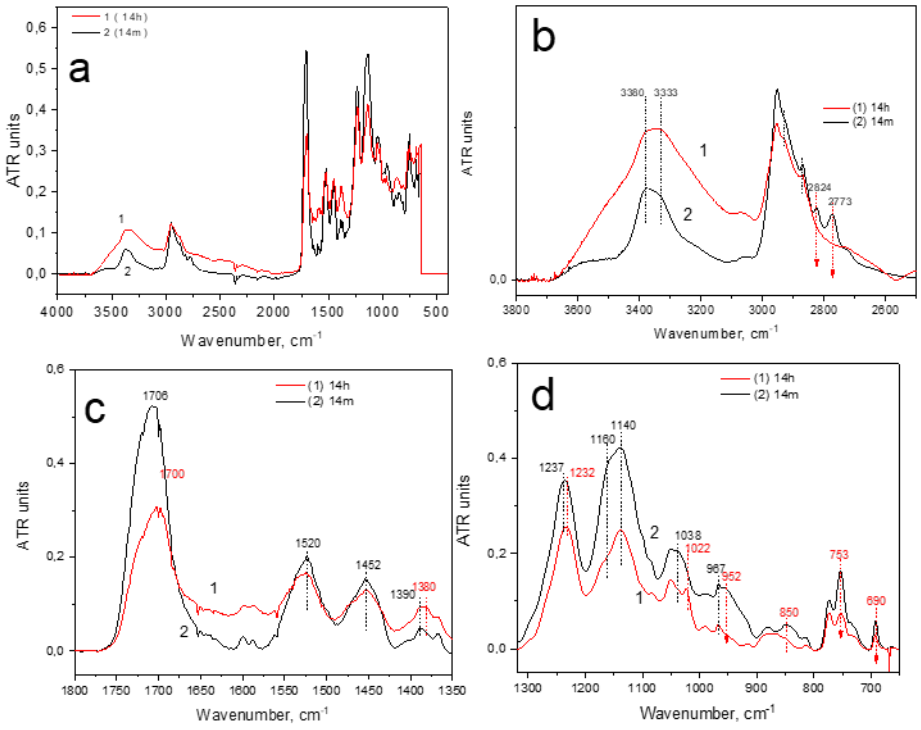

Fig. 4.3. *FTIR-ATR spectra for the 14h nanocomposite (curve 1) and pure monomer matrix (composition 14m) without chalcogenide nanoparticles (curve 2) in various spectral regions (a–d). (a–full range, b,c,d – selected ranges) [70].*

These changes indicate that donor-acceptor bonds are formed between the monomer matrix and the surface of the chalcogenide nanoparticles, which could prevent further aggregation, and help the homogeneous infusing to the monomer matrix and particle movement during optically induced mass transport.

Applicability of the developed chalcogenide nanocomposites for optical recording or as elements of photonics, strongly depends on the ability to change material properties upon illumination or heat treatment. Parameters of chalcogenides can easily be modified this way, as shown in [123], [124].

To test how it responds to light and heat effects, the *14h* nanocomposite was chosen on the base that green laser light can induce polymerization, and the As_2S_3 nanoparticles can be excited in that optical region as well.

To calculate the composite material's refractive index, I tested a few models on relative permittivity (Garnet Maxwell [125], Wiener [126], [127], Bruggeman [128], Lichtenecker [129]) first. Experimental data of [130] was analyzed by these methods, since the $As_{42}S_{58}$ in PMA composite is very similar to our composition, with $n_{polymer}$=1.45 and $n_{As42S58}$= 2.32 (at 633 nm) at various chalcogenide nanoparticle concentrations.

The models showed good correlation with experimental data. Nevertheless, the best results for low nanoparticle concentration were achieved by the Garnet Maxwell model [125], [131].

According to this model, the refractive index (*n)* without absorption of non-magnetic materials can be expressed as*:*

$$n(\omega) \approx \sqrt{\varepsilon(\omega)}, \tag{4.1}$$

where ω – light wave frequency, $n(\omega)$ – refractive index. Based on this relative permittivity of composite materials model [125], the refractive index of the nanocomposite can be expressed as:

$$n_{eff} = n_{polymer} \cdot \sqrt{\left\{ \frac{1+2\cdot f_{ChG}\cdot\left[(n_{ChG}^2 - n_{polymer}^2)/(n_{ChG}^2 + 2n_{polymer}^2)\right]}{1-f_{ChG}\cdot\left[(n_{ChG}^2 - n_{polymer}^2)/(n_{ChG}^2 + 2n_{polymer}^2)\right]} \right\}}, \tag{4.2}$$

where $n_{polymer}$ – polymer matrix refractive index, n_{ChG} – chalcogenide refractive index, n_{eff} – nanocomposite refractive index, f_{polymer} – polymer volume content, f_{ChG} – chalcogenide nanoparticle volume content.

On the other hand, the level rule approximation gives good correlation with our results as well:

$$n_{eff} = n_{polymer} \cdot f_{polymer} + n_{ChG} \cdot f_{ChG} \quad (4.3)$$

As shown on Fig. 4.4., the refractive index dependences (at 635 nm) on nanoparticle volume content were calculated by Eq. (4.2) and (4.3) using the developed *14h* NC.

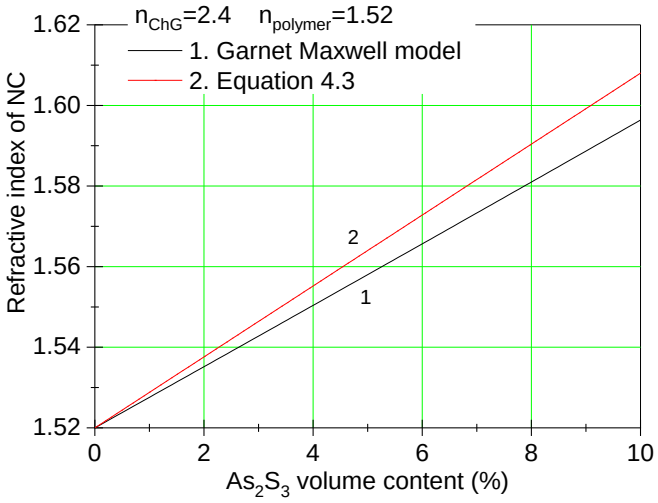

Fig. 4.4. *14h nanocomposite refractive index dependence on As_2S_3 nanoparticle volume content (1 – Garnet Maxwell model, 2 – Equation 4.3.) [70].*

From Table 2.1., the volume content of chalcogenide nanoparticles is approximately 2.6% in the *14h* nanocomposite, which will give a refractive index close to 1.54 (Fig. 4.4. curve 1). Using the second model with Eq. (4.3), and with 1.52 and 2.4 refractive indices for the polymer and chalcogenide glass respectively, the resulting refractive index for the nanocomposite is 1.54. This is in agreement with literature data from [130].

Due to the chalcogenides' properties of light and thermal sensitivity, the developed higher refractive index nanocomposite can be used for optical recording purposes, where we can modulate these properties after the recording process.

To investigate these properties, I conducted transmission measurements on the *14h* nanocomposite and its components (As_2S_3 thin film and monomers). The measurements were done for initial conditions as well as after heat treatment and after light illumination (shown in Fig. 4.5.).

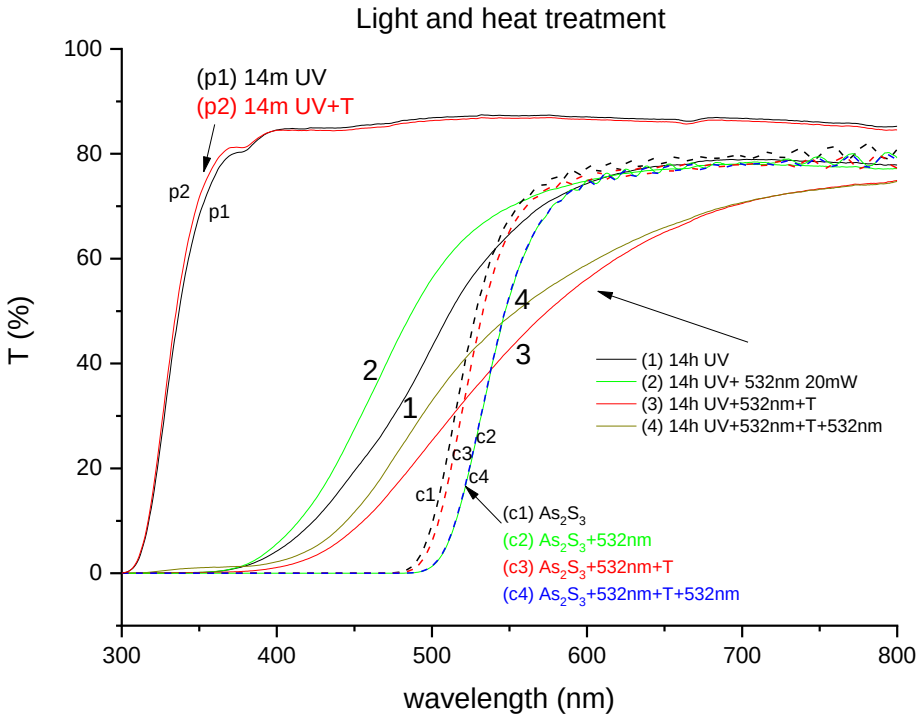

Fig. 4.5. *Transmission spectra for pure monomer 14m (curve p1–p2), As_2S_3 layer (curve c1–c4) and As_2S_3 chalcogenide nanocomposite 14h (curve 1–4). Before and after heat treatment and illumination (T – heat treatment, UV and 532nm – illumination) [70].*

Just from Fig. 4.5, we can see that the pure polymer (14m, curve p1-p2) is not affected by heat treatment, as well as it is transparent in the visible spectra. Also, as expected, the transmission of the *14h* nanocomposite lies between the pure *14m* polymer and the As_2S_3 layer. However, it is also visible that the effect of light and heat on the ChG nanocomposite is opposite to the pure As_2S_3 layer. In this case, the chalcogenide layer experiences photodarkening (curve c1-c2) under light illumination, but at the same time, the nanocomposite experiences photobleaching (curve 1-2). The result of the heat treatment of the nanocomposite is also opposite to the chalcogenide layer. At the first heat treatment, in the nanocomposite photodarkening occurs (curve 2-3), but photobleaching in the chalcogenide layer (curve c2-c3).

From the transmission spectra in Fig. 4.5., I created $(\alpha hv)^m$ vs hv dependences and normalized them (see Fig. 4.6.), since these dependences offer more information compared just to the transmission measurements.

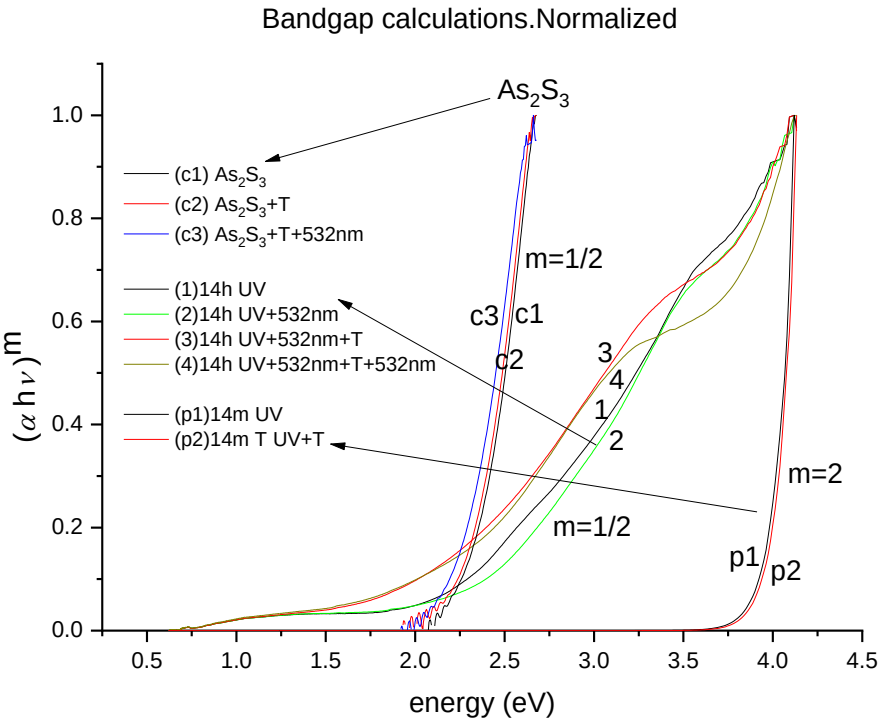

Fig. 4.6. *Normalized $(\alpha h\nu)^m$ vs hν dependences on illumination and heat for the 14h nanocomposite and its components (monomer 14m (curve p1–p2), As_2S_3 (curve c1–c4)), and As_2S_3 ChG nanocomposite 14h (curve 1–4) dependence. Here: m=2 for direct band gap, m=1/2 for indirect band gap materials (T – heat treatment, UV and 532nm-illumination) [70].*

Band gap calculations were performed taking m=2 for direct band gap materials, and for indirect band gap material (such as chalcogenides [106], [132]) m=1/2 was taken (see Table 4.1.).

Analyzing Fig. 4.6. (see Table 4.1 for band gap data), the calculated band gap for *14h* NC is 2.08–2.25 eV, which is slightly lower than for the As_2S_3 layer (2.27–2.35 eV). Structure, deformations, charging of the As_2S_3 particles could be reason behind that.

№	Material	Influence *(T – heat treatment, UV and 532nm – illumination)*	Band gap (eV)	Process(es)
p1	14m	UV	3.96	Polymerization, contraction of the monomer (polymer)
p2	14m	UV+T(150°C, 1h)	3.98	Bleaching determined by contraction of the polymer
c1	As_2S_3	as deposited	2.35	
c2	As_2S_3	as deposited+532nm (85mW, 100min)	2.27	Darkening determined by photo-structural transformations: defect generation
c3	As_2S_3	as deposited+532nm (85mW, 100min)+T(150°C, 1h)	2.33	Bleaching due to the annealing, defect relaxation
c4	As_2S_3	as deposited+532nm (85mW, 100min)+T(150°C, 1h)+ 532nm (85mW, 5min)	2.27	Darkening determined by illumination, defect generation
1	14h	UV	2.2	Polymerization and contraction of the polymer. Stress generation in As_2S_3 is possible
2	14h	UV+532nm (30min, 20mW)	2.25	Photo-induced softening of ChG NPs, stress decreasing in nanoparticles is possible
3	14h	UV+532nm(30min, 20mW)+T(150°C, 1.5 h)	2.08	Heating and cooling process generates two processes in polymer:

				expansion and contraction
4	14h	UV+532nm (30min, 20mW)+T (150°C, 1.5 h)+ 532nm (30min, 20mW)	2.08	The light cannot decrease the stress in the contracted polymer

Table 4.1. *Analyzation of illumination and thermal processes for Fig. 4.5. and Fig. 4.6. [70].*

Again, we can see from the results (Fig. 4.5.– 4.6., Table 4.1.), that the nanocomposite behavior is different from the behavior of the initial materials. Upon light illumination, As_2S_3 experiences photodarkening, but the polymerized virgin polymer (*14m*) sample does not react to light. The band gap of the latter only changes from 3.96 to 3.98 eV after heat treatment, which may be the result of structural reordering, volume contraction, or evaporation of the remaining solvents from the matrix.

In the As_2S_3 layer, the light induced photodarkening can be erased by heat treatment, which increases the band gap from 2.27 to 2.33 eV (Table 4.1., curve c2-c3). As-deposited metastable chalcogenides after heat treatment go back to a slightly different, but more stable state. Additional illumination on the chalcogenide layer by 532 nm band gap light causes photodarkening, and results in 2.27 eV band gap (Table 4.1.,curve c3-c4).

Heat treatment on the *14h* NC (423K, close to T_g of As_2S_3, safe for the polymer) showed an opposite trend to the As_2S_3 layer. Photodarkening occurs, and the band gap decreases from 2.25 eV to 2.08 eV (Table 4.1., curve 2-3). With additional illumination, bleaching can be induced in the NC depending on the dose, but it cannot reach the initial fresh polymerized state (Fig. 4.5., curve 3-4). Bleaching effects in chalcogenides are usually indicators of the non-equilibrium state [123], [124].

The dissimilar effect in the NC compared to its components may be explained by known changes of refractive index, and transmission of amorphous chalcogenides [123], [124]. Additionally, illumination and temperature caused changes can occur, like structural changes of the polymer matrix, viscosity and stresses as well. Optical elements like waveguides, gratings and photonic crystals can be created and adjusted by the investigated stimulations. With higher concentration of ChGs in the polymer matrix, these effects should be even more pronounced.

To demonstrate the applicability of the developed nanocomposites as optical elements, I recorded and investigated holographic gratings on them

(see Fig. 4.7. and Table 4.2.). Without the nanoparticles no grating recording was possible in the given pure polymer.

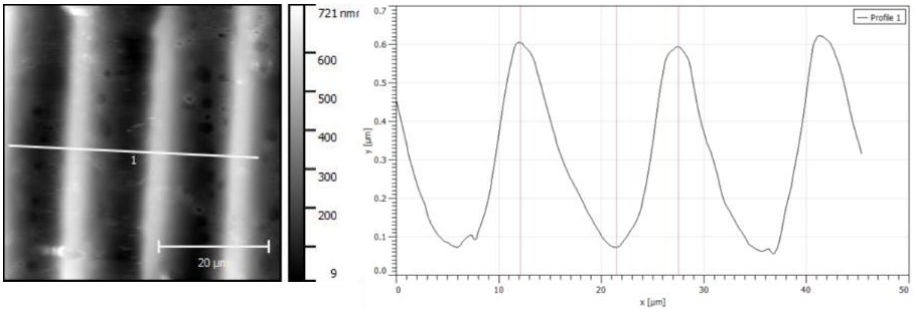

Fig. 4.7. *AFM picture of a thick volume grating recorded in 14h nanocomposite (a) and its surface profile (b) [70].*

Polymer-chalcogenide nanocomposite	11h	14h	20h
Diffraction efficiency, %	6	20	47

Table 4.2. *Diffraction efficiency of recorded volume gratings in different nanocomposites [70].*

Surface reliefs created on the *14h* nanocomposite had a sinusoidal relief with a smooth surface, both for 2 μm and 15 μm (see Fig. 4.7.) period holographic gratings. Depth modulation was around 520–530 nm for the latter.

Highest diffraction efficiency was achieved in the *20h* nanocomposite, followed by the *14h* and *11h* nanocomposite (see Table 2.1 and Table 4.2.). Differences between the diffraction efficiencies of the nanocomposites could be explained by the different diffusion properties of the nanoparticles, viscosity of the used polymer matrix, nanoparticle size, etc.

Comparing the input of the surface modulation and of the chalcogenide nanoparticle reorganization to the diffraction efficiency (DE) for the *14h* NC, it seems that the 20% DE in transmission mode is coming from Δn reorganization between dark and illuminated regions of the thick hologram (Table 4.2).

To calculate Δn modulation in the *14h* thick hologram, first I performed reflection measurements with an 532 nm laser light on the

smooth surface of the *14h* NC, which showed a 0.006 increase in the refractive index. Since the relative and absolute changes of the refractive index should be similar for both 532 nm and 635 nm light, using data from (Table 4.2) for the 2 μm period *14h* NC and Kogelnik's formula [133], Eq. (4.4), I calculated the refractive index modulation Δn in the volume grating.

$$\Delta n = \frac{\lambda \cos \theta_B \arcsin \sqrt{\xi}}{\pi H} \tag{4.4}$$

Here θ_B – the Bragg angle for the recorded volume grating (9.1° at λ= 635nm), H– layer thickness (30 μm), ξ – diffraction efficiency. This results a maximum refractive index deviation of Δn=0.003, which is smaller than the green light caused refractive index change of 0.006.

This total of 0.003 refractive index change could be explained by the result of two processes. The first process is the diffusion of the chalcogenide nanoparticles between the illuminated and unilluminated periodic regions of the grating, and the second is the light induced refractive index change of the chalcogenide nanoparticles.

In the first process, the polymerization in the illuminated region (peak) pushes some of the chalcogenide nanoparticles into the unilluminated region (valley), so the NP concentration drops in the illuminated region, and the chalcogenide nanoparticles are collected in the unilluminated regions. This is in accordance with previously investigated nanocomposites, where the silica nanoparticles have been found in the unilluminated regions [134]. This nanoparticle diffusion can cause a difference in the refractive index between the peaks and valleys.

In the second process, light causes a refractive index change in the nanoparticles. Ideally in the illuminated regions, the interference is perfect, meaning the illuminated region gets all the light and the unilluminated region gets none. In reality, the spatial distribution of the intensity of the two Gaussian beams during holographic recording may not be ideally set up, and the light caused refractive index modulation will not reach its maximum possible value. Therefore, the region of minimum light intensity is not a dark zone. Meaning, an imperfect light interference distribution could cause a lower refractive index modulation of the chalcogenide nanoparticles. In addition, this change of the refractive index of the nanoparticles can change during readout. At the same time, the diffusion related component of the refractive index modulation in the grating cannot relax in the polymerized nanocomposite. Therefore, the refractive index modulation in the chalcogenide nanocomposites at holographic recording is globally determined by the diffusion of chalcogenide nanoparticles. The

refractive index change caused by light illumination may have a smaller, opposite role compared to the diffusion of the nanoparticles in the resulting diffraction efficiency in the volume grating.

Such double, superimposed variations of optical transmission and refractive index in a comparatively soft, flexible recording media during the *in situ* recording process, or in the working photonic elements like coupling gratings, waveguide sensor elements with additionally functionalized surfaces on flexible substrates, are promising applications of the above described materials.

Conclusion

I showed that using a chemical manufacturing method, transparent, stable chalcogenide-polymer nanocomposites with an increased, variable refractive index can be created. Based on this method, optical elements, such as diffraction gratings and waveguides can be created. Such produced nanocomposites are created by careful combination of different monomers and chalcogenide glasses, without noticeable aggregation or scattering effects.

I recorded holographic gratings in the chalcogenide nanocomposite layers, fabricated samples for optical measurements and performed transmission measurements on them at different illumination and heating conditions. This enabled me to calculate and compare the band gap changes compared to the pure monomer or chalcogenide layer at different conditions.

I showed that low (3 vol%) content of chalcogenide glass can produce noticeable refractive index change of the nanocomposite, applicable for surface hologram or volume grating with up to 40% of diffraction efficiency.

The refractive index modulation is caused by nanoparticle and monomer diffusion into periodical structures, and by light-induced changes in the chalcogenide nanoparticles.

Properties of the developed nanocomposites can be changed even after the polymerization process with light irradiation or heat treatment.

Results of Chapter 4 are covered by thesis point 5.

These were published in:

[A6.] J. Burunkova, S. Molnar, V. Sitnikova, D. Shaimadiyeva, G. Alkhalil, R. Bohdan, J. Bako, F. Kolotaev, A. Bonyar, S. Kokenyesi,

Polymer–chalcogenide glass nanocomposites for amplitude–phase modulated optical relief recording, J. Mater. Sci. Mater. Electron. **30**, 10, 9742–9750 (2019).

Summary

In my thesis, I investigated the stimulated changes occurring in selected amorphous chalcogenide layers and nanocomposites.

1. I showed and analyzed the surface relief creating effect of focused He-Ne laser beams on bulk amorphous selenium samples at different light intensities, which includes thermally induced mass transport processes.

I fabricated the bulk samples by using polishing and molding methods and investigated the recorded surface profiles on them by using a profile meter.

I created a thermal model for the region near the vicinity of the illuminated spot, and micro-Raman measurements were done to study the structural changes depending on the distance from the illuminated spot, i.e. the temperature distribution under irradiation. This allowed the separation of thermal effects from light induced ones, which happen during the surface profile formation.

Accordingly, material properties such as heat conductivity, softening temperature should be considered in recording experiments to eliminate possible negative processes like crystallization and self-erasing. The crystallization effect can be even used as a temperature marker for low T_g chalcogenide glasses of proper compositions [A1, B4, C1, D1, D2, D4, E2, E3].

2. It was shown and published for the first time, that the thermal erasing process of holographic relief gratings can be used for direct measurement of the viscosity of thin chalcogenide films.

In this experiment I deposited the chalcogenide layers, using TVE method, recorded surface holograms and investigated them with AFM. Furthermore, I designed and built the experimental setup for the erasing measurements, performed the diffraction efficiency measurements and calculated the viscosity and diffusion parameters.

Additionally, I showed that the thermal erasing of a holographic grating on an $As_{20}Se_{80}$ thin film can be described by Arrhenius law with 2.9 eV activation energy, and this process has a viscous flow character. My investigations showed, that the erasing process can be accelerated with band gap light, and at the experiments, it was characterized by an activation energy between 2.9–1.1 eV for the 3.5 μm grating, depending on light intensity. I showed that erasing by light also depends on the grating period,

light intensity and polarization. In this case, band gap light illumination accelerates the grating erasing.

I showed, that gratings with large, 15 μm periods have viscous flow erasing mechanics, where the activation energy of erasing is independent of light illumination, and the flattening coefficient is proportional to the grating period as Λ^{-1}, however, gratings with smaller, 3.5 μm period, have a flattening coefficient proportional to Λ^{-3}. The latter gratings' effective viscosity is decreased by photo-induced diffusion, and the effective diffusion coefficients are larger using *p*- and depolarized light, compared to *s*-polarized light, and are equal at high, close to T_g, temperatures. The contribution of photo-induced diffusion to the erasing process drops at higher temperatures, whereas viscous flow contribution increases. By separation of these processes in mass transport, I determined the photo-induced diffusion coefficients and their temperature dependences, and showed that band gap light only changes the chalcogenide film's effective viscosity [A2, A3, D3, E2, E3].

3. I developed two new experimental methods for investigating light stimulated mass transport in As-Se (S) chalcogenide thin films.

For these investigations, I developed the deposition setup and deposited the thin chalcogenide films by TVE method. I recorded the surface reliefs on the thin layers and investigated the created profiles by AFM.

These experimental methods show *in situ* that light induced mass transport direction depends on the material composition and recording light polarization.

I showed that depending on the composition in the As_xSe_{100-x} (x=1,3,6,20,40) system, optically induced mass transport can be eliminated at around 1 at% of As, which may be connected to the electric parameters of charge carriers in the composition. This method of "two adjacent chalcogenide layers" also showed that during *in situ* recording investigations of the most used As-Se chalcogenide materials, where As is above 1 at%, the mass transport direction is opposite compared to the direction in amorphous selenium. Mass transport direction in As_2S_3 was found to be opposite to Se as well.

The second developed method ("mesh mask") shows directly, how mass transport direction depends on the illuminating light polarization during surface relief formations. Based on this, the type of material and possible recording output can be identified based on its mass transport properties.

Both methods can be used for simplifying more complicated or large experimental setups, and are improved in comparison to previously existing ones [A4, D3, D4, D8, E1, E2, E3].

4. On selected chalcogenide glass compositions (Se, As_6Se_{94}, $As_{20}Se_{80}$, As_2S_3 and $As_{30}Ge_{20}S_{50}$), I recorded surface relief structures with 2 MeV energy H^+ and He^+ ion beams.

I fabricated the investigated bulk glasses by mold method and deposited the used chalcogenide layers after simulating the required layer thicknesses using SRIM software. For the surface relief investigations I used an AFM and a profile meter.

I showed that the highest relief patterning efficiency was achieved on a-Se, similarly to results obtained by optical recording. Patterns of spots and lines were recorded in the selected compositions with high efficiency, which shows applicability to create structures like lens matrices and diffractive elements in a one-step process by ion irradiation.

I showed that patterning by a 2 MeV He^+ ion beam on Se and As_6Se_{94} chalcogenide layers on a non-conductive substrate is more efficient compared to a conductive substrate, which shows that charge accumulation and proper distribution support pattern growth.

Material properties like rigidity, T_g, heat and electrical conductivity could be the reason behind the various patterning efficiencies between the investigated glasses. As mentioned, highest patterning efficiency was achieved on Se samples, lower efficiency on As-Se samples and lowest efficiency on As-S-(Ge) samples. This can be explained by As-Se compositions having more flexible structures compared to As-S-(Ge) structures, as well as higher bonding energies for the latter compositions.

Ion beam caused local temperature rise should also be considered as a patterning effect, since the lowered viscosity helps mass transport processes. This may be more prevalent in low softening materials. Overheating, on the other hand, could result in local temperatures above T_g, and in the erasing of the recorded surface pattern.

I showed that patterning in the selected chalcogenide samples with the same 2 MeV energy ion irradiation was more effective with He^+ ions compared to proton irradiation. In numbers, it is ranging from 2 times in the case of Se to about 30 times in the case of As_2S_3. This may be the result of around 5–10 times less ion penetration depth, and around ten times larger linear energy transfer for 2 MeV He^+ ions, compared to the same energy H^+ ions for a selenium sample. Similar results were obtained for the other investigated compositions as well. Accordingly, larger absorbed energy per unit depth may cause increased patterning efficiency as well.

Patterning processes at different irradiations have common elements: formation of charge and temperature gradients, mass transport created by these gradient fields, local disorder and structural transformations. Comparing to the other illuminating sources (electron or light), ion beam patterning seems to be energetically the most efficient [A5, C1, D2, D4, D6, D10, E2, E3].

5. I showed that positive characteristics of transparent low refractive index photopolymers and light-sensitive high refractive index $As_{20}Se_{80}$ and As_2S_3 chalcogenide glasses can be combined in a nanocomposite. Surface and volume holographic gratings were recorded in such media.

I recorded holographic gratings in the chalcogenide nanocomposite layers, fabricated samples for optical measurements and performed transmission measurements on them at different illumination and heating conditions. This enabled me to calculate and compare the band gap changes compared to the pure monomer or chalcogenide layer at different conditions. The grating recording shows the applicability of the nanocomposite for optical elements, since without the nanoparticles no relief structures were possible to be recorded in the investigated polymers.

I showed that just 2.6 vol% addition of As_2S_3 nanoparticles to the polymer matrix resulted an increased refractive index of 1.54 in the nanocomposite, whereas in the pure polymer it is 1.52. I showed that the refractive index modulation, recorded in the same *14h* As_2S_3 nanocomposite, in the volume hologram is 0.003. For an As_2S_3-polymer nanocomposite, 20% diffraction efficiency is achievable in volume grating and 47% for an $As_{20}Se_{80}$-polymer nanocomposite. The different diffraction efficiency between the nanocomposites may be the result of the different nanoparticle diffusion properties, particle sizes, monomer properties, etc. The refractive index change in the volume grating is caused by nanoparticle and monomer diffusion into periodical structures, and by light-induced changes of chalcogenide nanoparticle properties.

Additional functionality is added by light and temperature induced changes of the developed chalcogenide nanocomposites, even after the polymerization process [A6, C3, D5, D7, D9, D12, E2, E3].

Összegzés

Doktori dolgozatomban kiválasztott amorf kalkogenid rétegekben és nanokompozitokban előforduló stimulált változásokat vizsgáltam.

1. Kimutattam és elemeztem a fókuszált He-Ne lézernyaláb felületi reliefet létrehozó hatását amorf tömbi szelénium mintákon különböző fényintenzitások mellett, mely során a felületi struktúrák kialakulásában hőindukált anyagtranszport folyamatok jönnek létre.

A vizsgálatokhoz elkészítettem a tömbi üvegeket polírozás vagy hő általi formázás módszerekkel. A fény által létrehozott felületi struktúrákat profilométerrel vizsgáltam.

Ennek megfelelően kialakítottam egy hőmérsékleti modellt a besugárzott pont környezetére vonatkozóan, valamint mikro-Raman vizsgálatokat végeztünk, hogy a besugárzott pontból kiinduló távolság függő strukturális változások vizsgálata lehetővé váljon. Ez által a felületi struktúrák keletkezése során előforduló hő- és fényindukált jelenségek elkülöníthetővé váltak.

Ez alapján az olyan anyagtulajdonságok, mint a hővezetés és a lágyulási hőmérséklet figyelembe vétele hasznos lehet felületi struktúrák kialakítása során, hogy megelőzzük az olyan lehetséges negatív folyamatokat, mint a kristályosodás és a struktúra öntörlése. Viszont maga a kristályosodási effektus is felhasználható hőmérséklet-jelzőként megfelelő összetételű, alacsony T_g hőmérséklettel rendelkező kalkogenid kompozíciókban [A1, B4, C1, D1, D2, D4, E2, E3].

2. Az irodalomban először mutattam ki, hogy a holografikus rácsok termikus törlése használható direkt módszerként az amorf kalkogenid rétegek viszkozitásának meghatározására.

A kísérletben felhasznált rétegeket termikus rétegleválasztási módszerrel hoztam létre. Ezekre a rétégekre holografikus rácsokat írtam és AFM-mel vizsgáltam a struktúrákat. Továbbá megterveztem és megépítettem a törlési kísérlethez szükséges berendezést, végrehajtottam a diffrakciós hatásfok méréseket és kiszámítottam a viszkozitási és diffúziós értékeket.

Kimutattam, hogy $As_{20}Se_{80}$ vékonyréteg felületén lévő holografikus rácsok hőmérsékleti törlése Arrhenius törvény szerint megy végbe, melynek aktivációs energiája 2.9 eV. E törlési folyamat viszkózus folyás

által megy végbe. Kimutattam, hogy ez a törlési folyamat gyorsítható tiltott sáv közeli energiával rendelkező fénykvantumok által, és a folyamat aktivációs energiája 2.9–1.1 eV között változott a fény intenzitásától függően a 3.5 μm periódusú rács esetén. A felületi rács hőmérséklet általi törlése emellett függött mind a rács periódusától, mind a megvilágító fény polarizációjától.

A nagy, Λ= 15 μm periódusú rácsok törlése viszkózus folyás alapján megy végbe, melynek lapulási együtthatója a periódus Λ^{-1} függvénye, viszont a 3.5 μm periódusú rácsok törlése során ez az együttható Λ^{-3}. A 15 μm periódusú rács törlésének aktivációs energiája független a fény intenzitásától. A kis, 3.5 μm periódusú rács törlése során az effektív viszkozitás csökkenthető a fotoindukált diffúzió által, ami jelentősebb a *p*-polarizált valamint depolarizált fény hatására, mint *s*-polarizált fény esetén, és egyenlő a magas, T_g közeli hőmérsékleteken. A fotoindukált diffúzió hozzájárulása a hőmérsékleti törléshez csökken a magas hőmérsékleteken, miközben a viszkózus folyás hozzájárulása nő. E két mechanizmus elválasztásával a vizsgált anyagtranszport folyamata során, meghatároztam a fotoindukált diffúziós együtthatókat és azok hőmérsékletfüggését. Kimutattam, hogy a tiltott sáv energia közeli fény csak a kalkogenid rétegek effektív viszkozitását változtatja meg [A2, A3, D3, E2, E3].

3. Két új kísérleti módszert fejlesztettem ki a fotostimulált anyagtranszport hatásfokának és irányának meghatározására amorf kalkogenid üvegekben a felületi relief kialakulásának folyamata során.

A mérésekhez szükséges rétegeket termikus rétegleválasztási módszerrel hoztam létre. Emellett egy maszkolási módszert fejlesztettem ki a vékonyrétegek precíz egymás mellé illesztésének elérésére. A vékonyrétegekre felületi struktúrákat rögzítettem, melyeket AFM-mel vizsgáltam.

A két új módszer alkalmazásával *in situ* kimutattam, hogy az anyagtranszport iránya függ mind az író lézernyaláb polarizációjától, mind az anyag összetételétől.

A „szomszédos rétegek” módszer segítségével *in situ* kimutattam, hogy a fotoindukált anyagtranszport megszűnik az As_xSe_{100-x} összetételű kompozíciókban 1 at% As koncentráció esetén. Ez a jelenség a kompozíciókban lévő elektron és lyuk töltéshordozók eltérő jellemzőihez kapcsolódhat.

Továbbá a „szomszédos rétegek” módszer *in situ* kimutatta, hogy a legelterjedtebb As-Se kalkogenid üvegek esetén az anyagtranszport iránya ellentétes az amorf szelénhez viszonyítva, ha az As koncentráció meghaladja az 1 at% -ot. Az anyagtranszport iránya szintén ellentétesnek bizonyult As_2S_3 esetén a szelénhez képest.

A kifejlesztett „fémháló” módszerrel *in situ* kimutattam, hogy az anyagtranszport iránya és hatásfoka függ az író fény lineáris polarizációjától a különböző kompozíciókban létrehozott felületi struktúrák kialakulása során.

Mindkét módszer továbbfejleszti és egyszerűsíti a korábban már meglévő módszereket a fotostimulált anyagtranszport tulajdonságainak meghatározására amorf kalkogenidekben [A4, D3, D4, D8, E1, E2, E3].

4. Kimutattam, hogy 2 MeV energiájú, H^+ és He^+ ionok felhasználhatóak felületi reliefek kialakítására Se, As_6Se_{94}, $As_{20}Se_{80}$, As_2S_3 és $As_{30}Ge_{20}S_{50}$ kalkogenid üvegeken és amorf vékonyrétegeken, melyek a látható, NIR és IR spektrum tartományokban működő diffrakciós elemek, lencsemátrixok készítésére alkalmasak. Ezek a pont- és vonalstruktúrák egylépcsős módszerrel lettek kialakítva.

A vizsgált tömbi mintákat termikusan kezeltem a megfelelő felületi tulajdonságok elérése érdekében, a vékonyrétegeket pedig termikus rétegleválasztással hoztam létre. A termikus rétegleválasztás esetén a szükséges rétegvastagságot SRIM szoftver segítségével határoztam meg. A létrehozott felületi struktúrákat AFM és profilométer segítségével vizsgáltam.

Kimutattam, hogy a legnagyobb hatékonysággal amorf szelénben hozhatók létre felületi pont- és vonalstruktúrák nagy energiájú ionok hatására, mely anyagnak a legalacsonyabb a lágyulási hőmérséklete, és az egyik legjobban alkalmazható anyag optikai írásra is a vizsgált minták között.

Kimutattam, hogy Se és As_6Se_{94} rétegen történő felületi mintázat létrehozása 2 MeV energiájú He^+ ionokkal nagyobb hatásfokkal történik szigetelő hordozón, mint vezető hordozón, ami azt mutatja, hogy a töltés-felhalmozódás segíti a relief-képződést.

Az olyan anyagjellemzők, mint a merevség, T_g, hő- és elektromos vezetés befolyással lehetnek a létrehozott mintázatok hatásfokára a vizsgált anyagokban. Mint ahogy említve volt, a legnagyobb hatásfokkal Se mintákon volt lehetséges felületi struktúrákat kialakítani, ezt követték az

As-Se és végül az As-S-(Ge) kompozíciók. Ez talán azzal magyarázható, hogy az As-Se rendszer rugalmasabb struktúrával rendelkezik az As-S-(Ge) kompozíciókhoz képest, emellett az utóbbi anyagban nagyobbak a kötésenergiák is.

Az ionnyaláb okozta lokális hőmérséklet emelkedés szintén figyelembe veendő, mint mintázat kialakító effektus, mivel a csökkentett viszkozitás segíti az anyagtranszportot. Ez a jelenség erőteljesebb lehet alacsonyabb hőmérsékleten lágyuló anyagoknál. A minta túlmelegítése viszont a lokális hőmérséklet T_g fölé emelésével és a felületi struktúra törlésével járhat.

A 2 MeV energiával történő ion besugárzás során a He^+ ionokkal nagyobb hatásfokkal sikerült felületi struktúrákat kialakítanom a H^+ ion besugárzáshoz képest a vizsgált kalkogenid mintákban. Számokban kifejezve a Se esetén kétszeres, míg az As_2S_3 esetén harmincszoros különbségről van szó. Ennek oka a körülbelül 5–10-szer rövidebb ion-behatolási mélység és körülbelül tízszer nagyobb lineáris energiatranszfer lehet a 2 MeV energiájú He^+ ionok javára ugyanilyen energiájú H^+ ionokhoz képest Se mintában. Hasonló eredményeket kaptam a többi vizsgált mintában is. Tehát az egységnyi anyagmélységben elnyelt nagyobb energia növelheti a felületi struktúra kialakításának hatásfokát.

A felületi mintázatok kialakítása során a besugárzás típusától függetlenül azonos folyamatok jelennek meg: töltés- és hőgradiensek, az anyagtranszport ezen gradiens terekben, lokális rendezetlenség és strukturális átalakulás. A fent említett okok miatt az ionnyalábos relief-létrehozás energetikailag kedvezőbbnek tűnik a fény- vagy elektronnyaláb által létrehozott struktúráknál [A5, C1, D2, D4, D6, D10, E2, E3].

5. Kimutattam, hogy olyan nanokompozitok hozhatók létre, mely során az átlátszó, de alacsony törésmutatójú fotopolimerek pozitív jellemzői egyesíthetők a fényérzékeny és magas törésmutatójú $As_{20}Se_{80}$, As_2S_3 kalkogenid üvegek által adott lehetőségekkel. Ezekben a nanokompozitokban felületi és térfogati holografikus rácsokat hoztam létre.

A vizsgálatok során létrehoztam optikai célra készített nanokompozit mintákat, melyekre holografikus rácsokat írtam, és melyekkel áteresztőképesség-vizsgálatokat végeztem különböző megvilágításokon és hőmérsékleteken. Ez által meghatároztam és összehasonlítottam a tiltott sáv értékét a nanokompozitban és annak alkotórészeiben. A holografikus

rácsok sikeres létrehozása bizonyítja a nanokompozit optikai elemként való alkalmazását, mivel nanorészecskék nélkül nem volt lehetséges reliefeket kialakítani az adott polimerben.

Kimutattam, hogy egy mindössze 2.6 vol% értékű As_2S_3 nanorészecske-koncentráció a polimer mátrixban 1.54 értékű törésmutatót eredményez a nanokompozitban a polimer kezdeti, nanorészecske nélküli 1.52-höz képest. Emellett 0.003 értékű törésmutató moduláció érhető el As_2S_3 polimer-kalkogenid nanokompozitokban egy térfogati holografikus rácsban. As_2S_3 polimer-kalkogenid nanokompozitokban 20%, $As_{20}Se_{80}$ polimer-kalkogenid nanokompozitokban pedig 47%-os diffrakciós hatásfokú térfogati rács kialakítása volt elérhető.

A törésmutató-változás oka a rácsformálódás során a kalkogenid nanorészecskék és monomerek diffúziója, melyek periodikus törésmutató-eloszlást és fázismodulációt hoznak létre, további ok a kalkogenid nanorészecskék paramétereinek fény általi változtathatósága.

Az így létrehozott kalkogenid nanokompozitok és a belőlük készített elemek optikai tulajdonságai megváltoztathatóak fénybesugárzással vagy hőhatással, akár a polimerizációs folyamat után is [A6, C3, D5, D7, D9, D12, E2, E3].

Appendix

№	Monomer ratios [wt %]			Initiator Irq784 [wt %]	ChG [wt %]	Description
11h	UDMA 80	IDA 10	PEA 10	4%	7.5 % As_2S_3	Used for optical transmission measurements, and holographic recording, 30 μm thick
14h	UDMA 70	AmAc 20	PEA 10		7.5 % As_2S_3	
20h	UDMA 70	AmAc 20	PEA 10		7.5 % $As_{20}Se_{80}$	
14m	UDMA 70	AmAc 20	PEA 10	4%	-	

Table A. *Parameters of the developed nanocomposites and pure polymer samples*

№	Sample	thickness	Description
S1	bulk Se with polished surface	2–3 mm	Used for temperature modelling and studying crystallization effects
S2	twenty-year-old bulk Se with smooth, unpolished surface	2–3 mm	
	$As_{20}Se_{80}$	2.3 or 2.6 μm	Thin films used for holographic relief creation and viscosity measurements. Obtained by TVE method
	As_2S_3	2.5 μm	Optical transmission measurements related to the polymer-chalcogenide experiments. Obtained by TVE method
	Se, As_1Se_{99}, As_3Se_{97}, As_6Se_{94}, $As_{20}Se_{80}$, $As_{40}Se_{60}$, As_2S_3,	1–6 μm	Thin films used for relief creation and optical transmission measurements. Obtained by TVE method
	Se- smooth surface, As_6Se_{94}, $As_{30}Ge_{20}S_{50}$, As_2S_3– thick plates	1–3 mm	Bulk glass used for high energy ion irradiation
	Se, As_6Se_{94} (on silica or ITO substrate)	25–35 μm	Chalcogenide layers used for high energy ion irradiation. Obtained by TVE method

Table B. *Main parameters of the chalcogenide samples.*

Acknowledgments

I am thankful for the help and guidance of my supervisor, Dr. Sándor Kökényesi, during my doctoral studies.

I must thank Dr. Roland Bogdán for the experience I gained, while working on joint projects.

Thanks to Dr. Viktor Takáts for the help with temperature related measurements and to Dr. Attila Csík for SEM/EDX measurements.

Last but not least, I am thankful for the continuous support of my wife, and of my late parents, who supported and encouraged all my studies.

The work is supported by the GINOP-2.3.2-15-2016-00041 project. The project is co-financed by the European Union and the European Regional Development Fund.

Publications

Publications serving as the basis of the thesis/A PhD értekezés alapjául szolgáló közlemények:

[A1.] R. Bohdan, **S. Molnar**, I. Csarnovics, M. Veres, A. Csik, S. Kokenyesi, *Optical recording of surface relief on amorphous selenium*, J. Non. Cryst. Solids **408**, 57–61 (2015). **IF: 1.825**

[A2.] **S. Molnar**, R. Bohdan, V. Takats, Y. Kaganovskii, S. Kokenyesi, *Viscosity of As20Se80 amorphous chalcogenide films*, Mater. Lett. **228**, 384–386 (2018). **IF: 3.019**

[A3.] **S. Molnar**, R. Bohdan, V. Takats, Y. Kaganovskii, S. Kokenyesi, *Stimulated Surface Relief Erasing in Amorphous As-Se Layers: Thermal- and Light Induced Effects*, Phys. Status Solidi Appl. Mater. Sci. **215**, 24, 1–7 (2018). **IF: 1.606**

[A4.] R. Bohdan, **S. Molnar**, S. Kokenyesi, *Methods comparing peculiarities of surface-relief recording in amorphous chalcogenides*, Phys. status solidi **212**, 10, 2186–2190 (2015). **IF: 1.648**

[A5.] **S. Molnar**, R. Bohdan, G. Nagy, I. Rajta, L. Illes, A. Csik, S. Kokenyesi, *Direct surface patterning of amorphous chalcogenide layers with high- energy H+ and He+ ion beams*, J. Mater. Sci. Mater. Electron. **30**, 16, 15331–15338 (2019). **IF: 2.195**

[A6.] J. Burunkova, **S. Molnar**, V. Sitnikova, D. Shaimadiyeva, G. Alkhalil, R. Bohdan, J. Bako, F. Kolotaev, A. Bonyar, S. Kokenyesi, *Polymer–chalcogenide glass nanocomposites for amplitude–phase modulated optical relief recording*, J. Mater. Sci. Mater. Electron. **30**, 10, 9742–9750 (2019). **IF: 2.195**

Further publications/ További közlemények

[B1.] J. Burunkova, D. Zhuk, V. Kaliabin, **S. Molnar,** S. Kokenyesi, *Peculiarities of holographic microfabrication of photonic structures in functional polymer nanocomposites*, Optical Materials **88**, 516-521 (2019). **IF: 2.687**

[B2.] **S. Molnar**, R. Bohdan, V. Takats, Yu. Kaganovskii, K. Vad, S. Kokenyesi, *Kinetics of photo-darkening and -bleaching in amorphous As20Se80 layers: temperature dependence*, J. Optoelectron. Adv. Mater. **20**, 11/12, 646-650 (2018). **IF:0.588**

[B3.] I. Csarnovics, M. Veres, P. Nemec, MR. Latif, P. Hawlova, **S. Molnar**, S. Kokenyesi, *Surface patterning in GeSe amorphous layers*, J. Non. Cryst. Solids **459**, 51-56 (2017). **IF: 2.488**

[B4.] **S. Molnar**, R. Bohdan, S. Kokenyesi, *Crystallization at optical recording in amorphous selenium*, Acta Physica Debrecina **XLVIII**, 100 (2014). **IF: 0.00.**

[B5.] I. Csarnovics, M. Veres, P. Nemec, **S. Molnár**, S. Kökényesi, *Surface plasmon enhanced light-induced changes in Ge-Se amorphous chalcogenide – Gold nanostructures*, J. Non-Crystalline Solids X 6, 100045 (2020). **IF: 0.00**

Conference proceedings/ Konferencia közlemények

[C1.] **S. Molnar**, R. Bohdan, I. Csarnovics, I. Burunkova, S. Kokenyesi, *Amorphous chalcogenide layers and nanocomposites for direct surface patterning*, Proceedings of SPIE - The International Society for Optical Engineering **9359**, 935908-935908-10 (2015).

[C2.] I. Csarnovics, **S. Molnar**, J. Burunkova, D. Zhuk, I. Denisyuk, A. Bonyár, C. Cserhati, S. Kökenyesi, *Patterning photosensitive layers for optoelectronic applications*, 38th International Spring Seminar on Electronics Technology (ISSE), 57-60 (2015).

[C3.] **S. Molnar**, J. Burunkova, R. Bohdan, J. Bako, L. Daroczi, S. Kokenyesi, *Development of functional polymer nanocomposites for direct optical relief recording*, Clusters and Nanostructured materials: Abstract book, 32, 2018.

[C4.] **S. Molnar**, R. Bohdan, V. Takats, A. Reznik, S. Kokenyesi, *Influence of As-Se Based Chalcogenide Glasses' Electrical Conductivity on The Direction of Photo-Induced Mass Transport*, Conference proceedings, International Conference on Applied Physics and Mathematics, 1, 2019.

Posters/ Poszterek

[D1.] R. Bohdan, **S. Molnar**, I. Csarnovics, A. Csik, S. Kokenyesi, *Thermal Effects in Surface Relief Recording on Chalcogenide Glasses*, 15th Joint Vacuum Conference, Vienna, Austria, June 15-20, 2014.

[D2.] **S. Molnar**, Gy. Nagy, P. Hajdu, T. Nichol, M. Mitkova, R. Bohdan, I. Rajta, S. Kokenyesi, *Comparison of light- and ion beam surface patterning of amorphous chalcogenide layers*, 7th International Conference Amorphous and Nanostructured Chalcogenides, Cluj-Napoca, Romania, July 5-10, 2015.

[D3.] **S. Molnar**, V. Takats, R. Bohdan, S. Misak, I. Csarnovics, Yu. Kaganovsky, S. Kokenyesi, *Investigations of phase-modulated optical recording in amorphous chalcogenide layers from As-Se-Te system*, 8th International Conference Amorphous and Nanostructured Chalcogenides, Sinaia, Romania, July 2-5, 2017.

[D4.] **S. Molnar**, R. Bohdan, V. Takats, I. Csarnovics, Yu. Kaganovskii, S. Kokenyesi, *Temperature an illumination dependent mass transport during surface relief formation in As-S(Se) amprhous chalcogenides*, 15th International Conference on the Physics of Non-Crystalline Solids and 14th European Society of Glass Conference, St. Malo, France, 9-13, July 2018.

[D5.] J. Burunkova , N. Zulina, M. Baranova, D. Kussainova, A. Churbanova, **S. Molnar**, S. Kokenyesi, *Polymer-Chalcogenide Glass Nanocomposites for Optical Relief Recording*, 13th International Conference on Solid State Chemistry, Pardubice, Czech Republic, September 16-21, 2018.

[D6.] **S. Molnar**, R. Bohdan, I.Rajta, Gy. Nagy, S. Kokenyesi, *Ion beam patterning in As-Se amorphous layers*, 13th Inthernational Conference on Solid State Chemistry, Pardubice, Czech Republic, September 16-21, 2018.

[D7.] J. Burunkova, **S. Molnar**, D. Kussainova, M. Uspenskaya, M. Baranov, R. Bohdan, T. Nosenko, S. Kokenyesi, *Acrylate polymer nanocomposites for direct optical relief recording*, The 9th International Conference on Materials Science and Condensed Matter Physics, Chisinau, Moldova, September 25-28, 2018.

[D8.] **S. Molnar**, R. Bohdan, V. Takacs, A. Reznik, S. Kokenyesi, *The influence of conduction type on photo-induced mass transport in semiconductor chalcogenide glasses*, Conference proceedings, VIII. Ukrainian Conference on Physics of Semiconductors, Uzhgorod, Ukraine, October 2-4, 2018.

[D9.] J. Burunkova**, S. Molnar**, G. Alkhalil, D. Shaymadieva, L.Daroczi, A.Bonyar, S. Kokenyesi, *Acrylate polymer-inorganic nanocomposites for photonic applications*, 8th International Conference on Nanotechnology & Materials Science, Amsterdam, The Netherlands, April 24-26, 2019.

[D10.] **S. Molnar**, R. Bohdan, Gy. Nagy, I. Rajta, I. Makauz, M. Shipljak, V. Pinzenik, S. Kokenyesi, *Surface Patterning of Amorphous Chalcogenide Layers by Light and Ion-Beams*, XVII International Freik Conference On Physics And Technology of Thin Films and Nanosystems, Ivano-Frankivsk, Ukraine, May 20-25, 2019.

[D11.] G. Alkhalil, J. Burunkova, **S. Molnar**,F. Kolotaev, M. Veres, S. Kokenyesi, *Optical Properties of As2S3 in Thin Layers and Solid Matrices*, XI. International Conference "Basic Problems of Optics" BPO-2019, St. Petersburg, Russia, October 21-25, 2019.

[D12.] G. Alkhalil, **S. Molnar**, J. Burunkova, F. Kolotaev, V. Sitnikova, T. Nosenko, M. Veres, S. Kokenyesi, *Polymeric composites based on As2S3 nanoparticles for holographic recording of Bragg gratings*, 15th International Saint Petersburg Conference of Young Scientists, St. Petersburg, Russia, October 28-31, 2019.

Main talks/ Főbb előadások

[E1.] **S. Molnar**, R. Bohdan, P. Nemec, A. Bonyar, A. Reznik, S. Kokenyesi, *Composition- and electrical field-dependent surface relief recording in amorphous chalcogenide layers and structures*, 9th International Conference Amorphous and Nanostructured Chalcogenides, 30 June - 4 July 2019, Chisinau, Moldova.

[E2.] S. Kokenyesi, **S. Molnar**, J. Burunkova, G. Alkhalil, I. Csarnovics, Yu. Kaganovskii, *Surface relief recording-erasing in amorphous chalcogenide layers and nanocomposites*, 9th International Conference Amorphous and Nanostructured Chalcogenides, 30 June - 04 July 2019, Chisinau, Moldova

[E3.] **S. Molnár**, *Felületi struktúrák kialakítása amorf kalkogenid rétegekben és nanokompozitokban sugárzás- és hőstimulált anyagtranszport által*, Az MTA Felületkémiai és Nanoszerkezeti Munkabizottság, az ELFT Vákuumfizikai, -technológiai és Alkalmazásai Szakcsoport, a Magyar Vákuumtársaság és az MTA Elektronikus Eszközök és Technológiák Tudományos Bizottság közös szemináriuma, Budapest, 2019. október 29.

References

[1] A. V. Kolobov, *Photo-Induced Metastability in Amorphous Semiconductors*. Winheim: Whiley, 2008.

[2] B. J. Eggleton, B. Luther-Davies, K. Richardson, *Chalcogenide photonics*, Nat. Photonics **5**, 3, 141–148 (2011). doi: 10.1038/nphoton.2011.309.

[3] F. Smektala, C. Quemard, L. Leneindre, J. Lucas, A. Barthélémy, C. De Angelis, *Chalcogenide glasses with large non-linear refractive indices*, J. Alloys Compd. **239**, 1, 139–142 (1996).

[4] S. Kugler, K. Shimakawa, *Amorphous semiconductors*. Cambridge: Cambridge University Press, 2015.

[5] A. Viswanathan, S. Thomas, *Tunable linear and non linear optical properties of GeSeSb chalcogenide glass with solute concentration and with silver doping*, J. Alloys Compd. **798**, 424–430 (2019). doi: 10.1016/J.JALLCOM.2019.05.261.

[6] L. Calvez, *Chalcogenide glasses and glass-ceramics: Transparent materials in the infrared for dual applications*, Comptes Rendus Phys. **18**, 5–6, 314–322 (2017). doi: 10.1016/J.CRHY.2017.05.003.

[7] J. Horvat, *Handbook of Advanced Electronic and Photonic Materials and Devices*. San Diego: Academic Press, 2001.

[8] A. Stronski, M. Vlček, A. Sklenar, P. Shepeljavi, S. Kostyukevich, T. Wagner, *Application of As40S60−xSex layers for high-efficiency grating production*, J. Non. Cryst. Solids **266**–**269**, 973–978 (2000). doi: 10.1016/S0022-3093(00)00032-6.

[9] S. Kokenyesi, I. Iván, V. Takáts, J. Pálinkás, S. Biri, I. A. Szabo, *Formation of surface structures on amorphous chalcogenide films*, J. Non. Cryst. Solids **353**, 13–15, 1470–1473 (2007). doi: 10.1016/j.jnoncrysol.2006.09.064.

[10] Y. Handa, T. Suhara, H. Nishihara, J. Koyama, *Scanning-electron-microscope-written gratings in chalcogenide films for optical integrated circuits*, Appl. Opt. **18**, 2, 248 (1979). doi: 10.1364/ao.18.000248.

[11] V. I. Mikla, J. M. Turovci, V. V. Mikla, N. Mehta, *Molecular structure of Se-rich amorphous films*, Prog. Solid State Chem. **49**, 1–15 (2018). doi: 10.1016/j.progsolidstchem.2017.10.001.

[12] R. Zallen, *The Physics of Amorphous Solids*. Wiley, 2007.

[13] P. Chen, P. Boolchand, D. G. Georgiev, *Long term aging of selenide glasses: Evidence of sub-Tg endotherms and pre-Tg exotherms*, J. Phys. Condens. Matter **22**, 6, 065105 (2010). doi: 10.1088/0953-8984/22/6/065104.

[14] Z. U. Borisova, *Glassy Semiconductors*. New York: Plenum, 1981.

[15] M. A. Popescu, *Non-Crystalline Chalcogenides*. Bucharest: Kluwer Academic Publishers, 2000.

[16] R. S. Williams, T. Egami, *Effects of deformation and annealing on magnetic amorphous alloys*, IEEE Trans. Magn. **12**, 6, 927–929 (1976). doi: 10.1109/TMAG.1976.1059247.

[17] H. S. Chen, E. Coleman, *Structure relaxation spectrum of metallic glasses*, Appl. Phys. Lett. **28**, 5, 245–247 (1976). doi: 10.1063/1.88725.

[18] T. Egami, K. Maeda, V. Vitek, *Structural defects in amorphous solids A computer simulation study*, Philos. Mag. A Phys. Condens. Matter, Struct. Defects Mech. Prop. **41**, 6, 883–901 (1980). doi: 10.1080/01418618008243894.

[19] E. Mytilineou, *Chalcogenide amorphous semiconductors: chemical modification or doping?*, J. Optoelectron. Adv. Mater. **4**, 705 (2002).

[20] V. A. Twaddell, W. C. Lacourse, J. D. Mackenzie, *Impurity effects on the structure and electrical properties of non-crystalline selenium*, J. Non. Cryst. Solids **8**–**10**, C, 831–836 (1972). doi: 10.1016/0022-3093(72)90234-7.

[21] M. H. Cohen, H. Fritzsche, S. R. Ovshinsky, *Simple Band Model for Amorphous Semiconducting Alloys*, Phys. Rev. Lett. **22**, 20, 1065–1068 (1969). doi: 10.1103/PhysRevLett.22.1065.

[22] E. A. Davis, N. F. Mott, *Conduction in non-crystalline systems V. Conductivity, optical absorption and photoconductivity in amorphous semiconductors*, Philos. Mag. **22**, 179, 903–922 (1970). doi: 10.1080/14786437008221061.

[23] P. W. Anderson, *Model for the Electronic Structure of Amorphous Semiconductors*, Phys. Rev. Lett. **34**, 15, 953–955 (1975). doi: 10.1103/PhysRevLett.34.953.

[24] H. Fritzsche, *The Nature of Localized States and the Effect of Doping in Amorphous Semiconductors*, Chinese J. Phys. **15**, 2, 73–91 (1977).

[25] N. F. Mott, E. A. Davis, R. A. Street, *States in the gap and recombination*

in amorphous semiconductors, Philos. Mag. **32**, 5, 961–996 (1975). doi: 10.1080/14786437508221667.

[26] M. Kastner, H. Fritzsche, *Defect chemistry of lone-pair semiconductors*, Philos. Mag. B Phys. Condens. Matter; Stat. Mech. Electron. Opt. Magn. Prop. **37**, 2, 199–215 (1978). doi: 10.1080/01418637808226653.

[27] M. Kastner, D. Adler, H. Fritzsche, *Valence-Alternation Model for Localized Gap States in Lone-Pair Semiconductors*, Phys. Rev. Lett. **37**, 22, 1504–1507 (1976). doi: 10.1103/PhysRevLett.37.1504.

[28] Y. Kuzukawa, A. Ganjoo, K. Shimakawa, *Photoinduced structural changes in obliquely deposited As- and Ge-based amorphous chalcogenides: Correlation between changes in thickness and band gap*, J. Non. Cryst. Solids **227**–**230**, 2, 715–718 (1998). doi: 10.1016/S0022-3093(98)00192-6.

[29] S. Rajagopalan, K. S. Harshavardhan, L. K. Malhotra, K. L. Chopra, *Photo-optical changes in Ge-chalcogenide films*, J. Non. Cryst. Solids **50**, 1, 29–38 (1982). doi: 10.1016/0022-3093(82)90197-1.

[30] K. Starbova, J. Dikova, N. Starbov, *Structure related properties of obliquely deposited amorphous a-As2S3 thin films*, J. Non. Cryst. Solids (1997). doi: 10.1016/S0022-3093(96)00582-0.

[31] P. Boolchand, *Insulating and Semiconducting Glasses*, **17**,. World Scientific, 2000.

[32] M. Vlček, M. Frumar, A. Vidourek, *Photoinduced effects in Ge-Sb-S glasses and amorphous layers*, J. Non. Cryst. Solids **90**, 1–3, 513–516 (1987). doi: 10.1016/S0022-3093(87)80475-1.

[33] Y. Kuzukawa, A. Ganjoo, K. Shimakawa, Y. Ikeda, *Photo-induced structural changes in obliquely deposited arsenic-based amorphous chalcogenides: A model for photostructural changes*, Philos. Mag. B Phys. Condens. Matter; Stat. Mech. Electron. Opt. Magn. Prop. **79**, 2, 249–256 (1999). doi: 10.1080/13642819908206796.

[34] M. Frumar, Z. Polák, Z. Černošek, *Raman spectra and photostructural changes in the short-range order of amorphous As–S chalcogenides*, J. Non. Cryst. Solids **256**–**257**, 105–110 (1999). doi: 10.1016/S0022-3093(99)00454-8.

[35] M. Frumar, Z. Polák, J. Jedelský, Z. Černošek, B. Frumarová, *Structure and Optically Induced Changes of Reactivity and Optical Properties of Amorphous Chalcogenides*, Prop. Appl. Amorph. Mater. 321–328 (2001).

doi: 10.1007/978-94-010-0914-0_19.

[36] M. Frumar, Z. Polák, Z. Černošek, B. Frumarová, T. Wágner, *Photoinduced effects in amorphous chalcogenides*, *Chemical Papers*, **51**, 6,. 310–327, (1997), doi: 10.1007/978-94-011-5496-3_9.

[37] H. Hisakuni, K. Tanaka, *Giant photoexpansion in As2S3 glass*, Appl. Phys. Lett. **65**, 23, 2925–2927 (1994). doi: 10.1063/1.112533.

[38] H. Hamanaka, K. Tanaka, S. Iizima, *Reversible photostructural change in melt-quenched GeS2 glass*, Solid State Commun. **33**, 3, 355–357 (1980). doi: 10.1016/0038-1098(80)91169-2.

[39] V. V. Poborchii, A. V. Kolobov, K. Tanaka, *Photomelting of selenium at low temperature*, Appl. Phys. Lett. **74**, 2, 215–217 (1999). doi: 10.1063/1.123297.

[40] H. Hisakuni, K. Tanaka, *Optical microfabrication of chalcogenide glasses*, Science (80-.). **270**, 5238, 974–975 (1995). doi: 10.1126/science.270.5238.974.

[41] S. H. Wemple, M. DiDomenico, *Behavior of the electronic dielectric constant in covalent and ionic materials*, Phys. Rev. B **3**, 4, 1338–1351 (1971). doi: 10.1103/PhysRevB.3.1338.

[42] S. H. Wemple, *Optical oscillator strengths and excitation energies in solids, liquids, and molecules*, J. Chem. Phys. **67**, 5, 2151–2168 (1977). doi: 10.1063/1.435102.

[43] M. Vlček, M. Frumar, M. Kubový, V. Nevšímalová, *The influence of the composition of the layers and of the inorganic solvents on photoinduced dissolution of As-S amorphous thin films*, J. Non. Cryst. Solids **137**–**138**, PART 2, 1035–1038 (1991). doi: 10.1016/S0022-3093(05)80298-4.

[44] M. Vlćek, J. Prokop, M. Frumar, *Positive and negative etching of As-S thin layers*, Int. J. Electron. **77**, 6, 969–973 (1994). doi: 10.1080/00207219408926118.

[45] S. R. Elliott, A. V. Kolobov, *Athermal light-induced vitrification of As50Se50 films*, *Journal of Non-Crystalline Solids*, **128**, 2,. 216–220, (1991), doi: 10.1016/0022-3093(91)90516-9.

[46] V. Balitska, O. Shpotyuk, *Radiation-induced structural transformations in vitreous chalcogenide semiconductors*, J. Non. Cryst. Solids **227**–**230**, 723–727 (1998). doi: 10.1016/S0022-3093(98)00154-9.

[47] B. Ushkov, R. Fairman, *Semiconducting Chalcogenide Glass I: Glass*

Formation, Structure, and Stimulated Transformations in Chalcogenide Glasses. 2004.

[48] H. Nishihara, Y. Handa, T. Suhara, J. Koyama, *Direct writing of optical gratings using a scanning electron microscope*, Appl. Opt. **17**, 15, 2342 (1978). doi: 10.1364/ao.17.002342.

[49] O. Nordman, N. Nordman, N. Peyghambarian, *Electron beam induced changes in the refractive index and film thickness of amorphous AsxS100-xand AsxSe100-xfilms*, J. Appl. Phys. **84**, 11, 6055–6058 (1998). doi: 10.1063/1.368915.

[50] K. Tanaka, *Electron beam induced reliefs in chalcogenide glasses*, Appl. Phys. Lett. **70**, 2, 261–263 (1997). doi: 10.1063/1.118356.

[51] P. Dwivedi, S. Tripathi, A. Pradhan, V. Kulkarni, S. Agarwal, *Raman study of ion irradiated GeSe films*, J. Non. Cryst. Solids **266**–**269**, 924–928 (2000). doi: 10.1016/S0022-3093(99)00867-4.

[52] M. S. Kamboj, G. Kaur, R. Thangaraj, D. K. Avasthi, *Effect of heavy ion irradiation on the electrical and optical properties of amorphous chalcogenide thin films*, J. Phys. D. Appl. Phys. **35**, 5, 477–479 (2002). doi: 10.1088/0022-3727/35/5/310.

[53] T. Tsvetkova, S. Balabanov, B. Amov, A. Djakov, I. H. Wilson, *Surface morphology changes in ion implanted chalcogenide films after annealing*, Nucl. Inst. Methods Phys. Res. B **80**–**81**, PART 2, 1264–1267 (1993). doi: 10.1016/0168-583X(93)90780-A.

[54] I. István, *Foto - és ionindukált változások kalkogenid rétegekben*, Debreceni Egyetem, 2009.

[55] M. Shiplyak, S. Kikineshi, D. Beke, K. S. Sangunni, *Amorphous Chalcogenide Nanomultilayers for Photonics*, Phys. Chem. Solid State **9**, 8, (2008).

[56] K. L. Chopra, K. S. Harshavardhan, S. Rajagopalan, L. K. Malhotra, *Ion-induced physical and optical densification in obliquely deposited Se0.75Ge0.25 films*, Appl. Phys. Lett. **40**, 5, 428–430 (1982). doi: 10.1063/1.93127.

[57] M. Chomát, D. Ležal, I. Gregora, I. Srb, *Relief holograms in thin films of amorphous As2Se3 under high laser exposures*, J. Non. Cryst. Solids **20**, 3, 427–437 (1976). doi: 10.1016/0022-3093(76)90123-X.

[58] P. Rochon, E. Batalla, A. Natansohn, *Optically induced surface gratings on azoaromatic polymer films*, Appl. Phys. Lett. **66**, 2, 136–138 (1995).

doi: 10.1063/1.113541.

[59] V. M. Kryshenik, Y. M. Azhniuk, V. S. Kovtunenko, *All-optical patterning in azobenzene polymers and amorphous chalcogenides*, *Journal of Non-Crystalline Solids*, **512**,. 112–131, (2019), doi: 10.1016/j.jnoncrysol.2019.02.019.

[60] J. Teteris, M. Reinfelde, J. Aleksejeva, U. Gertners, *Optical field-induced mass transport in soft materials*, in *Physics Procedia*, 2013, **44**, 151–158, doi: 10.1016/j.phpro.2013.04.019.

[61] M. Reinfelde, L. Loghina, Z. G. Ivanova, J. Teteris, U. Gertners, S. Slang, M. Vlcek, *Photoinduced surface relief grating formation in amorphous As40S60-xSex thin films*, J. Optoelectron. Adv. Mater. **18**, 1–2, 1–4 (2016).

[62] M. L. Trunov, V. S. Bilanich, S. N. Dub, R. S. Shmegera, *Giant photoplastic effect in vitreous semiconductors near the rigidity percolation transition*, JETP Lett. **82**, 8, 504–508 (2005). doi: 10.1134/1.2150870.

[63] A. Saliminia, T. V Galstian, A. Villeneuve, *Optical field-induced mass transport in As2S3 chalcogenide glasses*, Phys. Rev. Lett. **85**, 19, 41112 (2000). doi: 10.1103/PhysRevLett.85.4112.

[64] M. L. Trunov, P. M. Lytvyn, P. M. Nagy, O. M. Dyachyns'Ka, *Real-time atomic force microscopy imaging of photoinduced surface deformation in Asx Se100-x chalcogenide films*, Appl. Phys. Lett. **96**, 11, (2010). doi: 10.1063/1.3360229.

[65] M. L. Trunov, P. M. Lytvyn, S. N. Yannopoulos, I. A. Szabo, S. Kökényesi, *Photoinduced mass-transport based holographic recording of surface relief gratings in amorphous selenium films*, Appl. Phys. Lett. **99**, 5, 051906 (2011). doi: 10.1063/1.3614432.

[66] V. Takáts, M. L. Trunov, K. Vad, J. Hakl, D. L. Beke, Y. Kaganovskii, S. Kökényesi, *Low-temperature photo-induced mass transfer in thin As20Se80 amorphous films*, Mater. Lett. **160**, 558–561 (2015). doi: 10.1016/j.matlet.2015.08.040.

[67] M. L. Trunov, P. M. Lytvyn, *Selective light-induced mass transport in amorphous AsxSe100−x films driven by the composition tuning: Effect of temperature on maximum acceleration*, J. Non. Cryst. Solids **493**, 86–93 (2018). doi: 10.1016/j.jnoncrysol.2018.04.038.

[68] Y. Kaganovskii, M. L. Trunov, D. L. Beke, S. Kökényesi, *Mechanism of photo induced mass transfer in amorphous chalcogenide films*, Mater. Lett. **66**, 1, 159–161 (2012). doi: 10.1016/j.matlet.2011.08.045.

[69] Y. Kaganovskii, D. L. Beke, S. Kökńyesi, *Kinetics of photoinduced surface patterning in chalcogenide thin films*, Appl. Phys. Lett. **97**, 6, 061906 (2010). doi: 10.1063/1.3477957.

[70] J. Burunkova, S. Molnar, V. Sitnikova, D. Shaimadiyeva, G. Alkhalil, R. Bohdan, J. Bako, F. Kolotaev, A. Bonyar, S. Kokenyesi, *Polymer–chalcogenide glass nanocomposites for amplitude–phase modulated optical relief recording*, J. Mater. Sci. Mater. Electron. **30**, 10, 9742–9750 (2019). doi: 10.1007/s10854-019-01309-w.

[71] I. Csarnovics, M. Veres, P. Nemec, M. R. Latif, P. Hawlova, S. Molnar, S. Kokenyesi, *Surface patterning in Ge[sbnd]Se amorphous layers*, J. Non. Cryst. Solids **459**, 51–56 (2017). doi: 10.1016/j.jnoncrysol.2016.12.035.

[72] R. Bohdan, S. Molnar, S. Kokenyesi, *Methods comparing peculiarities of surface-relief recording in amorphous chalcogenides*, Phys. status solidi **212**, 10, 2186–2190 (2015). doi: 10.1002/pssa.201532288.

[73] S. Molnar, R. Bohdan, V. Takats, Y. Kaganovskii, S. Kokenyesi, *Stimulated Surface Relief Erasing in Amorphous As-Se Layers: Thermal- and Light Induced Effects*, Phys. Status Solidi Appl. Mater. Sci. **215**, 24, 1–7 (2018). doi: 10.1002/pssa.201800589.

[74] R. Swanepoel, *Determination of the thickness and optical constants of amorphous silicon*, J. Phys. E. **16**, 12, 1214–1222 (1983). doi: 10.1088/0022-3735/16/12/023.

[75] N. F. Mott, E. A. Davis, *Electronic Processes in Non-Crystalline Materials*, 2nd ed.,. Oxford: Clarendon Press, 1979.

[76] S. Molnar, R. Bohdan, I. Csarnovics, I. Burunkova, S. Kokenyesi, *Amorphous chalcogenide layers and nanocomposites for direct surface patterning*, in *Proceedings of SPIE - The International Society for Optical Engineering*, 2015, **9359**, doi: 10.1117/12.2076470.

[77] M. L. Trunov, C. Cserháti, P. M. Lytvyn, Y. Kaganovskii, S. Kökényesi, *Electron beam-induced mass transport in As-Se thin films: Compositional dependence and glass network topological effects*, J. Phys. D. Appl. Phys. **46**, 24, (2013). doi: 10.1088/0022-3727/46/24/245303.

[78] I. Csarnovics, C. Cserhati, S. Kokenyesi, M. R. Latif, M. Mitkova, P. Nemec, P. Hawlova, T. Nichol, M. Veres, *Light and electron beam induced surface patterning in Ge-Se system*, J. Optoelectron. Adv. Mater. **18**, 9–10, 793–797 (2016).

[79] J. F. Ziegler, M. D. Ziegler, J. P. Biersack, *SRIM - The stopping and range*

of ions in matter (2010), Nucl. Instruments Methods Phys. Res. Sect. B Beam Interact. with Mater. Atoms **268**, 11–12, 1818–1823 (2010). doi: 10.1016/j.nimb.2010.02.091.

[80] S. Molnar, R. Bohdan, G. Nagy, I. Rajta, L. Illes, A. Csik, S. Kokenyesi, *Direct surface patterning of amorphous chalcogenide layers with high-energy H+ and He+ ion beams*, J. Mater. Sci. Mater. Electron. **30**, 16, 15331–15338 (2019). doi: 10.1007/s10854-019-01906-9.

[81] A. Feltz, *Amorphous inorganic materials and glasses*. New York: Wiley, 1993.

[82] R. Bohdan, S. Molnar, I. Csarnovics, M. Veres, A. Csik, S. Kokenyesi, *Optical recording of surface relief on amorphous selenium*, J. Non. Cryst. Solids **408**, 57–61 (2015). doi: 10.1016/j.jnoncrysol.2014.10.016.

[83] M. Popescu, *Aide-Memoire: Chalcogenides and General Tables for Materials Scientist*. Bucharest: INOE, 2005.

[84] B. I. Boltaks, *Diffuziya i Tochechnye Defekty v Poluprovodnikakh (Diffusion and Point Defects in Semiconductors)*. St. Petersburg: Nauka, 1972.

[85] C. Rüssel, *Electrochemical study on the redox behavior of selenium-containing soda-lime-silica melts*, Glas. Sci. Technol. Glas. Berichte **74**, 1, 1–5 (2001).

[86] A. A. Joraid, A. A. Abu-Sehly, S. N. Alamri, *Isoconversional kinetic analysis of the crystallization phases of amorphous selenium thin films*, Thin Solid Films **517**, 21, 6137–6141 (2009). doi: 10.1016/j.tsf.2009.05.034.

[87] C. Górecki, T. Górecki, *Structural transformations in amorphous selenium as studied by the differential thermal analysis and exoelectron emission technique*, in *Journal of Physics: Conference Series*, 2007, **79**, 1, doi: 10.1088/1742-6596/79/1/012039.

[88] S. Wacke, T. Górecki, K. Ksia˛zek, C. Górecki, *Effect of the milling conditions on the degree of crystallization of amorphous selenium by milling in a planetary ball mill*, Visn. Lviv Univ. Ser. Phys. **43**, 81 (2009).

[89] G. Lucovsky, R. M. Martin, *A molecular model for the vibrational modes in chalcogenide glasses*, J. Non. Cryst. Solids **8**–**10**, C, 185–190 (1972). doi: 10.1016/0022-3093(72)90134-2.

[90] J. Tauc, *Amorphous and Liquid Semiconductors*. New York: Plenum, 1974.

[91] G. B. Abdullaev, S. I. Mekhtieva, D. Sh. Abdinov, G. M. Aliev, S. G. Alieva, *Thermal Conductivity of Selenium*, Phys. status solidi **13**, 2, 315–323 (1966). doi: 10.1002/pssb.19660130203.

[92] A. H. Abou El Ela, H. H. A. Labib, K. A. H. Sharaf, *Thermal conductivity of liquid selenium and Se−Tl−S alloys*, Acta Phys. Acad. Sci. Hungaricae **47**, 4, 353–356 (1979). doi: 10.1007/BF03158234.

[93] M. L. Trunov, P. M. Lytvyn, S. N. Yannopoulos, I. A. Szabo, S. Kökényesi, *Photoinduced mass-transport based holographic recording of surface relief gratings in amorphous selenium films*, Appl. Phys. Lett. **99**, 5, (2011). doi: 10.1063/1.3614432.

[94] W. W. Mullins, *Flattening of a nearly plane solid surface due to capillarity*, J. Appl. Phys. **30**, 1, 77–83 (1959). doi: 10.1063/1.1734979.

[95] S. Molnar, R. Bohdan, V. Takats, Y. Kaganovskii, S. Kokenyesi, *Viscosity of As20Se80 amorphous chalcogenide films*, Mater. Lett. **228**, 384–386 (2018). doi: 10.1016/j.matlet.2018.06.065.

[96] B. P. Pal, *Guided Wave Optical Components and Devices*. Cambridge: Academic Press, 2006.

[97] T. D. Mel'Nichenko, V. I. Fedelesh, T. N. Mel'Nichenko, D. S. Sanditov, S. S. Badmaev, D. G. Damdinov, *On the approximate estimation of the surface tension of chalcogenide glass melts*, Glas. Phys. Chem. **35**, 1, 32–42 (2009). doi: 10.1134/S1087659609010052.

[98] S. Nemilov, *The Relation between the Free Energy of Activation for Viscous Flow and the Energy of the Chemical Bonds in Glasses*, Sov. Phys. Solid State **6**, 5, 1075–1078 (1964).

[99] S. Suzuki, T. Kobayashi, H. Ohno, S. Kamiya, *Viscosity of Glasses in the System As-Se and As-Se-X (X=I, S) in the Transition Region*, J. Soc. Mater. Sci. Japan **22**, 233, 134–139 (1973). doi: 10.2472/jsms.22.134.

[100] K. M. Bernatz, I. Echeverría, S. L. Simon, D. J. Plazek, *Characterization of the molecular structure of amorphous selenium using recoverable creep compliance measurements*, J. Non. Cryst. Solids **307**–**310**, 790–801 (2002). doi: 10.1016/S0022-3093(02)01522-3.

[101] J. D. Musgraves, P. Wachtel, S. Novak, J. Wilkinson, K. Richardson, *Composition dependence of the viscosity and other physical properties in the arsenic selenide glass system*, J. Appl. Phys. **110**, 6, (2011). doi: 10.1063/1.3638122.

[102] M. Trunov, P. Lytvyn, V. Takats, I. Charnovich, S. Kokenyesi, *Direct*

surface relief formation in As0.2Se0.8 layers, J. Optoelectron. Adv. Mater. **11**, 12, 1959–1962 (2009).

[103] J. Dresner, *The photo-hall effect in vitreous selenium**, J. Phys. Chem. Solids **25**, 5, 505–511 (1964). doi: 10.1016/0022-3697(64)90123-4.

[104] T. C. Sum, A. A. Bettiol, H. L. Seng, I. Rajta, J. A. van Kan, F. Watt, *Proton beam writing of passive waveguides in PMMA*, Nucl. Instruments Methods Phys. Res. Sect. B Beam Interact. with Mater. Atoms **210**, 266–271 (2003). doi: 10.1016/S0168-583X(03)01028-0.

[105] M. B. H. Breese, D. N. Jamieson, P. J. C. King, *Materials analysis using a nuclear microprobe*. Hoboken: Wiley, 1996.

[106] J.-L. Adam, X. Zhang, *Chalcogenide Glasses, Preparation, Properties and Applications*, Chalcogenide Glas. Prep. Prop. Appl. (2014).

[107] C. Cserhati, S. Charnovych, P. M. Lytvyn, M. L. Trunov, D. L. Beke, Y. Kaganovskii, S. Kökényesi, *E-beam induced mass transport in amorphous As 20Se 80 films*, Mater. Lett. **85**, 113–116 (2012). doi: 10.1016/j.matlet.2012.06.095.

[108] V. Bilanych, V. Komanicky, M. Kozejova, A. Feher, A. Kovalcikova, F. Lofaj, V. Kuzma, V. Rizak, *Surface pattering of Ge–As–Se thin films by electric charge accumulation*, Thin Solid Films **616**, 86–94 (2016). doi: 10.1016/j.tsf.2016.07.073.

[109] L. Tichý, H. Tichá, *Covalent bond approach to the glass-transition temperature of chalcogenide glasses*, J. Non. Cryst. Solids **189**, 1–2, 141–146 (1995). doi: 10.1016/0022-3093(95)00202-2.

[110] A. S. Tverjanovich, *Temperature dependence of the viscosity of chalcogenide glass-forming melts*, *Glass Physics and Chemistry*, **29**, 6,. 532–536, (2003), doi: 10.1023/B:GPAC.0000007927.77309.ee.

[111] A. Kikineshi, *Layers of light-sensitive chalcogenide glass for optical recording*, Opt. Mem. Neural Networks **4**, 3, (1995).

[112] D. M. Bercha, A. A. Kikineshi, M. I. Marjan, *Anizotropnye jelementy struktury i inducirovannye deformacii v hal'kogenidnom stekle (in Russian)*, Ukr. Phys. J. **26**, 6, (1981).

[113] A. Reznik, S. D. Baranovskii, O. Rubel, K. Jandieri, S. O. Kasap, Y. Ohkawa, M. Kubota, K. Tanioka, J. A. Rowlands, *Avalanche multiplication in amorphous selenium and its utilization in imaging*, J. Non. Cryst. Solids **354**, 19–25, 2691–2696 (2008). doi: 10.1016/j.jnoncrysol.2007.09.058.

[114] O. Bubon, G. Decrescenzo, J. A. Rowlands, A. Reznik, *Amorphous selenium (a-Se) avalanche photosensor with metal electrodes*, J. Non. Cryst. Solids **358**, 17, 2431–2433 (2012). doi: 10.1016/j.jnoncrysol.2011.12.093.

[115] N. Toyosawa, K. Tanaka, *Photocurrent enhancement in light-soaked chalcogenide glasses*, Phys. Rev. B **56**, 12, 7416–7421 (1997). doi: 10.1103/PhysRevB.56.7416.

[116] C. Cserháti, I. Csarnovics, L. Harasztosi, M. L. Trunov, S. Kökényesi, *Direct surface relief formation by e-beam in amorphous chalcogenide layers*, J. Mater. Sci. Mater. Electron. **28**, 10, 7024–7028 (2017). doi: 10.1007/s10854-016-6076-y.

[117] I. Dekhant, R. Dants, V. Kimmer, R. Shmol'ke, *Infrakrasnaya Spektroskopiya Polimerov*. Moscow: Chemistry Publ., 1976.

[118] V. N. Vatulev, S. V Laptii, Y. Y. Kercha, *Infrakrasnye Spektry i Struktura Poliuretanov (Infrared Spectra and Structure of Polyurethanes)*. Kiev: Naukova Dumka, 1987.

[119] L. Bellami, *IR Spectra of Complex Molecules*, Infrakrasnye Spektry Slozhnykh Mol. (1963).

[120] B. N. Tarasevich, *IK spektry osnovnykh klassov organicheskikh soedinenii. Spravochnye materialy*. Moscow: Mosk. Gos. Univ., 2012.

[121] Y. Rabek, *Jeksperimenl'nye metody v himii polimerov*, **1**,. Moscow: Mir, 1983.

[122] K. Kaminski, R. Wrzalik, M. Paluch, J. Zioło, C. M. Roland, *Pressure-induced polymerization of phenoxyethyl acrylate*, J. Phys. Condens. Matter **20**, 24, (2008). doi: 10.1088/0953-8984/20/24/244121.

[123] K. Tanaka, K. Shimakawa, *Amorphous Chalcogenide Semiconductors and Related Materials*. New York, NY: Springer, 2011.

[124] A. Kikineshi, A., Mishak, *Photoinduced Effects in Chalcogenide Glasses and their Application for Optical Recording*, Photoinduced Eff. Chalcogenide Glas. their Appl. Opt. Rec. Phys. Appl. Non-Crystalline Semicond. Optoelectron. NATO ASI Ser. **3**, 249–257 (1997).

[125] J. C. Maxwell-Garnett, *Colours in metal glasses and in metallic films*, Philos. Trans. R. Soc. London **203**, 385–420 (1904).

[126] O. Wiener, *Lamellare doppelbrechung*, Phys. Z. **5**, 332–338 (1904).

[127] O. Wiener, *Die theorie des Mischkorpers für das Feld der statonären Stromüng i. die mittelwertsatze für kraft, polarisation und energie*, Der Abhandlungen der Math. Klasse der Königl. Sachs. Gesellschaft der Wissenschaften **32**, 6, 509–604 (1912).

[128] D. A. G. Bruggeman, *Berechnung verschiedener physikalischer Konstanten von heterogenen Substanzen. I. Dielektrizitätskonstanten und Leitfähigkeiten der Mischkörper aus isotropen Substanzen*, Ann. Phys. **416**, 7, 636–664 (1935). doi: 10.1002/andp.19354160705.

[129] K. Lichtenecker, *Die dielektrizitatskonstante naturlicher und kunstlicher mischkorper*, Phys. Z. **27**, 115–158 (1926).

[130] N. A. Carlie, *A Solution-Based Approach to the Fabrication of Novel Chalcogenide Glass Materials and Structures*, Clemson University, 2010.

[131] L. A. Golovan', V. Y. Timoshenko, P. K. Kashkarov, *Optical properties of porous-system based nanocomposites*, Usp. Fiz. Nauk **177**, 6, (2007).

[132] A. A. Al-Ghamdi, *Optical band gap and optical constants in amorphous Se96- xTe4Agx thin films*, Vacuum **80**, 5, 400–405 (2006). doi: 10.1016/j.vacuum.2005.07.003.

[133] H. Kogelnik, *Coupled Wave Theory for Thick Hologram Gratings*, Bell Syst. Tech. J. **48**, 9, 2909–2947 (1969). doi: 10.1002/j.1538-7305.1969.tb01198.x.

[134] D. I. Zhuk, J. A. Burunkova, I. Y. Denisyuk, G. P. Miroshnichenko, I. Csarnovics, D. Tóth, A. Bonyár, M. Veres, S. Kokenyesi, *Peculiarities of photonic crystal recording in functional polymer nanocomposites by multibeam interference holography*, Polymer (Guildf). **112**, 136–143 (2017). doi: 10.1016/j.polymer.2017.02.004.